High energy multi-cycle terahertz generation

Dissertation

zur Erlangung des akademischen Grades

Doctor rerum naturalium

(Doktor der Naturwissenschaften)

vorgelegt von

Frederike Beate Ahr

aus Wuppertal

an der

Universität Hamburg

Fakultät für Mathematik, Informatik und Naturwissenschaften,

Fachbereich Physik

Hamburg, 2017

Gutachter der Dissertation: Prof. Dr. Franz X. Kärtner
Dr. Andreas R. Maier

Zusammensetzung der Prüfungskommission: Prof. Dr. Franz X. Kärtner
Dr. Andreas R. Maier
Prof. Dr. Daniela Pfannkuche
Jun. Prof. Dr. Thorsten Uphues
Jun. Prof. Dr. Ulrike Frühling

Datum der Disputation: 30.8.2017

Vorsitzender der Prüfungskomission: Prof. Dr. Daniela Pfannkuche

Vorsitzender des Promotionsausschusses: Prof. Dr. Wolfgang Hansen

Dekan der Fakultät für Mathematik,
Informatik und Naturwissenschaften: Prof. Dr. Heinrich Graener

"Quidquid agis, prudenter agas et respice finem."

Gesta Romanorum, Cap. 103

Abstract

Development of compact electron accelerators and free-electron lasers requires novel acceleration schemes at shorter driving wavelengths. The AXSIS project seeks to develop terahertz based electron acceleration as well as the high energy terahertz sources required. This thesis explores the methods and optical material required for the generation of high-energy multi-cycle terahertz pulses. Two experimental concepts to generate high energy terahertz radiation are presented. In addition the theoretical background and the optical properties of pertinent optical materials in the terahertz range are discussed.

Investigations of the materials are performed with a terahertz time domain spectrometer and a Fourier transform infrared spectrometer. The nonlinear optical crystal lithium niobate as well as other crystals suitable for the terahertz generation and in addition polymers and other radiation attenuators are characterized in the range from 0.2 to 1 THz.

The theory describing the generation of narrowband terahertz radiation is evaluated. The experimental setups to generate terahertz radiation and to characterize its properties are described. The specific crystals – periodically poled lithium niobate (PPLN) – used in the experiments to generate the multi-cycle terahertz radiation are examined to determine e.g. the poling period.

The first experimental concept splits the ultra fast, broadband pump pulses into a pulse train in order to pump the PPLN at a higher fluence while increasing the damage limit. The measurements confirm that a pulse train of ultra short, broadband pump pulses increases not only the terahertz energy but also the energy conversion efficiency.

The second experimental concept utilizes chirped and delayed infrared laser pulses. This pulse format makes it possible to pump the crystal with high energy pulses resulting in high energy terahertz radiation. The concept is optimized to reach energies up to 127 µJ exceeding the existing results of narrowband terahertz sources by two orders of magnitude.

These results endorse the proposed methods of generating multi-cycle THz pulses at the mJ-level and show a pathway for further scaling to the multi-mJ-level required for the construction of the electron accelerator in the AXSIS project.

Zusammenfassung

Der Bau von Elektronen-Beschleunigern und Freien Elektronen Lasern erfordert neue Beschleunigungskonzepte, die auf kurzen Wellenlängen basieren. Das Axsis Projekt hat sich zum Ziel gesetzt, sowohl die auf Terahertzstrahlung basierende Elektronen-Beschleunigung als auch die erforderlichen hochenergetischen Terahertzquellen zu entwickeln.

Diese Arbeit untersucht die Methoden und die optischen Materialien, die zur Erzeugung hochenergetischer multi-cycle Terahertzspulse benötigt werden. Sie stellt zwei experimentelle Konzepte vor, mit denen hochenergetische Terahertzstrahlung erzeugt werden kann. Zusätzlich werden der theoretische Hintergrund sowie die optischen Eigenschaften der für den Terahertzbereich relevanten Materialien diskutiert.

An einem Terahertzspektrometer und einem Fourier-Transformations Infrarotspektrometer werden der nichtlineare optische Kristall Lithium Niobate sowie andere zur Terahertzerzeugung geeignete Kristalle im Terahertzband von 0.2 bis 1 THz untersucht. Auch Polymere und andere Strahlungsabschwächer werden charakterisiert.

Zunächst werden die theoretischen Grundlagen zusammengefasst, auf denen die Erzeugung der schmalbandigen Terahertzstrahlung basiert. Anschließend werden die Versuchsaufbauten zur Erzeugung der Terahertzstrahlung und zur Beschreibung ihrer Eigenschaften dargelegt. Die einzelnen Kristalle, die zur Erzeugung der multi-cycle Terahertzstrahlung eingesetzt werden, - periodisch gepolte Lithium Niobat (PPLN) Kristalle - werden eingehend beschrieben.

Im ersten experimentellen Konzept werden die ultrakurzen, breitbandigen Pumpimpulse in einen Impulszug aufgeteilt. Es ermöglicht, den periodisch gepolten Lithium Niobat Kristall mit einer höheren Fluenz zu pumpen und die Zerstörschwelle zu erhöhen. Die Messungen bestätigen, dass mit einem Impulszug von ultrakurzen, breitbandigen Pumpimpulsen nicht nur eine höhere Terahertzenergie sondern auch eine höhere Energiekonver-

sionseffizienz erreicht wird.

Das zweite experimentellen Konzept basiert auf gechirpten und zeitlich verschobenen infraroten Laserimpulsen, die es ermöglichen den Kristall mit hohen Energien nichtlinear anzuregen. Mit ihm gelingt es hochenergetische Terahertzstrahlung zu erzeugen. Dieses Konzept wird abschließend so verbessert, dass Energien bis zu 127 µJ erreicht werden, die die bisherigen Ergebnisse von schmalbandigen Terahertzquellen um zwei Größenordnungen übertreffen.

Diese Ergebnisse bestätigen die vorgeschlagenen Methoden zur Erzeugung von multicycle Terahertzpulsen mit Energien im mJ-Bereich und ebnen den Weg für eine weitere Erhöhung in den multi-mJ-Bereich, der für den Bau eines Elektronenbeschleuniger im AXSIS Projekt erforderlich ist.

Contents

1. Introduction

At the beginning of the 20th century the newly discovered X-ray radiation [Rön98] opened a new insight into materials and living organisms. The enthusiasm associated with the pictures diversified at that time quite substantial our understanding of nature and science. About one century of continuous improvements of X-ray instruments resulted in better resolution reaching today down to the molecular level. Large facility free-electron lasers (FEL) like LCLS at SLAC (USA), SACLA at RIKEN (Japan) or FLASH at DESY (Germany) supported by research funding already reach a few Angstrom resolution with femtosecond (femto = 10^{-15}) time resolution. Broad applications suffer from limited access and high cost at these research units. From science and industry there is an increasing demand for broader access achievable by "table-top" sources providing deeper understanding of structure and function at the atomic and molecular level. Even energy conversion processes at cellular levels may become traceable.

Therefore the project AXSIS – frontiers in Attosecond X-ray Science: Imaging and Spectroscopy – was initiated using the synergy of laser-, accelerator- and X-ray-scientists and spectroscopists as well as biochemists to build a "table top" FEL based on terahertz

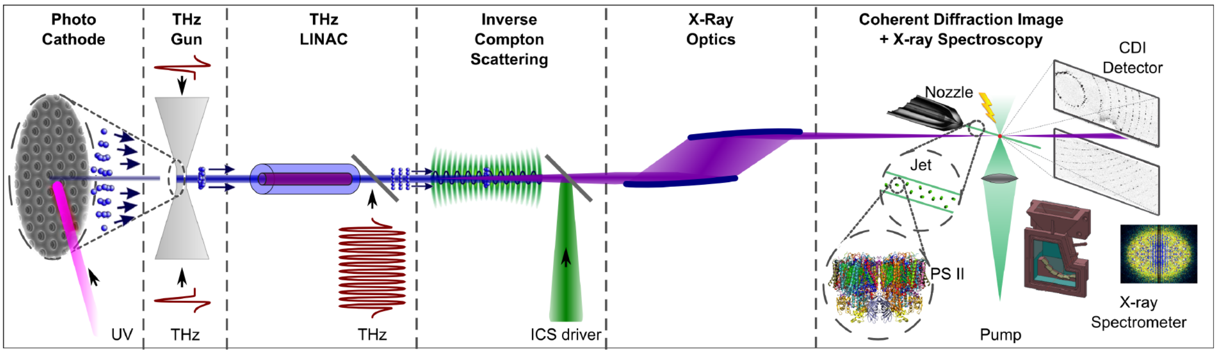

Figure 1.1.: The proposed AXSIS machine under development at DESY in Hamburg [Kär16].

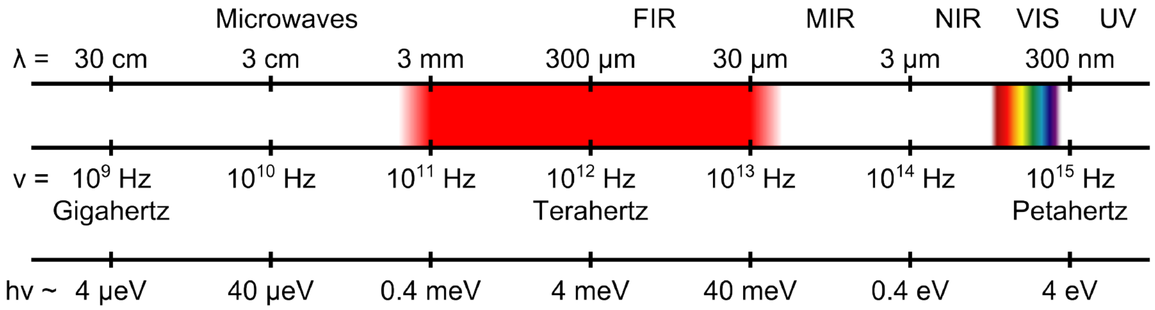

Figure 1.2.: The THz regime from 0.1 – 1 THz is marked in red in the electromagnetic spectrum. The corresponding wavelength range is 3 – 0.03 mm and the photon energy is 0.4 – 40 meV, respectivly.

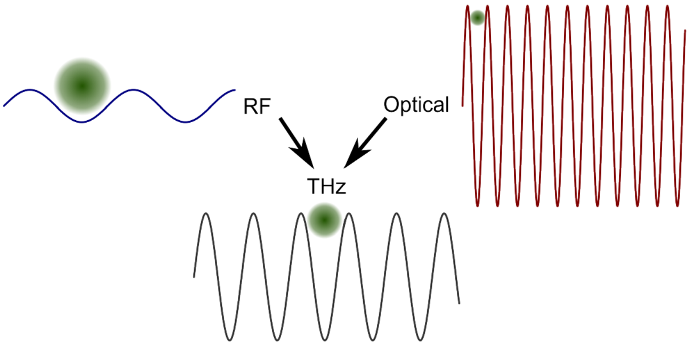

Figure 1.3.: Pictural representation of the benefits for THz accelerator.

radiation as accelerating field to measure dynamics of biological processes [Kär16]. AXSIS will generate keV X-rays with attosecond pulse durations enabling molecular movies before perturbing the sample [Kär16]. Figure 1.1 depicts the schematic layout of the AXSIS maschine. Within the AXSIS project the laser group focuses on the development of high energy THz pulses (1 THz = 10^{15} Hz) and their laser drivers. Within the electromagnetic spectrum the terahertz (THz) band is located at wavelength of 3 mm to 30 µm between the microwave band and the infrared band (figure 1.2, red).

The THz driven electron accelerator was anticipated to be a good compromise between high charge at conventional accelerators based on radio frequency technology and high acceleration gradient at pure laser-based accelerators. A THz based electron accelerator should accelerate enough electrons ($\sim$ 1 pC) reaching the requested acceleration fields ($\sim$ 1 GeV/m) (figure 1.3).

The linear or circular accelerator (LINAC) (figure 1.1 3rd block) requires mJ-level multi-cycle THz pulses in the low frequency range of $0.1 - 1\,\mathrm{THz}$ to accelerate electrons to an energy up to $10-20\,\mathrm{MeV}$ [Won13]. During inverse Compton scattering these electrons can generate X-ray radiation at ∼12 keV by counterpropagating with an intense laser beam [Kär16]. First proof of concept measurements with a single-cycle THz source with an electric field of 30-50 MV/m already showed the possibility of accelerating electrons with THz radiation [Nan15]. Multi-cycle THz pulses seem even more beneficial for acceleration [Fak17]. Even though the energy of the THz pulses may not yet be sufficient enough to attain electron acceleration to the level of $10-20\,\mathrm{MeV}$ every step towards higher energies is an groundbreaking step to reach the goal.

Multi-cycle THz pulses are generated with a second order nonlinear optical process transferring the energy of the driving source in the infrared (IR) range to the THz range. Unfortunately the Manley-Rowe relations limit the energy conversion to an efficiency of $\eta = 10^{-3}$. Therefore to achieve mJ-level THz sources high energy laser sources at the J-level are required. The maximum conversion efficiency demonstrated reaches the Manley-Rowe limit only at pump pulse energies of a few milli Joule [Car15]. In order to realize J-level pumping a deeper understanding of the nonlinear process as well as the limiting factors is indispensable for the AXSIS project.

Outline of this thesis

After introducing the reason why strong field multi-cycle THz pulses are mandatory for the "table top" electron accelerator based on THz radiation – AXSIS – the optimizing techniques for the generation of high energy, multi-cycle THz pulses will be discussed. Thorough knowledge of the material properties of the optical crystals in the THz regime is a crucial factor to enhance the energy of the pulses. Therefore chapter 2 describes two different techniques applied to analyze optical properties in the low frequency range of 0.2 - 1 THz: the terahertz time domain spectrometer (THz-TDS) and the Fourier transform infrared spectrometer (FTIR). Moreover, the results of the optical properties in this regime are discussed for the materials investigated.

With this knowledge of the material, the generation of multi-cycle THz pulses will be explained in Chapter 3. Furthermore, the THz beam properties (section 3.2) and the experimental resources (section 3.3) as well as the experimental measurement tools (section 3.5) are described.

Chapter 4 and 5 describe two different techniques to drive the nonlinear process to generate strong field multi-cycle THz pulses in PPLN. Pumping the PPLN with a pulse-train of compressed, broadband pulses allows one to realize a higher pump fluence and therefore to increase the conversion efficiency (chapter 4). The limits of optical induced damage are characterized with this technique. To pump the PPLN with even higher energies, uncompressed pump pulses are used to generate the THz pulses. It is further explored, how delaying the uncompressed pulses may generate the necessary frequency content to drive the nonlinear process. As results the chirp-and-delay technique is described in chapter 5 based on three performed experiments:

- Chirp-and-delay via pulse train pulses of two pulses of equal energy followed by several lower energy pulses (section 5.1 and 5.2)
- Chirp-and-delay via two identical pulses generated with a Mach-Zehnder interferometer (section 5.3)
- Chirp-and-delay via two pulses with asymmetric chirp (section 5.4)

Chapter 6 summarizes the results and provides an outlook for future research directions with a special attention on the generation of narrowband, multi-cycle THz pulses.

2. Material analysis in the terahertz range

In order to design the THz generation setups deeper knowledge of the material properties in the THz band of potential candidates as THz sources is mandatory. Therefore, the material properties and the measurement tools for this low frequency range will be outlined in this chapter. First of all the focus will be on the measurement tools itself the terahertz time domain spectrometer (THz-TDS) and the Fourier transform infrared spectrometer (FTIR) and how they measure the important material parameters like refractive index and absorption coefficient.

Potential candidates as THz sources are characterized in the low frequency range to determine the optical properties for THz pulses. The focus is on nonlinear crystals to generate THz radiation and other materials like polymers and glasses.

2.1. Instruments for material analysis

The refractive index and the absorption coefficient of materials in the THz range are of crucial interest. The roadmap of *Dhillon et al.* shows the relevance of these parameter for the THz frequency range [Dhi17]. Two instruments have been used to analyze the optical material properties: the terahertz time domain spectrometer (THz-TDS) and the Fourier transform infrared spectrometer (FTIR). It will be analyzed how the instruments are used to determine the optical properties like the refractive index and the absorption coefficient.

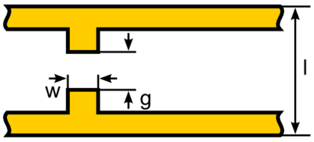

Figure 2.1.: Schematic of THz antenna: The distance l defines the THz frequency, the gap (g) is important for the gating laser pulse as well as the width (w).

2.1.1. Terahertz time domain spectrometer

THz time domain spectroscopy offers a great option to analyze the material properties in the THz regime. The THz-TDS is based on a stable, near-single-cycle THz-pulse, the THz beam-line and a fast detection scheme. To generate the THz pulse a photo-conductive (PC) switch, so called Auston switch [Aus83], is used. The pioneers in this field are *C. Fattinger and D. Grischkowsky* [Fat89]. The field of THz spectroscopy grew rapidly in the last three decades [Jep11].

Most of the THz-TDS systems are based on PC antennas gated by a short laser pulse. The PC antennas are highly efficient, generate a broadband THz pulse and can be used at high repetition rates in the megahertz range [Jep96]. A schematic example for such an antenna is shown in figure 2.1 [Mat97]. The antenna structure is made of metal lines grown on a low carrier lifetime semiconductor such as low temperature grown Gallium Arsenide (LT-GaAs). The biased antenna acts as a dipole if it is illuminated with a ultrashort laser pulse and generates a THz pulse [Jep96]. The center frequency ν of the pulse is defined by the distance l as dipole frequency given by

$$\nu = \frac{c}{2nl}, \tag{2.1.1}$$

where $n = 3.4$ is the refractive index of the GaAs and c the vacuum speed of light. The width and the gap size are matching the gating laser pulse (see figure 2.1) .

The detecting antenna take on the reverse process [Mit96]. The THz pulses are resolved by scanning an ultrafast laser pulse and measuring the current at the antenna. The antennas are well developed and are commercially available. The THz-TDS measures the time resolved electric field of a THz pulse and is therefore well suited for material analysis. The THz-TDS used in our laboratory is explained in the following section.

The terahertz time domain spectrometer of MenloSystems

A THz-TDS applies THz radiation to materials. It measures the sample effect on both the amplitude and the phase of the terahertz radiation. Our selected THz-TDS system Tera Sync of MenloSystems, schematic depicted in figure 2.2, is driven by an ultrafast fiber laser with a repetition rate of 100 MHz, a center wavelength of 1550 nm and a pulse duration of < 90 fs [MSG16]. These pulse are gating the emitter antenna (Tera15-TX-FC) biased with a high voltage of max. 120 V. The emitter antenna is capable to generate a single cycle THz pulse with a power up to 30 mW, if pumped at 1550 nm. A silicon lens on the antenna itself pre-collimates the THz pulse. Without the Si-lens the THz pulse expand too fast due to the wavelength of the THz pulse inhibiting the transport of the pulse. The transport of the THz pulse is accomplished with four TPX lenses, which have an effective focal length of about $EFL = 54\,\mathrm{mm}$. With the first lens the THz pulse collimates, the second lens focuses on the sample position marked with an iris, the third lens collects the transmitted THz pulse and collimates it. The last TPX lens focuses on the detector antenna, which has again a Si-lens in front capable to finally focus the small spot size on the antenna. The detector antenna (Tera15-RX-FC) as receiver is biased by the THz pulse. It can detect up to 40 mW of THz power at a repetition rate of 100 MHz using the 1550 nm pulse. The detected signal is amplified, converted with an A/D converter and saved.

The emitter antenna generates linear polarized THz radiation, therefore the precise orientation of the antennas is important for the performance of the THz-TDS. The linear polarized pulse allows the measurement of crystals properties which are polarization dependent in the THz regime like birefringence. The generated THz pulse and the inferred calculations will be discussed on the example of the ambient air containing a lot of undefined impurities.

Nitrogen purging

Within the common components in the air, water content is subject to great alterations. In addition water has absorption lines in the low frequency range. The interference with the measurements may become unpredictable. Thus the THz-TDS system performance is measured and compared, when used with air and purged with water free nitrogen. In

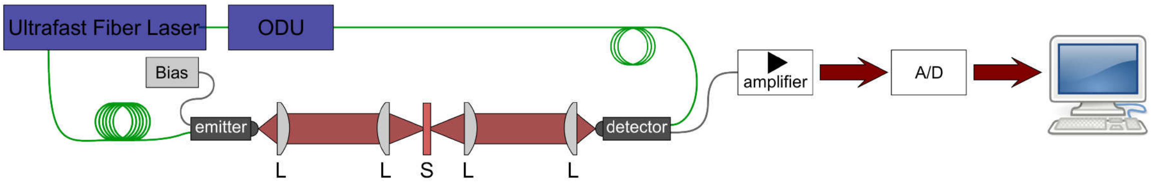

Figure 2.2.: Schematic setup of THz-TDS. **Key:** L: lens; S: sample; A/D: analog-to-digital converter.

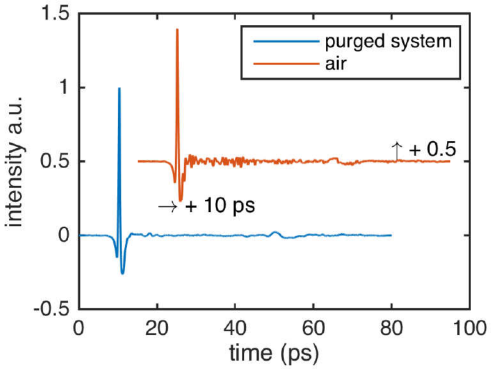

Figure 2.3.: THz pulses of a purged and non-purged system measured by the TDS. The pulse of the non-purged system (air) is shifted by 10 ps in time and 0.5 in intensity for a better visibility.

2.3 the influence of nitrogen and air on the THz pulse of the THz-TDS is illustrated as a simple visual check. To increase the visibility the THz-pulse in air is shifted by 10 ps in time and by 0.5 in intensity. Whereas the time remains unaffected the THz pulse in the purged system shows less noise than in air.

Using the fast Fourier transform (FFT) the THz pulse ($E(t)$) can be converted into the spectrum of the pulse ($E(\nu)$) as well as the corresponding phase ($\Phi(\nu)$) shown in figure 2.4. The spectrum of air clearly shows the absorption lines of water, while the nitrogen purged system has a smooth curve. This suggests that the noise in figure 2.3 trace back to the water absorption. As a further result of the FFT-spectrum the spectral range of the Menlo-THz-TDS system can be proven as greater 4THz with a maximal dynamic range of > 75 dB. To analyze now the optical properties of a sample, a reference and the sample are measured. It needs to be mentioned that the THz-TDS is just capable to measure samples of appropriated absorption and thickness. Outside these windows the sample

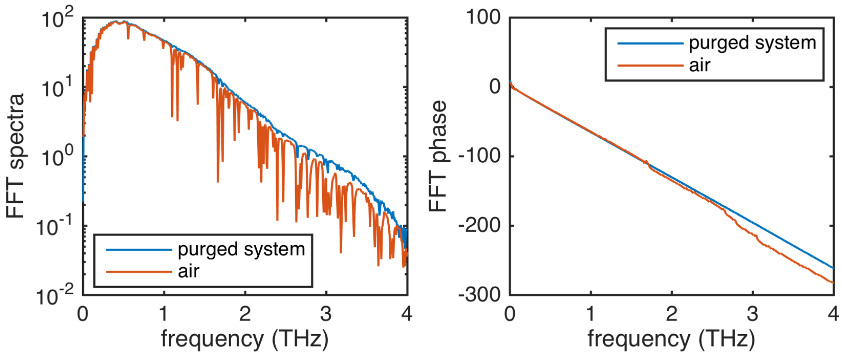

Figure 2.4.: FFT spectra and corresponding phase of the purged system and of air.

measurement or the high frequencies are in the noise level of the TDS and the measured values are not trustable.

Calculation of refractive index and absorption coefficient

To determine the refractive index n and the absorption coefficient α of a sample with the THz-TDS, the waveform of the THz electric field is analyzed with and without the sample. For illustration of the transmission spectroscopy a schematic is shown in figure 2.5. Based on this schematic the formulas of optical properties will be derived.

The incident THz pulse with an electric field E_r has a spectral intensity of

$$I_0 = \frac{c n_1(\nu)\epsilon_0}{2} \left|E_r(\nu)\right|^2 \tag{2.1.2}$$

At the surfaces of the sample this THz pulse experiences Fresnel losses, which are defined by the refractive index of the sample compared to the environment. In our case – normally air or nitrogen with $n_1(\nu) = 1$ – the Fresnel reflection and transmittance is given by

$$R(\nu) = \left|\frac{1 - n_2(\nu)}{1 + n_2(\nu)}\right|^2 \tag{2.1.3}$$

and

$$T(\nu) = 1 - R(\nu) = 1 - \left|\frac{1 - n_2(\nu)}{1 + n_2(\nu)}\right|^2 = \frac{4 n_2(\nu)}{(1 + n_2(\nu))^2}. \tag{2.1.4}$$

Leaving the first interface the intensity is reduced to

$$I_1(\nu) = T(\nu) I_0. \tag{2.1.5}$$

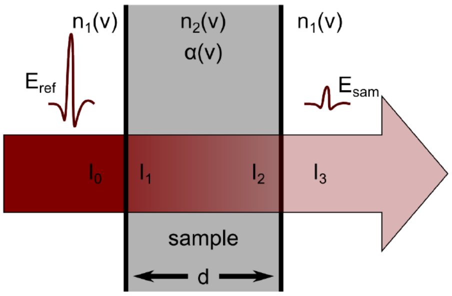

Figure 2.5: Schematic of transmission spectroscopy: THz pulse (E_{ref}) with an intensity I_0 is transmitted through a sample with thickness d, refractive index $n_2(\nu)$ and absorption coefficient $\alpha(\nu)$. Fresnel losses occur at each interface.

As the THz pulse is traveling through the sample with a thickness d the THz pulse experience absorption which results in an intensity of

$$I_2(\nu) = e^{-\alpha(\nu)d} I_1. \tag{2.1.6}$$

The THz pulse experiences Fresnel losses resulting in an output intensity of

$$I_3(\nu) = T(\nu)^2 e^{-\alpha(\nu)d} I_0. \tag{2.1.7}$$

The output field in relation to the input field is thus given by

$$E_s(\nu) = T(\nu) e^{-\alpha(\nu)d/2} E_r(\nu). \tag{2.1.8}$$

With an FFT of the direct measured THz waveform $E(t)$ the spectral range of the sample $E_s(\nu)$ and the reference $E_r(\nu)$ as well as the phase difference $\phi_s(\nu)$ and $\phi_r(\nu)$ are achieved. The phase shift

$$\begin{aligned}
\Delta\phi(\nu) &= \phi_s(\nu) - \phi_r(\nu) && (2.1.9)\\
&= \frac{2\pi\nu d}{c}\Delta n(\nu) && (2.1.10)\\
&= \frac{2\pi\nu d}{c}\left(n(\nu) - 1\right) && (2.1.11)
\end{aligned}$$

is used to calculate the refractive index [Jep05] as

$$n(\nu) = 1 + \frac{c}{2\pi\nu d}\left(\phi_s(\nu) - \phi_r(\nu)\right). \tag{2.1.12}$$

The absorption coefficient is calculated using equation 2.1.8 with the input and output field ($E_r(\nu)$ and $E_s(\nu)$) and the transmittance $T(\nu)$ (equation 2.1.4). Therefore the absorption coefficient is given by

$$\alpha(\nu) = -\frac{2}{d} ln\left(\rho(\nu)\frac{[n_2(\nu)+1]^2}{4n_2(\nu)}\right), \tag{2.1.13}$$

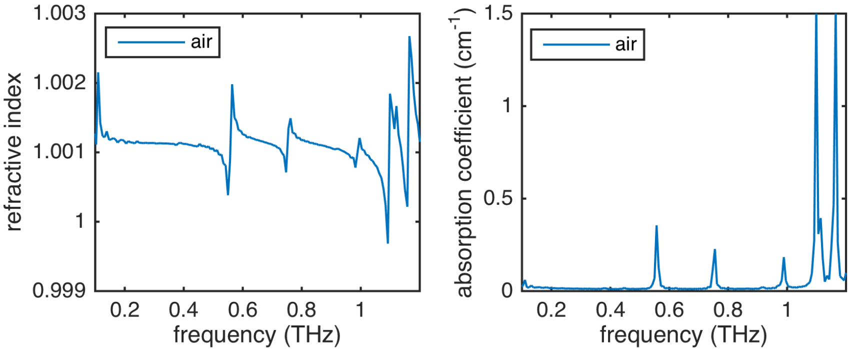

Figure 2.6.: Calculated refractive index and absorption coefficient of air with absorption peaks at 0.56 THz, 0.75 THz, 0.99 THz and at higher frequencies.

where $\rho(\nu) = \frac{E_s(\nu)}{E_r(\nu)}$ is the fraction of the electric fields [Jep05]. With these calculations the optical properties of a sample are determined.

The described standard calculations are applicable within certain limitations, e.g. the sample requires a certain thickness to avoid that the second Fresnel reflected pulse is interfering with the first pulse - the Fabry Perot effect. If the sample is too thin more sophisticated calculations are mandatory. Also lots of interfaces or thin layers on a substrate require calculations beyond the standard calculation. These calculations are well presented in literature [Jep05, Lee09]. For the samples used in this thesis the standard calculation is considered as adequate.

As example for the calculation the refractive index and the absorption coefficient of air are depicted in figure 2.6. Hereby the measured pulse in the purged system is the reference signal and the measured signal of the unpurged system with the 30 cm long beam path is the sample signal (see figure 2.3 and 2.4). The refractive index is as expected $n = 1$. Air has absorption peaks at 0.56 THz, 0.75 THz, 0.99 THz and at higher frequencies. Therefore Lorentzian peaks can be seen in the calculated refractive index at these frequencies. The absorption line at 0.56 THz is especially interesting for further THz experiments. The absorption coefficient is $\alpha(0.5\,\mathrm{THz}) = 0.4\,\mathrm{cm}^{-1}$. Experiments conducted in the range of that frequency should be performed in a setup purged with nitrogen or executed in vacuum to reduce absorption along the THz beam path.

Calculation of loss at sample

The losses of THz energy depend on the thickness of the sample and can be calculated using the refractive index and the absorption coefficient in the THz range. Using the refractive index $n(\nu)$ and assuming the sample is in air $(n = 1)$, we can calculate the Fresnel transmittance at the two surfaces:

$$T(\nu) = \frac{4n(\nu)}{(1 + n(\nu))^2}. \tag{2.1.14}$$

Knowing the absorption of a sample with a thickness d and the absorption coefficient α as

$$A(\nu) = e^{-\alpha(\nu)d}, \tag{2.1.15}$$

the intensity loss can be calculated with

$$\frac{I_{in}}{I_{out}} = T(\nu)^2 \cdot A(\nu) \tag{2.1.16}$$

$$= \left(\frac{4n(\nu)}{(1 + n(\nu))^2}\right)^2 \cdot e^{-\alpha(\nu)d}. \tag{2.1.17}$$

To illustrate the intensity loss for different thick Teflon plates, which we use to dump the remaining IR in the multi-cycle THz generation, the intensity loss is calculated and shown in table 2.1.

n	α(cm^{-1})	$T(\nu)$	d (cm)	$A(\nu)$	intensity loss
1.44	0.2	0.97	0.8	0.85	0.80
			1	0.82	0.77
			1.5	0.74	0.69
			2	0.67	0.63

Table 2.1.: Transmission for different thick Teflon plates at a frequency of 0.360 THz

Conclusion THz-TDS

The THz-TDS is a specific measurement tool, which allows the precise measurement of refractive index and absorption coefficient in the low frequency range up to 4 THz.

2.1.2. Fourier transform infrared spectrometer

The Fourier transform infrared (FTIR) spectroscopy is a technique to measure the reflectance or transmittance of a sample over a wide wavelength range [Gri83]. With the FTIR it is possible to cover a wide spectral range with a high spectral resolution. The base of this spectrometer is the fast Fourier transform of the measured interferogram, which calculates the spectrum of the sample either in transmission or reflection depending on the configuration.

For the measurements the FT-IR-Spectrometer VERTEX 80v of Bruker of the group of Andrea Cavalleri (Max Planck Institute of Structural Dynamics at the CFEL, Hamburg) is used. A schematic setup is depicted in figure 2.7. An FTIR spectrometer consists of a source, which is classically a light bulb to get the wide spectral range, the aperture to adjust the beam size to the detector, and then the main part the interferometer, where the interferogram is generated, with the fast delay line and the beam splitter. In this FTIR the whole spectral range from visible (VIS), over near-infrared (NIR) and mid-infrared (MIR) to far-infrared (FIR) and also up to the THz range is covered. Several sources and several beam splitters are easily exchangeable and open the wide spectral range. The whole system works in vacuum to avoid environmental interferences and to resolve the full spectral range. To measure the reflectance and the transmittance the generated interferogram is traveling through the sample compartment either used in reflection or in transmission. To allow also polarization dependent measurements the interferogram is polarized with the polarizer, adapted to the spectral range of the respective measurement. For each spectral range the appropriate detector has to be selected to reach the optimal sensitivity in the desired spectral range. The used combination of source, beam splitter and detector is listed in table 2.2.

As the sample holder of the FTIR is temperature controlled from liquid helium temperature (5 K) to a temperature higher than room temperature (300 K) measurements at specific temperatures are possible. Each measurement at the FTIR is referenced to a well characterized trace, for transmission just an empty holder and for reflection an uncoated gold mirror, where the reflection is well known. To achieve the transmission or reflection spectra the sample spectra are normalized to the reference. With the two

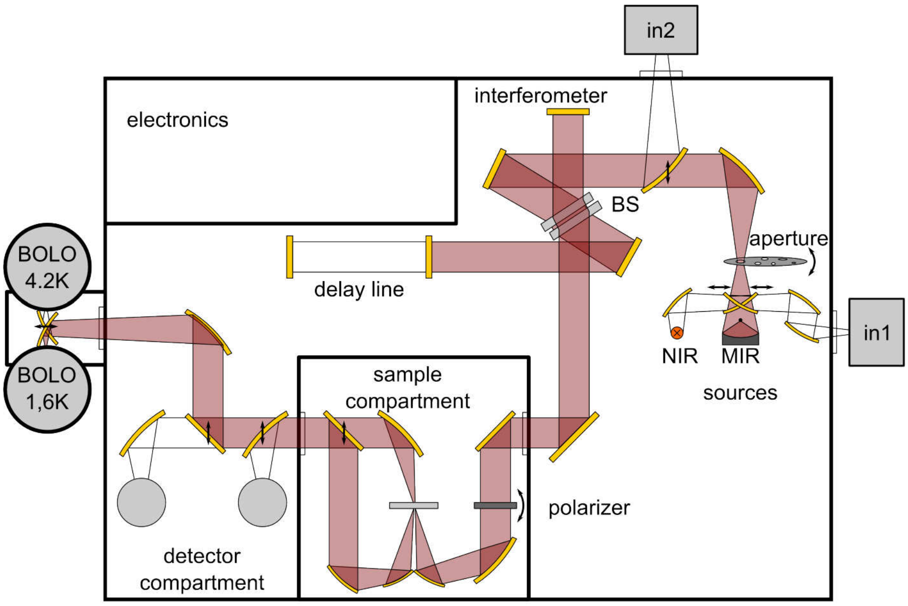

Figure 2.7.: Schematic drawing of the FTIR spectrometer VERTEX 80v of Bruker.

spectral range	WN (cm^{-}1)	source	beam splitter	detector
VIS	19000 - 9000	UV-VIS-NIR	CaF2	RT-Si
NIR	10000 - 4000	UV-VIS-NIR	CaF2	LN-MCT
MIR	7000 - 300	MIR	K-Br	LN-MCT
FIR	1000 - 80	MIR	Mylar Multilayer	RT-DTGS
THz high	90 - 9	FIR/MIR	Mylar Multilayer	Si-bolometer 4.2 K
THz low	40 - 6	FIR	Mylar 50	Si-bolometer 1.6 K

Table 2.2.: Source, beam splitter and detector for the desired spectral range and corresponding wavenumber (WN) used in the FTIR

spectra the extinction coefficient κ, the absorption coefficient α and the refractive index n are calculated [Cun92].

First of all the bulk reflectivity R is calculated with the measured reflectance R_0 and the measured transmittance T_0 with

$$R = \frac{-(R_0^2 - T_0^2 - 1 - 2R_0) - \sqrt{(R_0^2 - T_0^2 - 1 - 2R_0)^2 - 4R_0(2 - R_0)}}{2(2 - R_0)} \tag{2.1.18}$$

$$\text{and} \quad R = \frac{R_0}{1 + T_0 A}. \tag{2.1.19}$$

Therefore the absorption in the sample can be calculated with

$$A = \frac{1}{T_0}\left(\frac{R_0}{R} - 1\right). \tag{2.1.20}$$

With the known absorption $A = e^{-4\pi\nu\kappa d}$ of a sample with thickness d the extinction coefficient κ is known as

$$\kappa = -\frac{\ln A}{4\pi\nu d} \tag{2.1.21}$$

Thus the absorption coefficient α is defined as

$$\alpha = 4\pi\nu\kappa. \tag{2.1.22}$$

With the bulk reflectance R and the extinction coefficient κ the refractive index n can be calculated with

$$R = \frac{(n-1)^2 + \kappa^2}{(n+1)^2 + \kappa^2} \tag{2.1.23}$$

$$n = \frac{1 + R + \sqrt{4R - \kappa^2(1-R)^2}}{1 - R}. \tag{2.1.24}$$

The FTIR operates over the full frequency range from VIS to THz. The full capabilities are illustrated for lithium niobate. Figure 2.8 shows for the different spectral ranges (VIS/IR/MIR, MIR/FIR and THz) the reflectance (blue, yellow) and transmittance (red, violet) of lithium niobate with an ordinary (yellow, violet) and extraordinary (blue, red) orientation. In the VIS/IR/MIR the birefringence of lithium niobate is detectable. In the MIR/FIR spectral range the phonon resonances are well detectable as well as the absence of transmission. In the THz range the fringes are detectable as the thickness of the sample is in the range of the wavelength. The FTIR measurements in the THz range is suited to compare the results to the THz-TDS measurements.

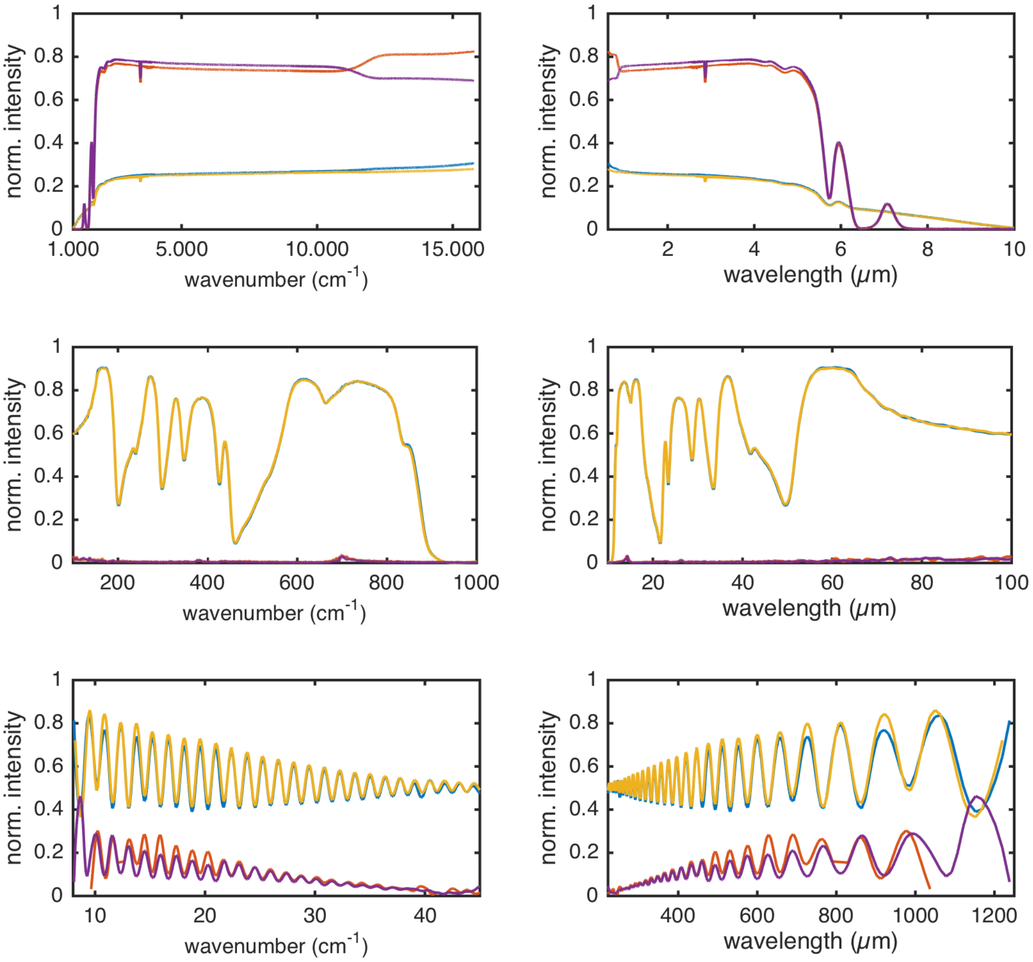

Figure 2.8.: FTIR measurement in the VIS-NIR-MIR (top), MIR-FIR (middle) and THz (bottom) range: reflectance (blue, yellow) and transmittance (red, violet) of lithium niobate vs wavenumber (cm^{-1}) (left) or wavelength (µm) (right) for the ordinary (yellow, violet) and extraordinary (blue, red) orientation.

2.2. Optical properties in the THz range

This section focuses on the linear optical properties in the THz regime of several nonlinear crystals which are regarded as candidate for THz generation, some polymers and glasses. They are measured mainly by the THz-TDS or by the FTIR. The relevant range for electron acceleration between 0.2 - 1 THz is discussed in detail. The full traces are shown in the appendix B.

2.2.1. Optical crystals for THz generation

Lithium niobate (LN)

Lithium niobate is a dielectric, ferroelectric, birefringent, uniaxial negative crystal with physical properties like linear electro-optical effect, piezoelectricity and pyroelectricity. An overview on the physical properties as well as the crystal structure is presented in the appendix A. This section characterize properties of lithium niobate ($LiNbO_3$) relevant in the THz range measured with the THz-TDS and FTIR. The nonlinear crystal $LiNbO_3$ has an effective nonlinear coefficient of $d_{eff} = 152.4$pm/V in the THz regime (section A.3.8).

All lithium niobate samples are commercially available. The samples investigated are purchased as wafers from Precision Micro-Optics Inc. or United crystals Inc. As doping of lithium niobate with magnesium oxide reduces the defects in the crystal growth and increases the conductivity and the damage threshold [O'B85] different doping concentrations of Magnesium oxide were selected and investigated. In figure 2.9 a schematic of different wafer cuts is depicted to explain the possible orientations of crystal axes to the laser polarization. The extraordinary axis of lithium niobate is the z-axis which is parallel to the c-axes of the crystal structure. The wafer is named with the axis which is perpendicular to the surface, therefore along the propagation of the optical pulse. The wafer is well defined by the primary flat indicating the other axis. With a x-cut and y-cut wafer the ordinary and extraordinary axis can be measured, the z-cut allows us to measure just the ordinary axes as the z-axis is perpendicular to the surface of the wafer. For this thesis a x-cut $LiNbO_3$ wafer, a x-cut 5 mol% MgO:$LiNbO_3$ wafer and a y-cut 6 mol% MgO:$LiNbO_3$ wafer are selected.

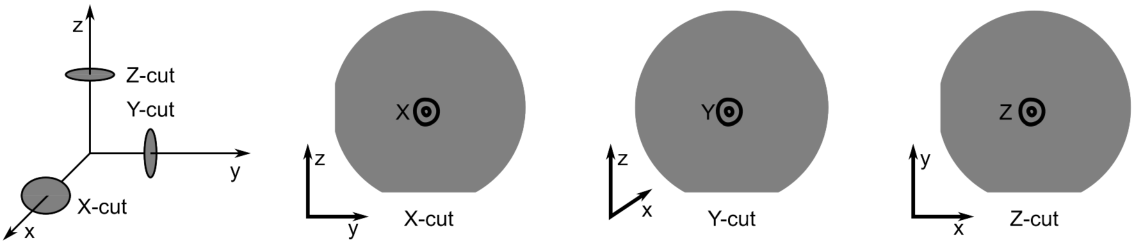

Figure 2.9.: Schematic of different wafer cuts of lithium niobate. The cut is defined by the axes which is normal to the surface. The axes, which is normal to the primary flat, is then defining the crystal axes in the wafer. The secondary flat is for an uniaxial crystal not necessary.

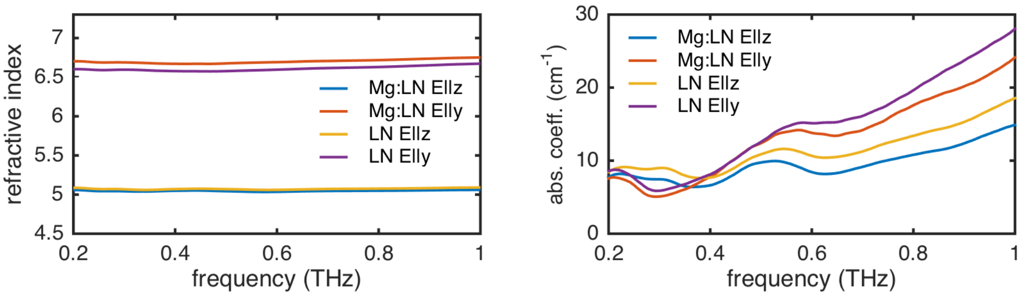

Figure 2.10.: Refractive index (left) and absorption coefficient (right) of lithium niobate and 5 mol% magnesium doped lithium niobate.

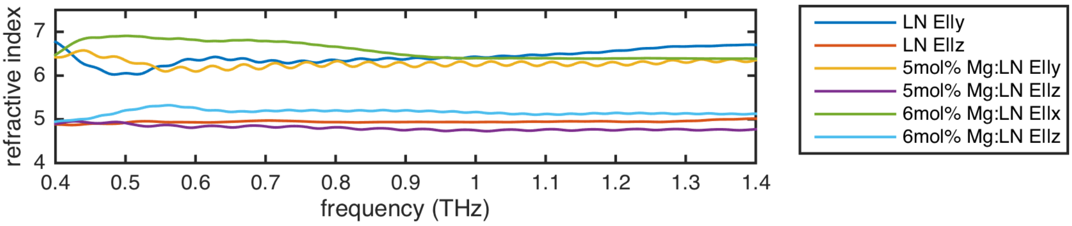

Figure 2.11.: Refractive index (left) of lithium niobate and magnesium doped lithium niobate at a temperature of 100 K.

Figure 2.10 shows the frequency dependence of the refractive index and the absorption coefficient of $LiNbO_3$ and 5 mol%MgO:$LiNbO_3$ at room temperature. The refractive index is nearly constant within the whole frequency range as the lowest phonon resonance of lithium niobate is at 7.6 THz [Koj02, Feu07]. The extraordinary refractive index ($E||z$) is lower then the ordinary ($E||x$ or $E||y$). Therefore lithium niobate is negative birefringent in the THz range. At 0.5 THz the refractive index is $n_o = 5.07$ and $n_e = 6.68$. The magnesium doping reduces the refractive index slightly to $n_e = 5.04$ and $n_o = 6.58$ at 0.5 THz. At 0.5 THz the absorption coefficient is $\alpha_e = 10.8\,\mathrm{cm}^{-1}$ for $LiNbO_3$, $\alpha_e = 9.8\,\mathrm{cm}^{-1}$ for Mg:$LiNbO_3$ and $\alpha_o = 12.5\,\mathrm{cm}^{-1}$ for both wafers. The absorption length, the length where the intensity is reduced to 1/e of the initial intensity, is about 1 mm at 0.5 THz. The absorption coefficient is increasing for higher frequencies which decreases the absorption length. Therefore, THz generation at higher frequencies is limited due to the high absorption in the crystal. The magnesium doping reduces also the absorption coefficient beneficial for the THz generation.

The resolution of the absorption coefficient for frequencies lower then 0.37 THz is limited due to the thickness of the sample (0.5 mm) as frequency resolution $d\nu$ from the FFT is given by:

$$d\nu = \frac{2\pi}{dt} = \frac{\pi\ c}{dl\ n} = 0.37\,\mathrm{THz}. \tag{2.2.1}$$

The data for higher frequencies could be fitted with a Drude-Lorentz model to resolve even the absorption coefficient at the frequency range lower the 0.4 THz. As the THz-TDS purged with nitrogen had a residual 4% relative humidity the absorption coefficient (figure 2.10 right) is slightly increased between 0.4 THz to 0.6 THz due to the absorption peak of air at 0.56 THz.

The birefringence of $LiNbO_3$ was confirmed by the measurement at the FTIR (see figure 2.11) at a temperature of 100 K. Drawback of the FTIR is the resolution of the measurement as well as the signal to noise ratio. As the refractive index is relative high, the photons counted at the detector were low deteriorating the resolution. As the refractive index is calculated with the extinction coefficient κ and the bulk reflectivity (see section 2.1.2) the precision on the refractive index is limited. Therefore the FTIR gives an estimate of the refractive index but for an accurate measurement of the refractive index, the THz-TDS is better suited.

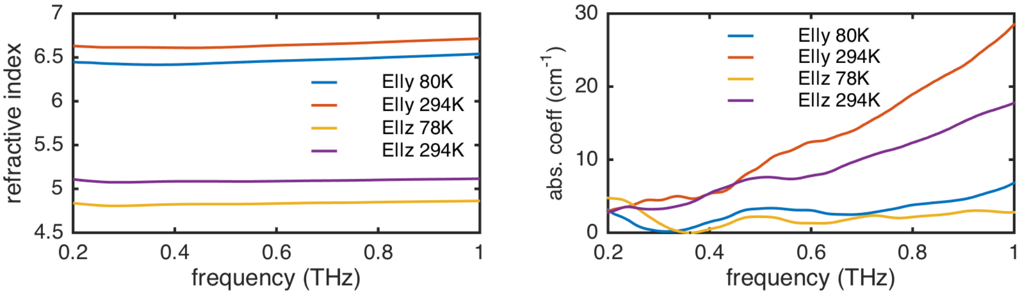

Figure 2.12.: Temperature dependence of the refractive index (left) and absorption coefficient (right) of 5 mol% magnesium doped lithium niobate.

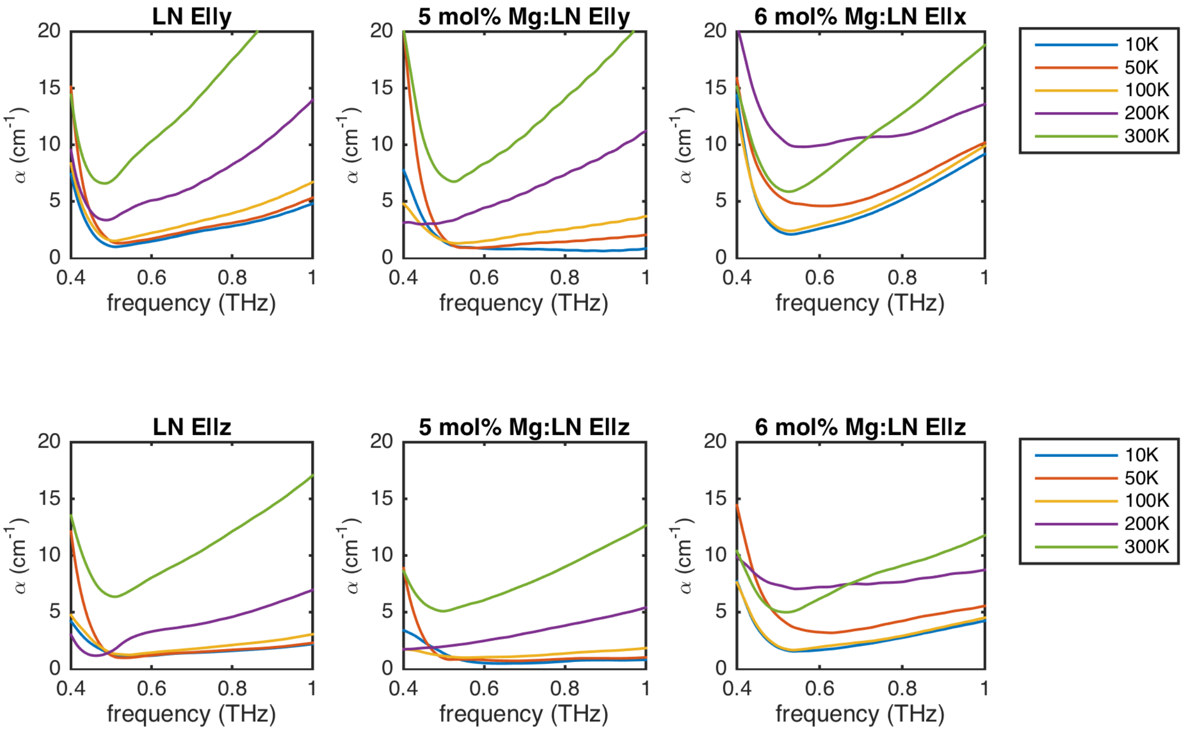

Figure 2.13.: Temperature dependence of the absorption coefficient for a x-cut lithium niobate wafer, a x-cut 5 mol% magnesium doped lithium niobate wafer and a y-cut 6 mol% magnesium doped lithium niobate wafer measured at the FTIR.

As *Pálfalvi et al* [Pál05] reported the refractive index and absorption coefficient are temperature dependent. Further measurements done by *Kiesling et al.* [Kie13], *Unferdorben et al* [Unf15], and our group [Wu15] supported the high relevance of this measurement. Figure 2.12 shows the refractive index and the absorption coefficient measured at room temperature and at cryogenic temperature (~ 80 K). Both values are decreasing for lower temperatures. At 0.5 THz the refractive indices decreases from $n_e(294\,K) = 5.08$ and $n_o(294\,K) = 6.62$ to $n_e(78\,K) = 4.82$ and $n_o(80\,K) = 6.44$, a difference of $\Delta n_e = 0.26$ and $\Delta n_o = 0.18$. The absorption coefficient is reduced by a factor of 3.44 from $\alpha_e(294\,K) = 7.5\,\mathrm{cm}^{-1}$ to $\alpha_e(78\,K) = 2.18\,\mathrm{cm}^{-1}$ and by a factor of 2.7 from $\alpha_o(294\,K) = 8.7\,\mathrm{cm}^{-1}$ to $\alpha_o(78\,K) = 3.2\,\mathrm{cm}^{-1}$.

The temperature dependence of the absorption coefficient is depicted in figure 2.13 for the calculated absorption coefficients measured at the FTIR for three different samples. This measurement was performed for several temperatures as the sample holder allowed us to tune the temperature. The absorption coefficient of all samples is valuable for frequencies higher then 0.55 THz due to the resolution of the FTIR limited by the beam size and the sample thickness. The absorption coefficient of the 6 mol% Mg:LN at 200 K is less reliable due to irregularities during the measurement. At the corner points the dependences are similar to the measured values of the THz-TDS which will be further discussed in section 2.2.1 (Absorption of lithium niobate). The absorption coefficient decreases from 300 K to 100 K substantially, but from 100 K to 10 K the decrease is less pronounced. This leads to the conclusion, that cooling the crystal to liquid helium temperature would be not worth the balancing higher cost of liquid helium with the expected improvement.

For confirmation the optical properties are measured at the Peking University at a THz-TDS with a temperature controlled liquid helium cryostat [Wu15]. The results are depicted in figure 2.14. The refractive index and the absorption coefficient show the same behavior as measured at our THz-TDS.

The high effective nonlinear coefficient and the low absorption at cryogenic temperature characterize $LiNbO_3$ as well suited material for efficient THz generation. The THz generation will be discussed in chapter 3.

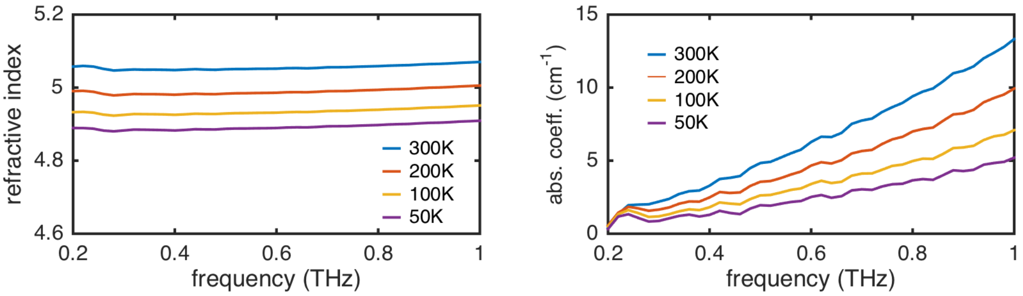

Figure 2.14.: Temperature dependent refractive index (left) and absorption coefficient (right) of 5 mol% MgO:LN for the extraordinary axis ($E||z$) (Data of [Wu15]).

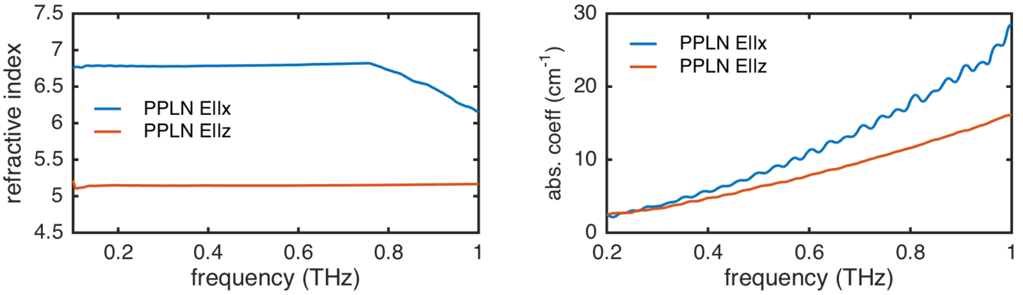

Figure 2.15.: Refractive index (left) and absorption coefficient (right) of 5 mm long 5 mol% periodically poled MgO:LN at room temperature.

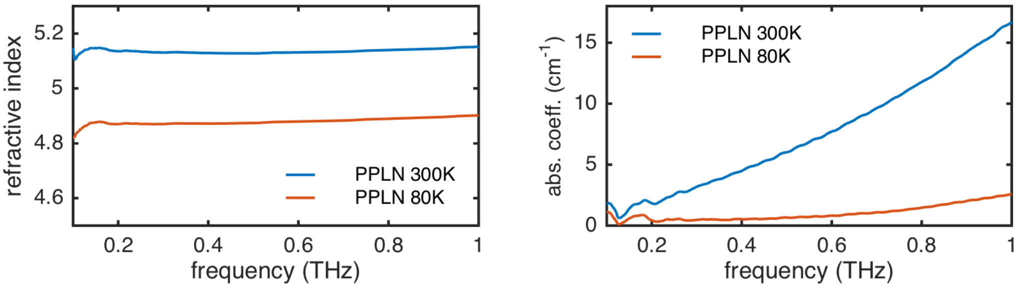

Figure 2.16.: Extraordinary refractive index (left) and absorption coefficient (right) of 5.05 mm long 5 mol% periodically poled MgO:LN at room and cryogenic temperature.

Periodically poled lithium niobate (PPLN)

Periodically poled lithium niobate (PPLN) is used to generate the multi-cycle THz pulses as described in chapter 3 in detail. For completeness of data the refractive index and the absorption coefficient, which are identical to the Mg:LN wafer, are depicted in figure 2.15. As the measured PPLN has a thickness of 5 mm the influence of the absorption is visible. The ordinary refractive index drops at a frequency of $\nu = 0.751\,\text{THz}$ and the lower extraordinary refractive index at $\nu = 1.3\,\text{THz}$ (see figure 2.15 and B.5). Higher frequencies are more strongly absorbed due to the higher absorption coefficient (see figure B.5 left). This measurement visualizes that crystals longer than the absorption length attenuate the transmitted THz pulse.

Lowering the temperature from room to cryogenic temperatures paves an additional effect as depicted in figure 2.16 showing the extraordinary refractive index and the absorption coefficient of a 5 mol% MgO:LN crystal. The refractive index is changed by $\Delta n = 0.26$ and the absorption coefficient is decreased at a frequency of 0.5 THz by a factor of 9. Table 2.3 summarizes the values in the low frequency range between 0.2 and 1 THz. The detailed error analysis can be found in the appendix C.

ν (THz)	0.2	0.3	0.4	0.5	0.6	0.7	0.8	0.9	1
n @ 80 K	4.87	4.87	4.87	4.87	4.88	4.88	4.89	4.89	4.9
n @ 300 K	5.14	5.13	5.13	5.13	5.13	5.13	5.14	5.14	5.15
$\alpha(\text{cm}^{-1})$ @ 80 K	0.42	0.46	0.53	0.66	0.82	1.09	1.48	2.03	2.6
$\alpha(\text{cm}^{-1})$ @ 300 K	1.82	3.2	4.46	6.02	7.72	9.63	11.8	14.2	16.8

Table 2.3.: Extraordinary refractive index and absorption coefficient of 5 mol% periodically poled MgO:LN with a length of 5.05 mm in low THz frequency range of 0.2 - 1 THz

Absorption coefficient of lithium niobate

Figure 2.17 summarizes the calculated absorption coefficients comparing the values at room temperature and cryogenic temperature for the different measurement tools (THz-TDS, the FTIR and the values of [Wu15]). The two room temperature curves for the PPLN and the Mg:LN wafer measured at our THz-TDS are similar. Also the room temperature curves of the FTIR and the THz-TDS at Peking University result in similar absorption

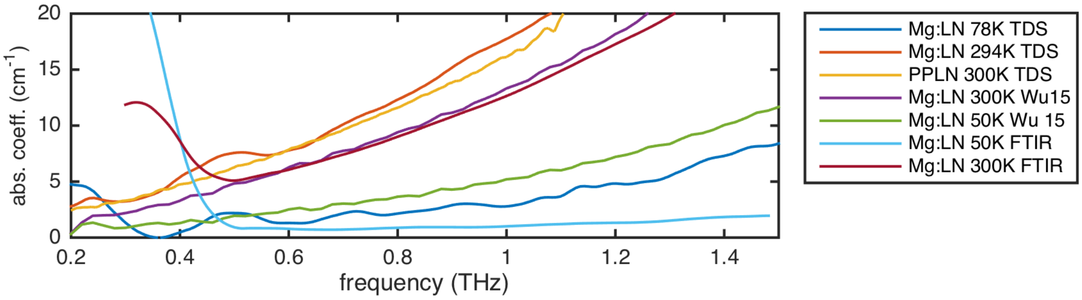

Figure 2.17.: Comparison of absorption coefficient between various 5 mol% periodically poled MgO:LN samples at different temperatures measured at the THz-TDS and the FTIR.

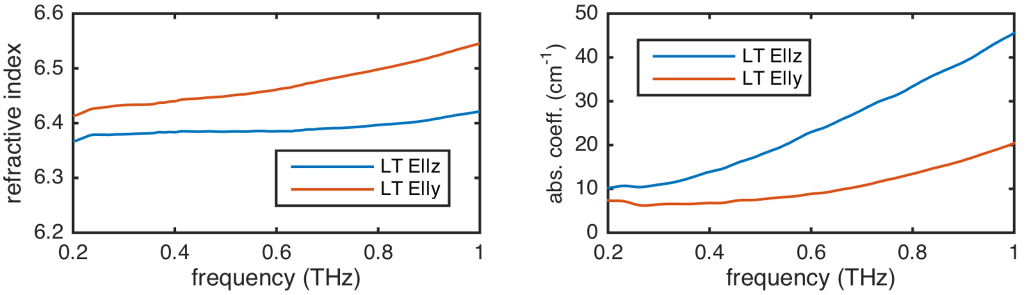

Figure 2.18.: Refractive index (left) and absorption coefficient (right) of lithium tantalate.

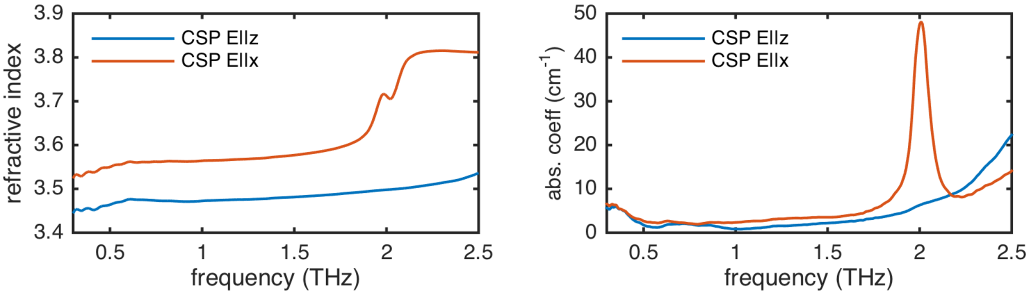

Figure 2.19.: Refractive index (left) and absorption coefficient (right) of CSP.

coefficients. The two pairs have a difference of 20% indicating the accurancy of the measurement tools compared to each other. At cryogenic temperatures the values are at all measurement techniques lower than at room temperature. It is worth to mention that the three values are in the same magnitude. The FTIR measures a 2 times lower value than our THz-TDS. The values demonstrated by *Wu et al.* is a factor 2 higher than our THz-TDS. Therefore this creates evidence that the true value can be expected in that range of $\alpha(0.6\,\text{THz}) = 1.5\,\pm 0.75\,\text{cm}^{-1}$.

As seen in this section the measurements of the absorption coefficient are complex and highly dependent on the sample and the measurement tool. To achieve consistence all samples should be measured at the same THz-TDS, if they are used in further experiments. Some additional possible candidates to generate THz radiation are measured at the THz-TDS and are described in the following subsections.

Lithium tantalate (LT)

Lithium tantalate ($LiTaO_3$ or LT) and lithium niobate ($LiNbO_3$) belong to the trigonal crystal system and have the same crystal structure. Lithium tantalate has the same optical properties as lithium niobate: $LiTaO_3$ is ferroelectric, linear electro optical, piezoelectric and pyroelectric [Smi71]. Lithium tantalate has a slightly lower nonlinear coefficient of $d_{33} = 145.2\text{pm/V}$ [Vod08]. In figure 2.18 the refractive index and the absorption coefficient of a 0.5 mm thick $LiTaO_3$ wafer (Precision Micro-Optics Inc.) are depicted. At 0.5 THz the extraordinary refractive index is $n_e = 6.6$ and the absorption coefficient is $\alpha_e = 17\,\text{cm}^{-1}$. Lithium tantalate is less birefringent than lithium niobate and both indices are higher, which is regarded as unfavorable for an efficient THz generation. Even not interesting at a first guess $LiTaO_3$ can be also poled [Mat91] and would be capable to generate multi-cycle THz pulses. As the absorption of coefficient is $> 15\,\text{cm}^{-1}$ over the full spectral range the generation would be less efficient.

Cadmium Silicon Phosphide (CSP)

In 2009, *Schunemann et al.* reported on the nonlinear optical crystal Cadmium Silicon Phosphide, $CdSiP_2$, a negative uniaxial II-IV-V_2 chalcopyrite compound semiconductor in the space group $42m$ which has a high nonlinear coefficient of $d_{36} = 84.5$ and can be grown

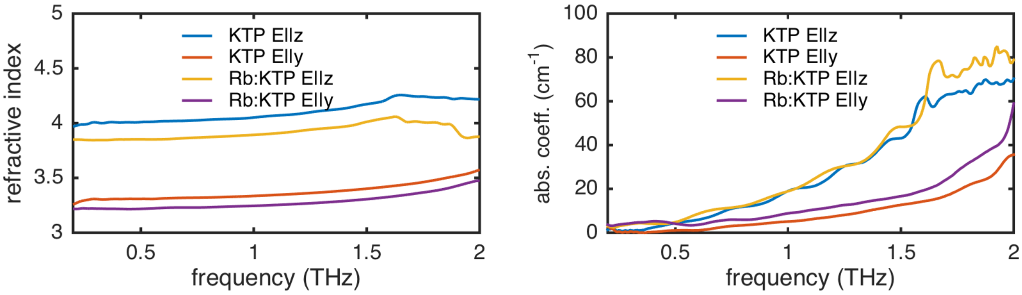

Figure 2.20.: Refractive index (left) and absorption coefficient (right) of KTP and Rb:KTP.

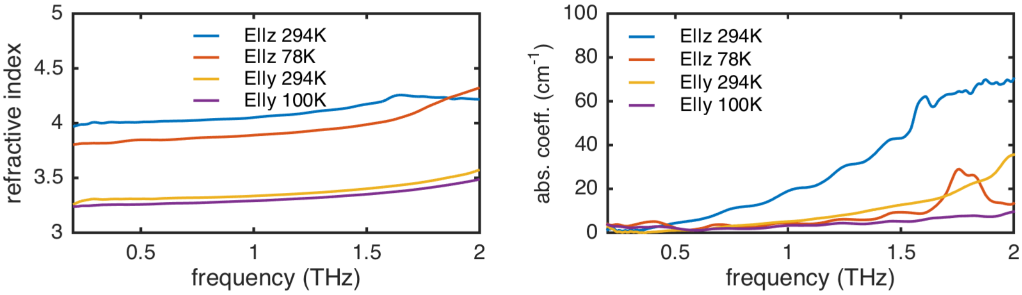

Figure 2.21.: Refractive index (left) and absorption coefficient (right) of KTP.

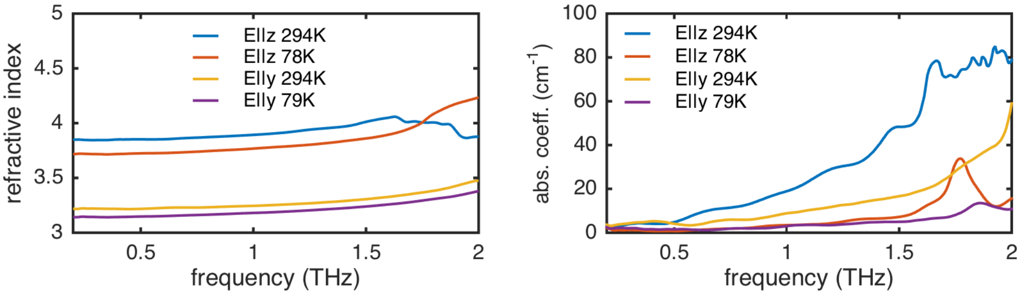

Figure 2.22.: Refractive index (left) and absorption coefficient (right) of Rb:KTP.

in a size sufficient for nonlinear optical devices [Sch09]. Therefore the optical properties in the THz range were measured. The crystal samples were produced by Schunemann. The refractive indices of $n_e = 3.47$ and $n_o = 3.56$ show the negative birefringence of the crystal (see figure 2.19 right). Promising for the THz generation is the low absorption coefficient at room temperature of $\alpha_e = 1.4\,\mathrm{cm}^{-1}$ and $\alpha_o = 2.4\,\mathrm{cm}^{-1}$ which could allow THz generation without cryogenic cooling of the crystal. The refractive index in the IR is in the range of $n = 3.1$ with a negative birefringence and could be pumped at 1 µm and higher [Sch09]. At 2 THz a dominant absorption peak occur on the x-axes. $CdSiP_2$ is considered as promising candidate for THz generation.

Potassium titanyl phosphate (KTP)

Potassium titanyl phosphate ($KTiOPO_4$ or KTP) is a orthorhombic (space group $Pna2_1$ (C_{2v}^9)) biaxial nonlinear crystal with a high damage threshold and the high nonlinear coefficient [Tho90, Han00]. KTP can be poled for efficient nonlinear processes [Pas98]. The measured samples, a x-cut KTP crystal (6Wx3Hx1.35L) and a x-cut Rubidium doped KTP (8Wx5Hx1.7L), are produced by the KTH Royal Institute of Technology in Stockholm in the group of Frederic Laurell. They are measured with a 3 mm pinhole which limits the resolution in the low frequency range. As KTP is a biaxial crystal the sample was not applicable to measure all axes, but the two ordinary axes (x and y) have a similar refractive index at $n = 3.3$ [Ant14]. The refractive index and the absorption coefficient is trustable above 0.5 THz. The refractive index and the absorption coefficient in the THz range of KTP and rubidium doped KTP is depicted in figure 2.20. The refractive index on the main optical axes (z-axis) is measured to be $n_o = 4$ with an absorption coefficient at 1 THz of $\alpha_o = 19\,\mathrm{cm}^{-1}$ for KTP and $n_o = 3.8$ for Rb:KTP with an absorption coefficient at 1 THz of $\alpha_o = 19\,\mathrm{cm}^{-1}$. At a frequency of $\nu = 1.75$ THz an absorption peak on the main optical axis is detectable which is already reported in the literature [Ant14]. Cooling both crystals reduces again both optical parameter. Figure 2.21 shows the temperature dependent refractive index and the absorption coefficient for KTP. The extraordinary refractive index is reduced by $\Delta n = 0.15$ and the extraordinary absorption coefficient is reduced to $\alpha_o = 1.8\,\mathrm{cm}^{-1}$ at 0.8 THz. The temperature dependent refractive index and the absorption coefficient for Rb:KTP is depicted in figure 2.22. The extraordinary

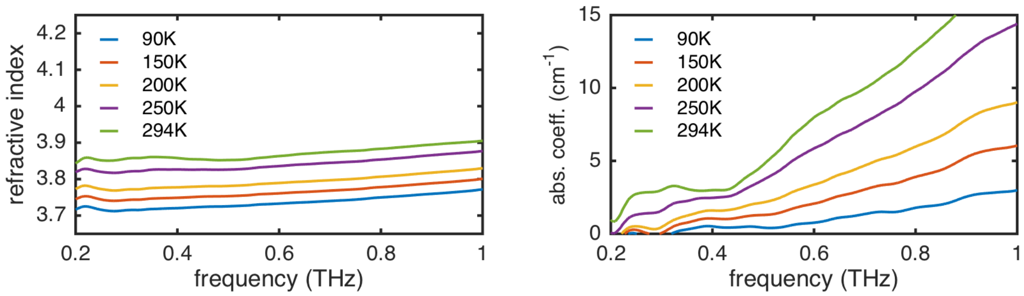

Figure 2.23.: Refractive index (left) and absorption coefficient (right) of Rb:KTP for various temperatures.

refractive index is reduced by $\Delta n = 0.1$ and the extraordinary absorption coefficient is reduced to $\alpha_o = 2\,\mathrm{cm}^{-1}$ at 0.8 THz.

Additional benefit of cooling was investigated by stepwise reduction of the temperature. Hereby the crystal was mounted on a 4.5 mm pinhole and cooled with liquid nitrogen. The intermediate temperatures (250K, 200K and 150K) were measured while cooling the crystal from room temperature to cryogenic temperature with a temperature error of ± 10 K. The bigger aperture allows us to measure also the lower frequencies with a smaller error on both values (see appendix C). The influence on the extraordinary refractive index and the absorption coefficient of a Rb:KTP is depicted in figure 2.23. The refractive index of Rb:KTP is changed via cooling by $\Delta n = 0.13$ to $n = 3.73$ and the absorption coefficient is decreased at a frequency of 0.6 THz by a factor of 10 to $\alpha_e = 0.76\,\mathrm{cm}^{-1}$. Table 2.4 summarizes the values for 90 K, 200 K and 294 K in the low frequency range between 0.36 and 1 THz. The absorption coefficient is already at a temperature of 200K in the order of $\alpha = 1.5\,\mathrm{cm}^{-1}$. This opens the possibility to cool the crystal with cheaper techniques than cooling by liquid nitrogen.

With KTP crystals *Wu et al.* [Wu16] demonstrated first generation experiments in the THz range. The effective nonlinear coefficient is half compared to lithium niobate, but the damage threshold of KTP is more than twice then in lithium niobate. Therefore KTP could be considered as a possible material for high energy THz generation.

ν (THz)	0.36	0.4	0.5	0.6	0.7	0.8	0.9	1
n @ 90 K	3.72	3.72	3.73	3.73	3.74	3.75	3.76	3.77
n @ 200 K	3.78	3.78	3.78	3.79	3.8	3.81	3.82	3.83
n @ 294 K	3.86	3.86	3.85	3.86	3.87	3.88	3.89	3.91
$\alpha(\mathrm{cm}^{-1})$ @ 90 K	0.35	0.51	0.42	0.76	1.35	1.79	2.55	3.01
$\alpha(\mathrm{cm}^{-1})$ @ 200 K	1.32	1.6	2.16	3.37	4.67	6	7.83	9.05
$\alpha(\mathrm{cm}^{-1})$ @ 294 K	3.01	2.99	4.78	7.99	9.96	12.6	15.7	18.5

Table 2.4.: Temperature dependent extraordinary refractive index and absorption coefficient of Rb:KTP in low THz frequency range of 0.36 - 1 THz

2.2.2. Polymers and glass

All THz generation experiments within this thesis are using several materials additional to the non-linear crystal, e.g. to block the IR-pump in the generation setup. This section collects all materials, which are used in the experiments, and discusses the measurement of the samples with the THz-TDS. There are first several polymers, mostly with low absorption in the THz frequency range, followed two glass plates e.g. to obtain the transmittance for the cryo-dewars.

Polytetrafluoroethylene (PTFE)

Polytetrafluoroethylene (PTFE) is widely known as Teflon and is a white polymer with a good transmittance in the far infrared frequency range. If the Teflon is thick enough it is a great candidate to block the IR light due to the relatively high absorption in the near IR. The transmission of the THz light remains unaffected. In figure 2.24 the measurements at the THz-TDS of Teflon plates with a nominal thickness of 10 mm, 15 mm, and 20 mm are shown. In these measurement it is shown that the THz pulse of the THz-TDS is delayed for each thickness differently, for example the d = 10 mm thick plate delays the pulse by $\Delta t = 14.78\,\mathrm{ps}$. With this delay the estimated refractive index can be calculated via

$$n = \frac{\Delta t \cdot c}{d_p} + 1, \tag{2.2.2}$$

where d_p is the precise thickness. In table 2.5 the estimated refractive index due to the delayed pulses is depicted. The precise thickness d_p of the plates has been measured for each plate with a digital calliper and is displayed in column 2. Comparing this estimated

d (mm)	d_p (mm)	Δt (ps)	n
10	10.4	14.78	1.426
15	16.36	23.99	1.439
20	21.96	31.26	1.427

Table 2.5.: Transmission for different thick Teflon plates at a frequency of 360 GHz

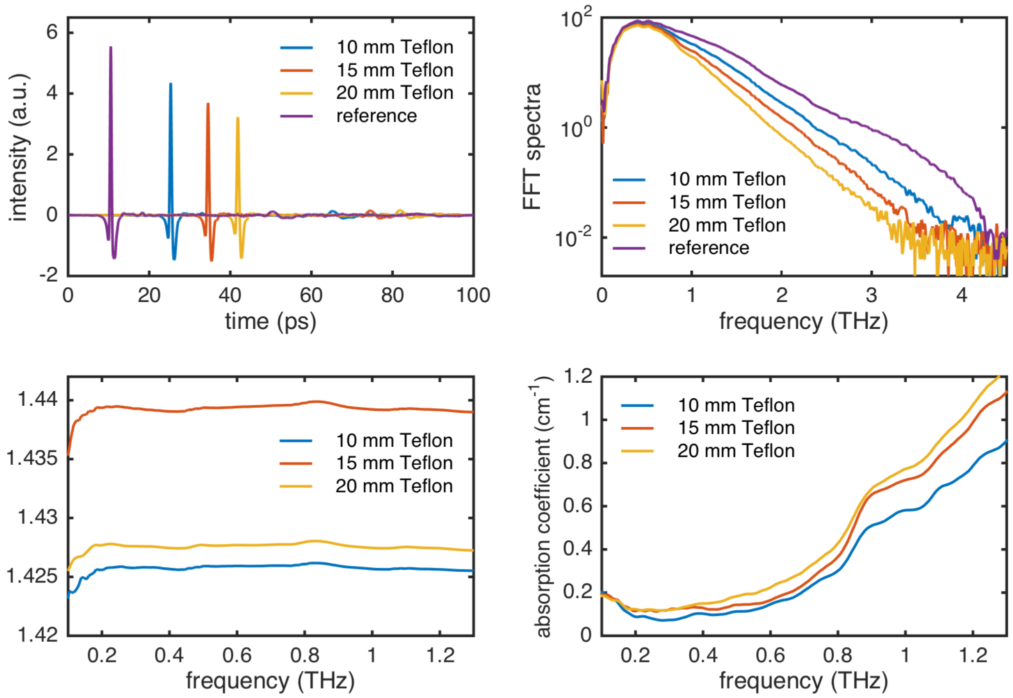

Figure 2.24.: THz-TDS results for different thick Teflon plates: THz-pulses for 10 mm, 15 mm, and 20 mm plates (top left), corresponding FFT spectra (top right), refractive index for the different plates (bottom left), and absorption coefficient (bottom right).

refractive index to the measured refractive index in figure 2.24 (bottom left) both are in good agreement due to the refractive index remaining flat over the whole frequency range. This low refractive index results in low Fresnel reflection on the surface of about 3%.

Important for the measurements is the absorption coefficient α in the low frequency range (figure 2.24 bottom right) which is in the order of 0.2cm^{-1}. This leads to the losses calculated in table 2.1.

Polymethylpentene (TPX)

Polymethylpentene known as TPX is transparent in the frequency range of UV, VIS, NIR and also in the THz range. TPX has the same refractive index over the whole frequency range with about 1.46. Therefore, TPX lenses are a great candidate to be used in the experimental setups, due to the possibility of pre-alignment in the VIS or NIR of the THz setups. In figure 2.25 the refractive index and the absorption coefficient measured by the THz-TDS are shown. The absorption coefficient is in this frequency range around 0.4cm^{-1}, which leads again in low losses for TPX optics.

Polyethylene (PE)

Polyethylene (PE) is a relatively soft plastic, which has again a relative low refractive index in the THz frequency range (see figure 2.26). As the absorption coefficient is higher then for the other polymers (1.7cm^{-1}), PE should not be the ideal candidate as THz material, but PE has his benefit in the low transmission in the NIR spectral range. Therefore PE is mainly used to protect the energy detectors from scattered or direct IR pump light in the THz setups.

Acrylonitrile butadiene styrene (ABS)

Acrylonitrile butadiene styrene, short ABS, is a thermoplastic polymer, which is a hard plastic. It is well-known from Lego bricks. The capability to use them in 3D-printers is the reason for looking into this material. Compared to the other polymers the refractive index is larger as seen in figure 2.27 and the absorption coefficient is extremely high for a polymer with 5cm^{-1}. Therefore, this material is not suitable for THz applications.

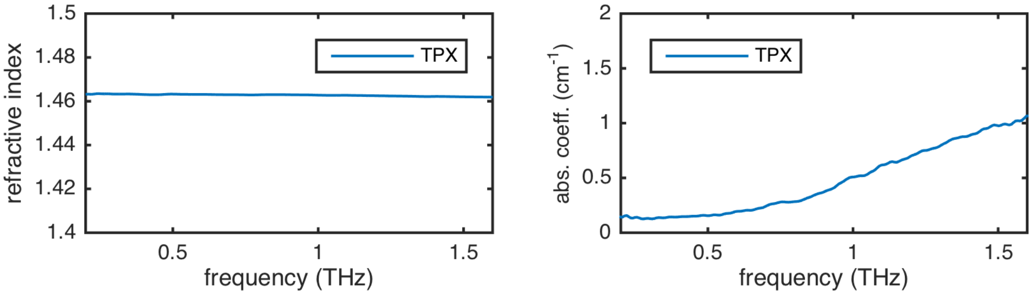

Figure 2.25.: Refractive index (left) and absorption coefficient (right) of Polymethylpentene (TPX).

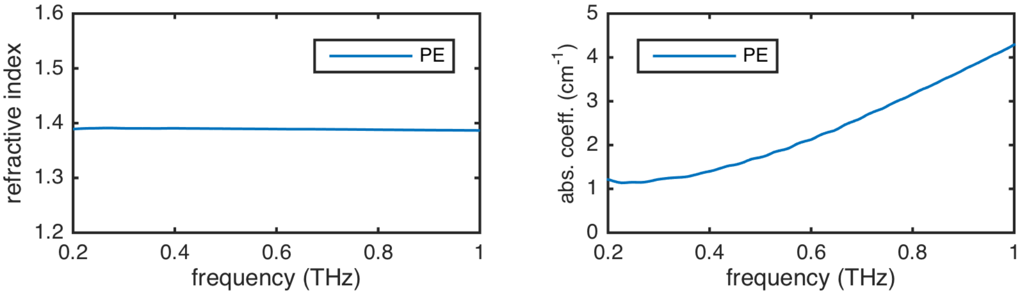

Figure 2.26.: Refractive index (left) and absorption coefficient (right) of polyethylene.

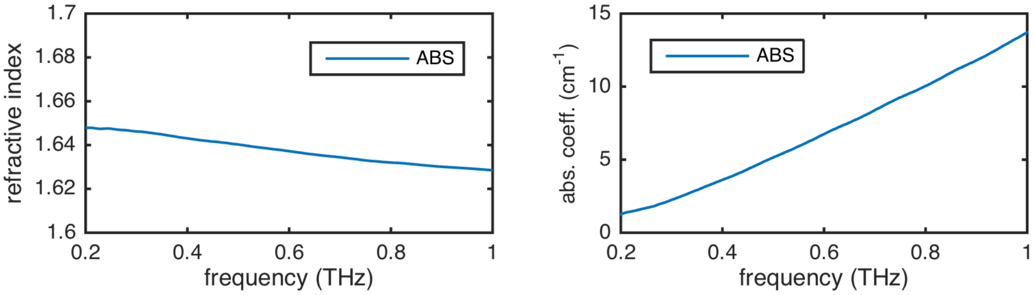

Figure 2.27.: Refractive index (left) and absorption coefficient (right) of ABS.

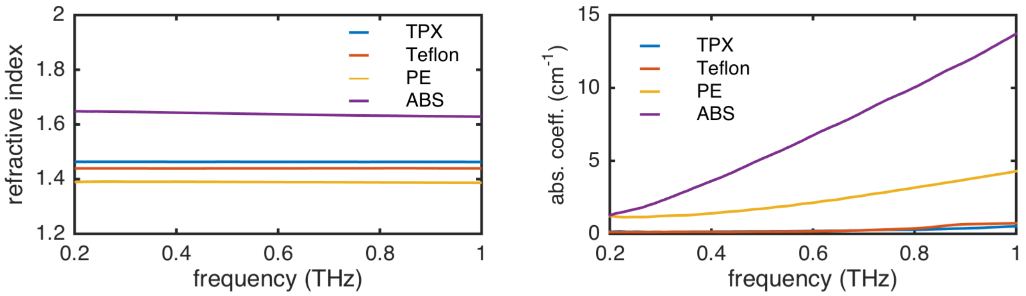

Figure 2.28.: Summary of refractive index (left) and absorption coefficient (right) of different polymers.

Summary polymers

Polymers are well suited for THz optics due to the low absorption and the low refractive index in the THz frequency range. Excluding of ABS all of the measured samples are used in different parts of the THz beam lines. Figure 2.28 displays all measured polymers as overview.

Glass windows

Optical glass windows are used in vacuum chambers to transmit the infrared laser pulses as well as the generated THz pulses. The windows are made of sapphire (Al_2O_3) or fused silica (SiO_2 or FS) with an AR coating for the infrared, which is not influencing the THz pulses as the coating is too thin compared to the wavelength. Figure 2.29 shows the refractive index and the absorption coefficient for a 3 mm thick sapphire window and 0.2 mm thick fused silica window. As the fused silica window is so thin the Fresnel reflections are not distinguishable from the main pulse resulting in a modulation of the refractive index as well as of the absorption coefficient. To calculate the actual values the modulated function is fitted with

$$n = 0.001256\nu^2 - 0.002047\nu + 2.105 \tag{2.2.3}$$

$$\alpha = 3.25\nu^2 - 2.63\nu + 0.68 \tag{2.2.4}$$

This fit is just a guide to the eye. A more accurate fit could be reached with the Drude-Lorentz model including the phonon peaks at the high frequencies.

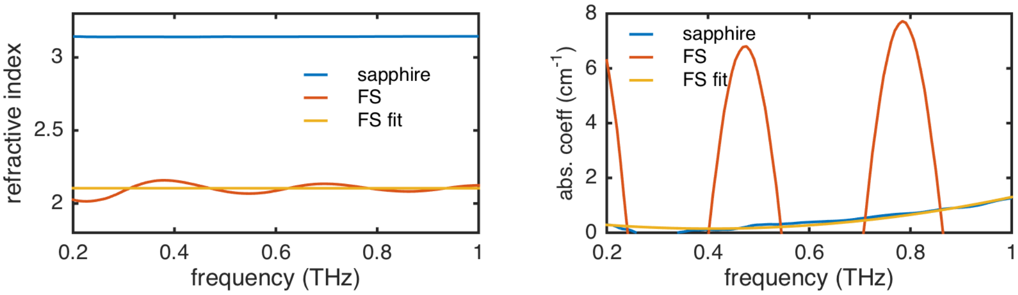

Figure 2.29.: Summary of refractive index (left) and absorption coefficient (right) of a sapphire and a fused silica window.

At 0.5 THz the refractive indices are $n_{sapp} = 3.14$ and $n_{FS} = 2.1$ and the absorption coefficient is $\alpha_{FS} = 0.28\,\mathrm{cm}^{-1}$ and $\alpha_{FS} = 0.18\,\mathrm{cm}^{-1}$. The absorption of both is low in the desired frequency range which is favorable for the transmission of the THz pulses through the windows.

2.3. Summary

This chapter provides a thorough overview on the optical material properties in the THz frequency range, mainly the refractive index and the absorption coefficient. Two different measurement tools, the THz-TDS and the FTIR, are introduced and the estimated material properties are discussed. The capabilities for the applied measurement tools are elaborated. With this knowledge a deeper insight into optical crystals, which are promising for the THz generation due to the high nonlinearity known from the infrared region, is achieved. The properties of polymers used for THz optics are also presented.

In conclusion, this chapter is a reference chapter for several material properties in the THz frequency range and the explanation chapter for analyzing even more samples in this regime with the presented measurement tools.

3. Overview of multi-cycle terahertz generation in periodically poled lithium niobate

Multi-cycle THz pulses can be generated via optical rectification (OR) or difference frequency generation (DFG) in periodically poled lithium niobate (PPLN) crystals. The theoretical background of THz generation in PPLN is introduced in this chapter. The quasi phase-matching (QPM) as underlining nonlinear process as well as the theoretical description of the THz generation via different pumping schemes is described. Two techniques of generating high energy pulses are introduced. Furthermore, the experimental resources such as the PPLN and the driving lasers are presented. The THz measurement tools essential for the experiments executed in this thesis are described in detail.

3.1. Theoretical background

The underlying nonlinear processes are described in textbooks like references [Boy03, Sut03] for the optical range and can be straight forwardly transferred to the THz range. The generation of THz pulses is based on the second order nonlinear process proportional to the second order nonlinear coefficient χ_2 as reference [Xu92] already describes. The following section summarizes the theoretical background of multi-cycle THz generation in PPLN based on the theory of *K. Vodopyanov* [Vod06]. Other sources are given according to necessity.

3.1.1. Quasi phase-matching

Basic description of quasi phase-matching for second harmonic generation and difference frequency generation was transferred to the THz regime in the early 2000's by [Lee00, Wei01, Lee01]. In the following the quasi-phase matching to generate THz pulses via difference frequency generation is described.

In order to generate THz radiation efficiently the wave-vectors of the interacting waves have to be zero to fulfill the phase-matching condition in the THz regime [Vod06]:

$$\Delta k(\Omega) = k(\Omega) + k(\omega) - k(\omega + \Omega) = 0, \tag{3.1.1}$$

assuming the angular THz frequency Ω, the angular IR frequency ω and the by Ω shifted angular IR frequency $\omega + \Omega$. The refractive index in the optical and the THz range of the crystal material used for THz generation is necessary to calculate the mismatch Δk as $k(\omega) = \omega n(\omega)/c$. As lithium niobate has a high refractive index in the THz regime of $n_{\mathrm{THz}} \sim 5$ as described in chapter 2 compared to the optical range ($n_{\mathrm{IR}} = 2.17$) the pulses mismatch prematurely. The coherence length l_c

$$l_c = \frac{\pi c}{\Omega(n_{\mathrm{THz}} - n_{\mathrm{IR}})} \tag{3.1.2}$$

describes the limit of the interaction length of the IR pulse and the THz pulse [Yaj70]. By inverting the polarization of the domains in the PPLN after the coherence length l_c the THz is generated efficiently via quasi-phase matching (see figure 3.2 left top). After the coherence length l_c a half cycle of the THz pulse is generated. The crystal length of the PPLN is defined by

$$N \cdot 2 \cdot l_c = N \cdot \Lambda, \tag{3.1.3}$$

where Λ is the domain period generating a full THz cycle and N the number of periods. As example, the coherence length for a THz pulse with a frequency of 0.36 THz is $l_c \approx 150\,\mu\mathrm{m}$ and for a frequency of 0.54 THz $l_c \approx 100\,\mu\mathrm{m}$.

Quasi-phase matching is introduced with a grating on the PPLN [L'h07a, L'h07b]. The ferroelectric domain of $\mathrm{LiNbO_3}$ is inverted periodically to achieve the poled structure. The grating wave vector is known as

$$k_{QPM} = \frac{2\pi}{\Lambda}, \tag{3.1.4}$$

where Λ is the poling period of the PPLN [Fej92]. The wave-vector mismatch Δk has to be amended by k_{QPM} to

$$\Delta k(\Omega) = k(\Omega) + k(\omega) - k(\omega + \Omega) - k_{QPM}. \tag{3.1.5}$$

Figure 3.1 shows the wave-vector picture for such a quasi-phase matching out of scale.

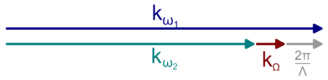

Figure 3.1.: Schematic wave-vector picture for quasi-phase matching.

As the generated frequency is far away from the driving frequency the interacting driving waves are close to each other. Therefore the wave-vectors of the IR has to be rewritten to

$$k(\omega + \Omega) - k(\omega) = \Omega \frac{dk}{d\omega}, \tag{3.1.6}$$

where $\frac{dk}{d\omega}$ is the group velocity of the IR n^{gr}_{opt} [Yaj70, Nah96]. Consequently, the wave-vector mismatch is

$$\Delta k(\Omega) = \frac{\Omega}{c} \left(n_{\text{THz}} - n^{gr}_{\text{opt}} \right) - \frac{2\pi}{\Lambda}. \tag{3.1.7}$$

At the optimal case the wave-vector mismatch is zero to generate efficiently the desired frequency. Thus the generated angular frequency is depending on the poling period via

$$\Delta k(\Omega) = 0 \tag{3.1.8}$$

$$\Rightarrow \frac{\Omega}{c} \Delta n = \frac{2\pi}{\Lambda} \tag{3.1.9}$$

$$\Omega = \frac{2\pi c}{\Lambda \Delta n} \tag{3.1.10}$$

where the index mismatch is introduced as $\Delta n = n_{\text{THz}} - n^{gr}_{\text{opt}}$. As the angular frequency $\Omega = 2\pi\nu$ the generated frequency ν is given by

$$\nu = \frac{c}{\Lambda \Delta n}. \tag{3.1.11}$$

In figure 3.2 the different cases (i) no phase matching, (ii) quasi-phase matching and (iii) perfect phase-matching are depicted (left). As equation 3.1.11 describes, the desired frequency is depending on the poling period of the PPLN and the difference between the refractive indices. As the refractive index in the THz regime varies with temperature for a given frequency, the generated frequency changes for the specific poling period. Figure 3.2 (right) shows the poling period in the low frequency regime for two temperatures (300 K and 100 K).

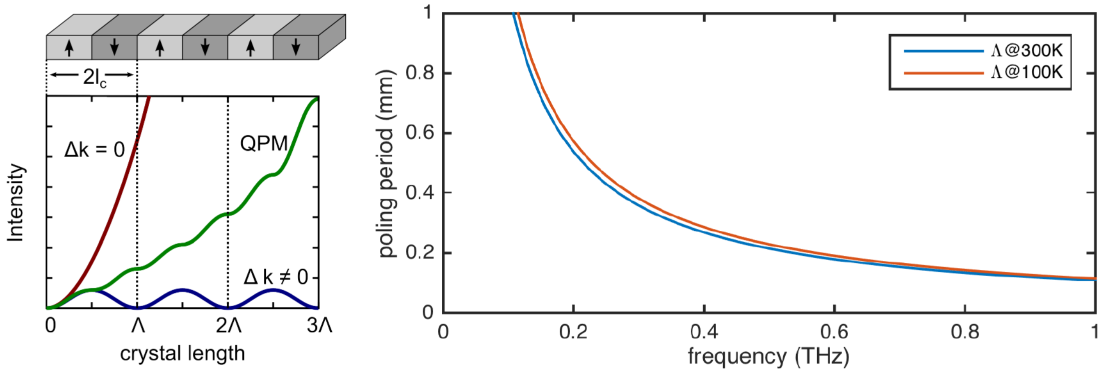

Figure 3.2.: Quasi phase-matching in periodically poled lithium niobate. **Left:** Comparison of no phase-matching $\Delta k \neq 0$ (blue), quasi-phase matching (green) and perfect phase matching $\Delta k = 0$(red) for a PPLN with a poling period of $\Lambda = 2l_c$. **Right:** Poling period Λ at the various frequencies for room- (300 K) and cryogenic temperature (100 K).

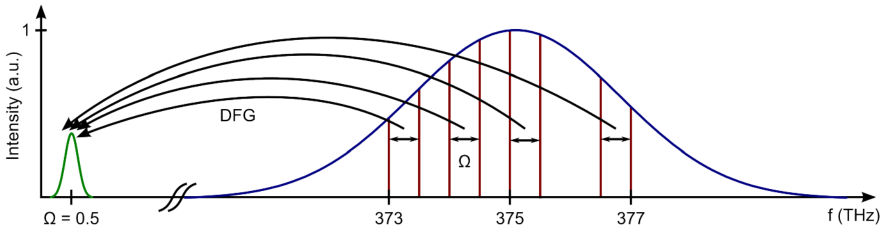

Figure 3.3.: Schematic concept of optical rectification. The broadband IR pulse generates THz via intra-pulse DFG.

3.1.2. Optical rectification

A compressed pump pulse with a broad bandwidth can be used to generate THz pulses via intra-pulse DFG called optical rectification. To support the THz frequency the bandwidth needs to exceed a minimal bandwidth. Figure 3.3 shows a schematic drawing of OR for a broadband IR pulse at a center wavelength of 800 nm (i.e. 375 THz) generating a narrowband THz pulse at 0.5 THz.

To generate the THz pulse the poled $\mathrm{LiNbO_3}$ crystal has to fulfill the quasi phase matching as described earlier. Varying the angle of observation allows us to fine-tune the phase-matched frequency ν_0 as it is determined by the poling period Λ to be

$$\nu_0 = \frac{c}{\Lambda |n^g_{\mathrm{IR}} - n_{\mathrm{THz}} \sin\Phi|}, \tag{3.1.12}$$

where c is the speed of light, n^g_{IR} the group velocity of the pump pulse, n_{THz} the refractive index at the generated frequency and Φ the angle of observation [Wei01]. By changing the angle of observation the freqency of the generated THz wave can be tuned. Due to the high refractive index of $\mathrm{LiNbO_3}$ in the THz range, the total internal reflection is around 11°and therefore the tuning is limited. The three main observation angles are $\Phi = 90°$, $\Phi = -90°$ and $\Phi = 0°$ so that the equation 3.1.12 can be simplified to

$$\nu_0(90°) = \frac{c}{\Lambda |n^g_{\mathrm{IR}} - n_{\mathrm{THz}}|} \tag{3.1.13}$$

$$\nu_0(-90°) = \frac{c}{\Lambda |n^g_{\mathrm{IR}} + n_{\mathrm{THz}}|} \tag{3.1.14}$$

$$\nu_0(0°) = \frac{c}{\Lambda\, n^g_{\mathrm{IR}}}. \tag{3.1.15}$$

The equ. 3.1.13 and equ. 3.1.14 are corresponding to the forward and backward propagating wave observed by *Lee et al.* [Lee00]. The equation 3.1.15 correspond to the THz wave emitted perpendicular to the driving source as described by *Weiss et al.* [Wei01]. These perpendicular emitted wave benefits from a shorter path length through the lithium niobate crystal and therefore the lower absorption. The bandwidth of the perpendicular emitted THz wave is highly dependent on the collection angle and the spatial distribution of the pump as already described in *Weiss et al.*[Wei01] and is limited by

$$\frac{\Delta\Omega}{\Omega} = \frac{C}{N}, \tag{3.1.16}$$

where C is a constant depending on the spatial distribution of the pump along the x-axis [Wei01].

In this thesis the focus is on the forward propagating THz wave collinear with the pump source. As this wave co-propagates with the optical pulse the forward propagating wave is far better detected as the backward propagating wave as observed by *Lee et al.*[Lee00] and also in our group [Car15]. Furthermore, if the pump source defines the generated frequency, the phase-matched frequency is defined by equation 3.1.13 to be generated in the most efficient way.

Due to the difference in the refractive index in the THz and the optical range a walk-off between the optical pulse and the generate THz will occur. Assuming a pulse duration τ_o

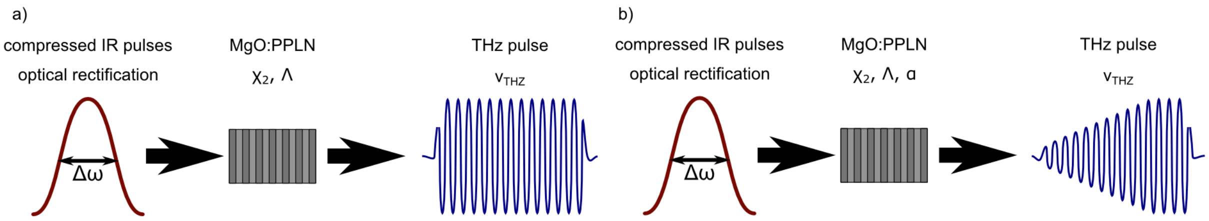

Figure 3.4.: Schematic concept of generating multi-cycle terahertz pulses via optical rectification. **a)** Compressed IR pulses with a bandwidth $\Delta\omega$ generates in the PPLN with nonlinear coefficient χ_2 and poling period Λ a rectangular THz pulse under ideal condition. **b)** The absorption α of the THz pulse introduces a loss leading to a damped THz pulse. The cycles generated in the first periods are absorbed.

of the optical pulse, the THz pulse will be τ_o behind the optical pulse after the walk-off length l_w described by

$$l_w = \frac{c\tau_o}{n_{\mathrm{IR}}^g - n_{\mathrm{THz}}}. \tag{3.1.17}$$

If the domain length is matched to the walk-off length between the optical and the THz pulse the generation of the THz radiation is most efficient [Lee00].

As shown by *Lee et al.*[Lee00] the envelope of waveform of an ideally generated THz pulse without any losses in the material itself is a rectangular pulse. Including a phenomenological loss in their simulations they were capable to match the simulations to their experimental waveform. The loss leads to a dumping of the first generated cycles and just the last generated cycles can exit the crystal without being absorbed. Figure 3.4 shows a schematic of a THz pulse generated via optical rectification for a PPLN without (a) and with (b) absorption.

3.1.3. THz conversion efficiency

The THz conversion efficiency depends on the input fluence and the generated THz fluence and is

$$\eta = \frac{F_{\mathrm{THz}}}{F_{pump}}. \tag{3.1.18}$$

Vodopyanov describes in detail how the efficiency is derived from the THz fluence and the pump fluence for a plain wave approximation [Vod06]. The efficiency is depending on the pump pulse format. In the case of optical rectification with compressed, broadband pump pulses the optical-to-THz conversion efficiency is

$$\eta = g_1 \frac{2\Omega^2 d_{eff}^2}{\epsilon_0 c^2 n_{\mathrm{THz}} n_{IR}^2 \Delta n} L F_{pump}, \tag{3.1.19}$$

where g_1 is a reduction factor depending on the $\tau \cdot \Omega$-product and d_{eff} is the effective nonlinear QPM coefficient. The reduction factor g_1 is for short pulses ($\tau < 1\,\mathrm{ps}$) ≈ 1 in the desired frequency range of 0.2 to 1 THz. The nonlinear coefficient is depending on the material and is for stoichiometric lithium niobate 152.4 pm/V [Vod08].

The efficiency for THz generation via optical rectification in PPLN therefore depends on the input fluence – and not the intensity – and the length of the crystal.

For long pulses the frequency components of a single pulse are not suited to generate THz via optical rectification. Therefore an interaction of two pulses is required. The generation process is DFG of the two pulses. The conversion efficiency can be written as [Agg77, Vod08]:

$$\eta_{\mathrm{THz}} = \frac{2\Omega^2 d_{eff}^2}{\epsilon c^3 n_{\mathrm{IR}}^2 n_{\mathrm{THz}}} L^2 I_{pump}. \tag{3.1.20}$$

The efficiency therefore depends on the intensity and the length squared.

As the underlying generation is based on DFG of two Gaussian pulses the generated pulse maintains the Gaussian shape. In the following, further theoretical aspects are discussed: cascading as increase of the efficiency, effective length, bandwidth of PPLN as well as the concepts introducing for high energy THz pulses.

3.1.4. Cascading and Manley-Rowe relation

The Manley-Rowe relation describes that the quantum-efficiency for a nonlinear energy conservation is limited to 1 and includes the energy conversation of the system [Man56]. As the frequency of the pump pulse is around 300 THz and the frequency of the THz pulse is around 0.3 THz, the efficiency of THz generation is limited to

$$\eta_{\mathrm{THz}} = \frac{\nu_{\mathrm{THz}}}{\nu_{\mathrm{pump}}} \sim 10^{-3}. \tag{3.1.21}$$

A higher conversion efficiency than Manley-Rowe relationship predicts is technical feasible due to cascading of the IR pulse [CG04]. The generated THz photons are back-acting

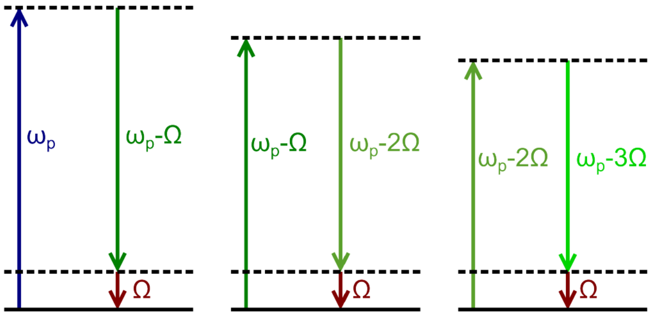

Figure 3.5.: Schematic of cascading while THz generation. The pump photon ω_p and the signal photon $\omega_p - \Omega$ generate a THz photon Ω. The signal photon and the THz photon generate a red-shifted photon $\omega_p - 2\Omega$ which is used to generate again a THz photon.

to the IR pulse and therefore introduce a redshift of the pump pulse (figure 3.5). This redshift is suited to predict the intrinsic conversion efficiency, which could be extracted at perfect out-coupling conditions as well as at lack of absorption of the generated THz pulse. To calculate the intrinsic efficiency η_i the center of mass of the input pump pulse and redshifted output pulse in the IR has to be determined. The intrinsic efficiency can be calculated by

$$\eta_i = \frac{\Delta\nu}{\nu}, \tag{3.1.22}$$

where $\Delta\nu$ is the frequency difference between the two centers of mass and ν is the frequency of the IR input pulse.

The cascading circumvents the Manley-Rowe relation and allows us to generate even higher conversion efficiencies. Using the cascading effects efficiencies up to 10% may be achieved as predicted by *Ravi et al.* [Rav16b].

3.1.5. Effective length

The efficiency of THz generation is proportional to the length (L) of the crystal [Vod06]. As lithium niobate has a high absorption coefficient in the THz range efficiency is impaired and absorption needs to be considered in the calculation of the effective length L_{eff}. The THz conversion efficiency (η_{THz}) is thus proportional to the effective length L_{eff}:

$$\eta_{\mathrm{THz}}(L) \propto \frac{1}{\alpha}\left[1 - \exp\left(-\alpha L\right)\right] \equiv L_{eff}, \tag{3.1.23}$$

where α is the absorption coefficient. The effective length is for long crystals inverse to the absorption coefficient:

$$L_{eff} = \frac{1}{\alpha}. \tag{3.1.24}$$

The effective length of $LiNbO_3$ is at room temperature $L_{eff} = 1.9\,\mathrm{mm}$ assuming an absorption coefficient of $\alpha = 5.2\,\mathrm{cm}^{-1}$. As the absorption coefficient of $LiNbO_3$ is reduced with temperature the effective length increases for a cryogenic cooled crystal compared to a crystal at room-temperature. At cryogenic temperature the absorption coefficient is reduced to $\alpha = 2.8\,\mathrm{cm}^{-1}$ resulting in an effective length of $L_{eff} = 3.6\,\mathrm{mm}$.

The effective length limits the amount of the generated THz but it can be still beneficial to have longer crystals than the effective length as the frequency content may build up in the crystal for example in a THz optical parametric amplifier [Cir17].

3.1.6. Acceptance bandwidth of a PPLN

The acceptance bandwidth of the PPLN can be derived via differentiating the wave-vector mismatch as well as the condition for the acceptance bandwidth of the wave-vector itself $\Delta k^{acc.} L/2 = \pi$ [Vod06]. The acceptance bandwidth is therefore

$$\Delta\Omega^{acc} = \frac{d\Delta k}{d\Omega}\Delta k^{acc} = \frac{c}{\Delta n}\frac{2\pi}{L}. \tag{3.1.25}$$

As the angular frequency is defined as

$$\Omega = \frac{2\pi c}{\Delta n \Lambda}, \tag{3.1.26}$$

the acceptance bandwidth can be described by

$$\Delta\Omega^{acc} = \frac{\Omega}{N}, \tag{3.1.27}$$

where $N = L/\Lambda$ is the number of poling periods in the PPLN. The bandwidth can be rewritten in terms of frequency as

$$\Delta\nu = \frac{\nu}{N}. \tag{3.1.28}$$

Therefore, when increasing the length of the PPLN the spectral width of the generated THz pulse will narrow down.

3.1.7. Generation of high energy, multi-cycle terahertz pulses

The energy of the THz pulses generated via optical rectification is limited by the crystal size in combination with the damage threshold of the crystal. High energy pulses in the mJ-level are essential for efficient electron acceleration [Won13]. To cope with this challenge *Ravi et al.* [Rav16b] proposed three pump mechanism to be used instead of optical rectification of a compressed pulse to reach the high energy pulses:

1. pulse sequence of compressed pulses with an optical bandwidth adapted to optical rectification,
2. difference frequency of two narrow lines with a spectral difference of the desired frequency,
3. two broadband chirped and delayed pulses generate a sequence of pulses as they interfere with each other.

In this thesis the experiments for the pulse sequence of compressed pulses and the chirp-and-delay pumping scheme and the thereby resulting improvements are further discussed.

Pulse sequence of compressed pulses

Using a sequence of compressed pulses allows to distribute a predefined pump energy over several pulses. As the efficiency for OR is depending on the pump fluence, the efficiency remains unchanged when the pump fluence is spread over a sequence of pulses. Reducing the peak intensity of each single pulse allows to increase the total pump fluence. This traces back to the observation, that the damage threshold of the crystal is depending only on the peak intensity at a short pulse duration[Boy03]. As consequence the efficiency can be increased due to the higher total pump fluence. An additional efficiency increase occurs as the generated THz pulses add coherently. The details of this process as well as the executed measurements are described in Chapter 4.

Chirp-and-delay pumping

The concept of chirp-and-delay pumping aims to generate high energy pulses. Reaching a higher pump energy is achieved by pumping with a pulse with a long pulse duration which

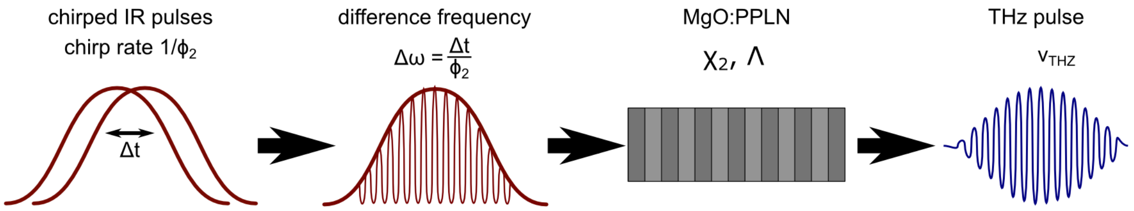

Figure 3.6.: Schematic concept of generating multicycle terahertz pulses with two chirped and delayed pulses.

increases the damage threshold. In the chirp-and-delay concept a broadband, chirped pulse is split in two equally loaded pulses delayed by a time delay Δt (figure 3.6). The chirp rate ϕ_2 in combination with the time delay of the pulses generates the necessary frequency content via

$$\Delta\omega = \frac{\Delta t}{\phi_2}. \tag{3.1.29}$$

Matching the poling period Λ of the PPLN with a nonlinear second order coefficient χ_2 allows an efficient THz generation reaching also the goal of high energy THz pulses. The process and the conducted experiments are described in detail in Chapter 5.

3.2. Properties of the THz beam and the THz pulse

Fundamental transverse mode (TEM00) laser beams are Gaussian modes, whose propagation has been described theoretically by *Boyd and Gordon* in the early 60's [Boy61]. This section summarizes this formalism with the equations which are valid for all optical frequencies and an analysis for the narrowband THz waves with Gaussian spatial profile.

3.2.1. Gaussian beam propagation

The THz waves as the name already says are classically described by their frequency ν. For the treatment of the propagation of the beam, it is commonly preferred to use the wavelength connected to the frequency by

$$\lambda = \frac{c}{\nu}. \tag{3.2.1}$$

The spot size parameter $w(z)$ after a propagation z is calculated via

$$w(z) = w_0\sqrt{1+\frac{z^2}{z_R^2}} \tag{3.2.2}$$

and depends on the beam waist w_0 and the Rayleigh range z_R defined by

$$z_R = \frac{\pi w_0^2}{\lambda}. \tag{3.2.3}$$

At the Rayleigh distance z_R the spot size is $\sqrt{2}$ times greater than the beam waist. The Rayleigh distance defines the distance where the beam is collimated. The divergence of a beam is described with the divergence angle θ calculated via

$$\theta = \frac{\lambda}{\pi w_0}. \tag{3.2.4}$$

As the Gaussian beam propagation assumes the paraxial approximation, the divergence is limited to an angle of 30°[Sie86]. This sets the diffraction limited spot size of a wave to

$$w_{min} = \frac{2\lambda}{\pi}. \tag{3.2.5}$$

The diffraction limited spot size limits the focusability of the THz beam.

Considering a THz beam with a Gaussian beam profile, a diffraction limited minimal achievable waist is in the range of millimeters. The clear aperture of the crystals used for

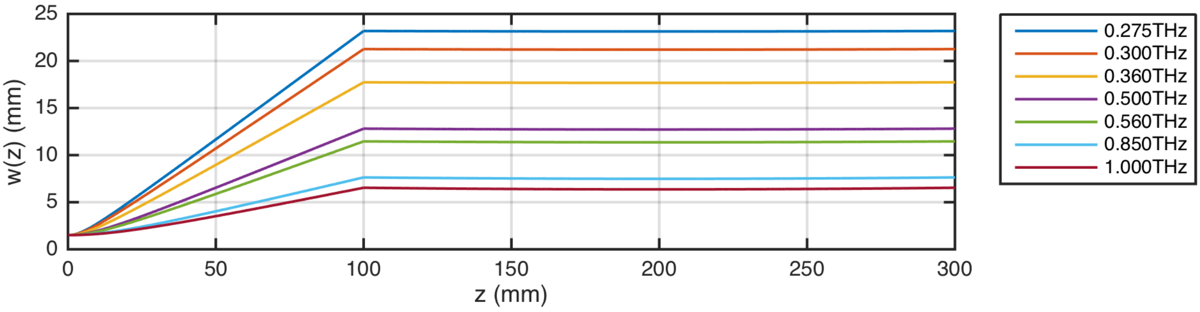

Figure 3.7.: Gaussian beam propagation of a THz beam with beam size of $w_o = 1.5\,\mathrm{mm}$ for various frequencies. At a distance $z = 100\,\mathrm{mm}$ a lens is placed to illustrate the collimation of the beam.

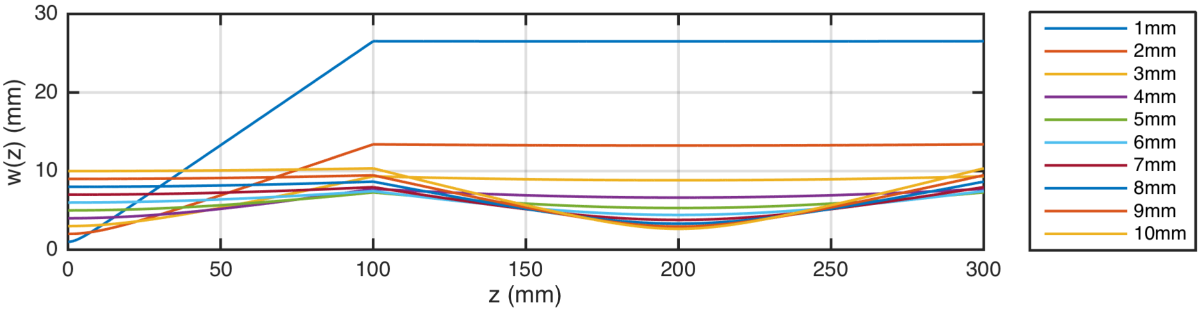

Figure 3.8.: Gaussian beam propagation of a THz beam with a frequency of 0.36 GHz for various beam sizes w_o. At a distance $z = 100\,\mathrm{mm}$ a lens is placed to illustrate the divergence of the beam.

THz generation are in this range of millimeters. For example, a THz beam with 1.5 mm waist diverges with a divergence angle up to 13.4° for 0.275 THz pulses and 3.6° for 1 THz (see figure 3.7). Lower frequency beams are diverging even faster and exceed the limit of a divergence of 30°.

For example, a lens placed at a distance of 100 mm is able to collimate THz beams which are used in this thesis (figure 3.7) for at least a distance of 30 cm.

Increasing the initial beam waist decreases the divergence as seen in figure 3.8 for a THz beam with a frequency of 0.36 THz. A beam with a waist of $w_0 = 5\,\mathrm{mm}$ has a divergence of 3°, 5°divergence corresponds to a beam waist of $w_0 = 2.98\,\mathrm{mm}$.

The THz beam is still slightly diverging for a beam waist of 10 mm. In the infrared range a beam is called collimated if the Rayleigh range is greater than a meter. A THz beam with a frequency of 0.36 THz can be regarded as collimated if the beam has a waist of 26.5 mm. This has to be considered if the THz beam will be transported to subsequent applications like for example electron acceleration.

Measurements in the workload of this thesis confirmed the Gaussian beam propagation for the THz waves (see section 5.4.5). The narrow bandwidth of the THz pulses used in the experiments helps to describe the optical beam path as no spatial distribution of the different frequencies occurs.

3.2.2. Pulse peak field

The THz pulse is characterized by the energy, the pulse duration and the beam size. For most experiments the key parameter is the peak field. It combines all characteristic parameters for the multi-cycle terahertz pulses. Independent of a direct measurement through the electro optic sampling (EOS) the peak field E can be calculated with the intensity I

$$E = \sqrt{\frac{2I}{c\epsilon_0}} \qquad \text{with} \quad I = \frac{E_p}{A\tau} \tag{3.2.6}$$

where c is the speed of light, $\epsilon_0 = 8.85 \cdot 10^{-12}$As/Vm is the vacuum permittivity, E_p is the peak energy, A the spot size of the THz pulse and τ the pulse duration. Assuming a diffraction limited spot size of

$$w_0 = \frac{\lambda}{\pi \mathrm{NA}} = \frac{\lambda}{\pi n \sin\theta} = \frac{2\lambda}{\pi}, \tag{3.2.7}$$

where NA= $n\sin\theta = 0.5$ is the maximal numerical aperture limited by the Gaussian beam model which collapses for an opening angle $\theta > 30°$, the area A can be calculated with

$$A = \pi w_0^2 = \frac{4\lambda^2}{\pi}. \tag{3.2.8}$$

Table 3.1 shows for various frequencies the diffraction limited spot size and the corresponding area A, and also the peak field within the example of 100 µJ pulse energy and 300 ps pulse duration.

In figure 3.9 the diffraction limited spot size is plotted versus the THz frequency. The spot size is inversely proportional to the frequency and therefore increase steeply in the frequency range under 1 THz. In consequence a Gaussian THz beam diverges much faster

ν [THz]	λ[µm]	w_o [mm]	A [mm^2]	E_p [µJ]	τ [ps]	I [GW/m^2]	E [MV/m]
0.30	999	0.636	1.271	100	300	262	14.05
0.36	832	0.530	0.883	100	300	377	16.87
0.50	599	0.382	0.458	100	300	728	23.43
0.56	535	0.341	0.365	100	300	913	26.24
0.85	352	0.224	0.158	100	300	2104	39.83

Table 3.1.: Diffraction limited spot size for an opening angle of 30°for the frequencies used in this thesis. Calculated peak electric field E for a THz pulse with 100 µJ pulse energy and 300 ps pulse duration.

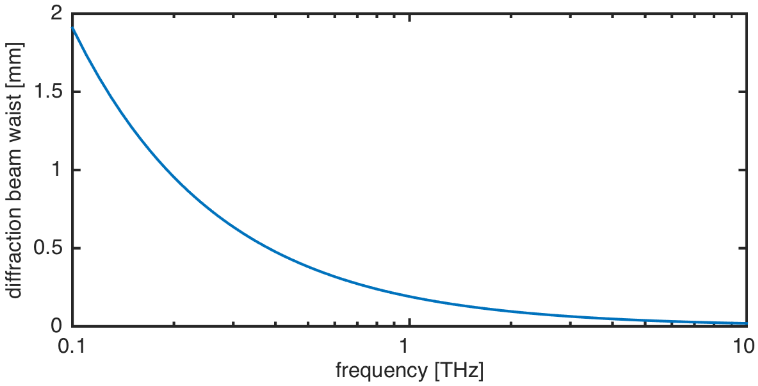

Figure 3.9.: Diffraction limited beam size w_o versus the THz frequency ν calculated via $w_0 = \frac{2c}{\pi\nu}$.

than higher frequency beams. For example an optical beam at a wavelength of 800 nm can be focused to a beam waist of $w_0 = 0.5$ µm. THz beams can not be focused as tightly as the optical beams as discussed in section 3.2.1.

The calculated electric field strengths for several input energies are depicted in figure 3.10. First measurements of acceleration were performed with THz fields around 30-40 MV/m [Nan15]. Efficient acceleration with THz pulses could be achieved with field strengths in the range of 100-500 MV/m, but would be more efficient in the range of 1 GV/m [Won13]. To reach this range of efficient acceleration, multi-cycle THz pulse energies in the mJ-range are necessary for the THz pulse lengths in the range of $100 - 1000$ ps.

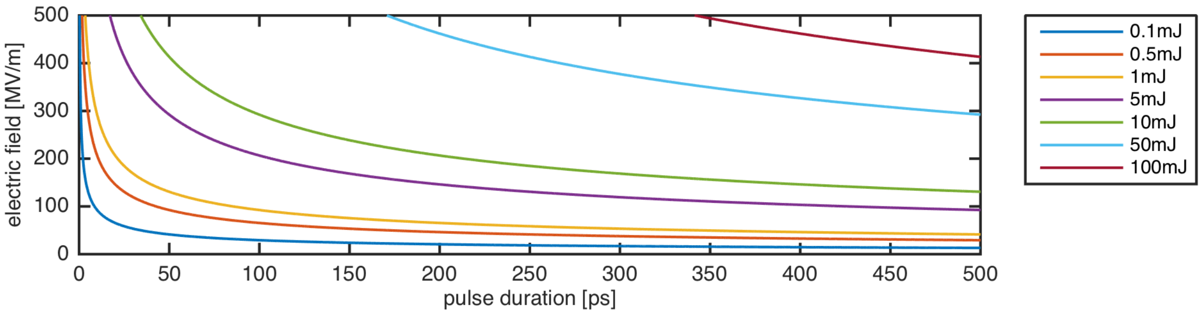

Figure 3.10.: The electric field strength of a multi-cycle THz pulse with a frequency of 0.36 THz at several pulse energies.

3.3. Experimental resources

At the Center for Free Electron Science several high energy lasers are well developed sources to generate multi-cycle THz pulses. The possible wavelengths ranges for high energy pulses in the mJ-range are 0.8 µm, 1 µm and at 2 µm. The most developed sources are Ti:sapphire based high energy laser with a center frequency around 0.8 µm reaching energies above 1 J. To generate multi-cycle THz pulses these high energy laser pulses as well as an optical crystal – the periodically poled lithium niobate – are essential. This chapter pays attention to the special experimental resources: the periodically poled lithium niobate crystals as well as the laser sources to conduct the experiments of this thesis.

3.3.1. Periodically poled lithium niobate crystals

Based on the work of *Carbajo et al.* multi-cycle THz pulses can already be generated with energies up to 1 µJ [Car15]. This thesis focuses on a further optimization of the THz pulse energy by optimizing the frequency content or temporal content of the pump laser. As gain material magnesium oxide doped periodically poled lithium niobate (MgO:PPLN) crystals with a doping concentration of 5 mol%, which has been proven to mitigate the photo-refractive damage and increase the life-time [Mil98], are used. To phase-match the desired frequency the crystals are poled by inverting the ferroelectric domains after the walk-off length l_w (section 3.1.1). In that case the poling period Λ defines the phase-matched frequency ν via

$$\nu = \frac{c}{\Lambda|n(\nu) - n_{\mathrm{g}}|} \tag{3.3.1}$$

where $n(\nu)$ is the refractive index of the generated signal and n_{g} the group velocity index at the pump wavelength [Fej92, Yam93] (see section 3.1.1). As the refractive indices for the lithium niobate are known both at 300 K and 100 K with $n(300K) = 5.05$ and $n = (100K) = 4.8$ (see section 2.2.1) the generated frequency can be calculated with the group velocity index $n_{\mathrm{g}} = 2.26$ at the pump wavelength of 800 nm [Zel97] (table 3.2). The table 3.2 summarizes all PPLN used in the experiments with the corresponding clear aperture (heigth (H) x width (W)) and length (T).

Crystal number	HxW(mm^2)	T (mm)	Λ (µm)	ν @ 300K	ν @ 100K
1	3x10	10	125	875	944
2	3x10	5	212	516	557
3	3x10	10			
4	4x4	20			
5	10x15	36	330	332	358
6	3x10	10	400	274	295

Table 3.2.: Generated frequency calculated via 5.1.2 at the different temperatures for the poling period of the used PPLN

One of the PPLNs used to generate efficiently multi-cycle THz had a poling period of 212 µm and a clear aperture of 3x3mm^2. Figure 3.11 a) shows a light microscope picture of this PPLN to check the thickness of the domains. A mask is glued to the crystal during the production of the domain walls [Mil98]. The structure of the mask is still visible after removing the mask and corresponds to the domain wall of the PPLN. This allows to double-check the poling period and the homogeneity of the poling.

The aperture size of the PPLN limits the generation of high energy multi-cycle THz pulses due to the damage threshold of lithium niobate. Commercially PPLN are available up to a height of 4 mm. Due to the crystal structure and the manufacturing process the size of the width, the length and the height are interrelated. The width is depending on the length of the crystal: for crystals up to 10 mm a width of up to 10 mm is possible, for longer crystals the width is depending on the height of the crystal so that the clear aperture is up to 4x4 mm^2. The crystals are made of 5 mol% magnesium-doped congruent z-cut lithium niobate wafers and poled with the period as shown in table 3.2.

Within a collaboration with the group of Professor Takunori Taira (Laser Research Center, Institute for Molecular Science, Japan) a PPLN with a larger clear aperture than commercially available was received for our high energy experiments [Ish12]. A picture of this crystal is shown in figure 3.11 b). The crystal itself has a dimension of 10Hx20Wx36L mm^3 where the QPM area is just 10x15 mm^2. The poling period of this crystal is 330 µm, which corresponds to a frequency of 360 GHz.

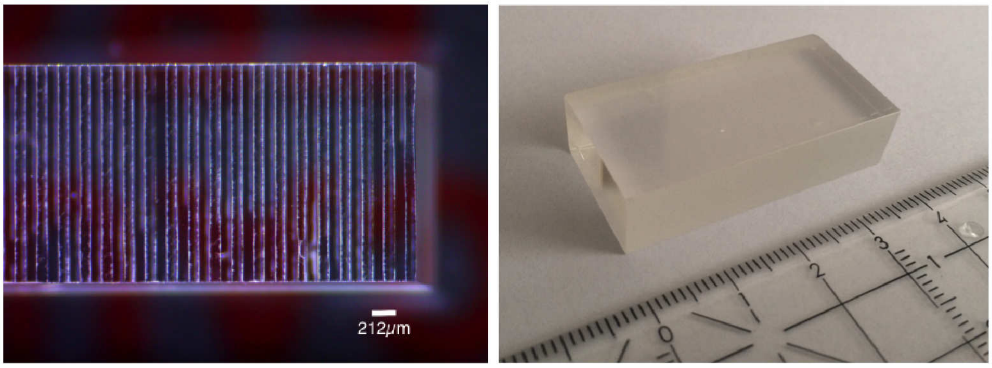

(a) (b)

Figure 3.11.: **a)** Microscope picture of a PPLN with a poling period of 212 µm, **b)** picture of the PPLN from Prof. Taira with a length of 36 mm.

Damage threshold

Optical induced damage of the crystal structure and the caused loss of transmission is one limitation at higher pump energies. Already in the early years *Askin et al.* found that the lithium niobate crystal showed inhomogeneities of the refractive index after optical pumping [Ash66]. For frequency conversions in the IR and MIR the lithium niobate crystal is normally heated to allow the remigration of the electrons and thus to reduce the optically induced damage [Ram00]. This subsection gives a brief overview about the measured optically induced damage thresholds for a lithium niobate wafer at laser sources used for this thesis.

The aim is to determine the critical pump power where damage occurs. This pump power is measured on a magnesium oxide doped lithium niobate wafer (0.5 mm thick, x-cut, 5 mol% MgO:LiNbO$_3$) at room temperature. The wafer is representative for the actual PPLN crystals and has the advantages that it is much cheaper then the PPLN crystals.

At a 5 Hz repetition rate Ti:sapphire based laser system the wafer damages at a fluence of 750 mJ/cm^2. For shorter pulses the damage threshold fluence decreases with $\sqrt{\tau}$ [Boy03]. The damage threshold measured for 150 fs long pulses at a 1 kHz repetition rate Ti:sapp system is 80 mJ/cm^2. To circumvent the optically induced damage on the actual crystal the pump laser is operating at a safe operation points

1. 294 K, 800 nm pump, 240 ps, 5 Hz: 650 mJ/cm^2,

2. 80 K, 800 nm pump, 240 ps, 5 Hz: 600 mJ/cm^2,

3. 295 K, 800 nm pump, 150 fs, 1 kHz: 75 mJ/cm^2.

When going to cryogenic temperature, the electrons are less mobile leading to a lower damage threshold especially at the domain walls of the PPLN which has to be considered.

Our hypotheses that bulk damage occurs due to the missing anti-reflection (AR) coating on the crystals briefly before the back surface was not further investigated. We suggest that the electric field of the actual and the reflected beam are overlapping leading to a higher peak field at the end of the crystal/wafer.

The dependence of the damage threshold on low temperatures, on repetition rate and on the wavelength is not fully understood and needs further investigation. Other groups focus on this research topic as for example the investigation of repetion rate scaling by *Bach et al.* [Bac17].

3.3.2. Laser systems

As THz generation is a nonlinear process, pump lasers with high pulse intensities are necessary. In the experiments of this thesis two Ti:sapphire based laser systems are used to generate the multi-cycle THz pulses. Ti:sapphire based laser systems are highly developed systems generating ultrashort IR pulses typically centered at a wavelength around $\lambda = 800$ nm. Compared to other gain materials like Ytterbium doped materials, Titanium Sapphire has a broad bandwidth allowing ultra short pulses in the fs-regime. This subsection describes the two used pump lasers, the "Legend Elite Cryo PA" and ANGUS.

Cryogenically cooled CPA with a 1 kHz repetition rate

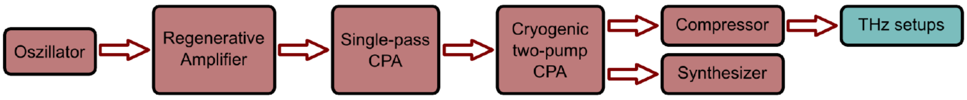

Figure 3.12.: Schematic of the "Legend Elite Cryo PA" laser system of Coherent, Inc. used for THz experiments.

The laser named "Legend Elite Cryo PA" is commercially available from Coherent, Inc. It is a cryogenically cooled chirped pulse amplifier (CPA) laser system producing broad bandwidth, high energy pulses. In figure 3.12 a schematic overview of the system is drawn with all stages of the system. The system is seeded by the "Vitara" oscillator producing low power femtosecond pulses with MHz-repetition rate. The pulses are then amplified in the "Legend Elite Duo", a regenerative amplifier combined with a single pass CPA, that bring the pulse energy to the mJ-level and reduces the repetition rate to $f_{rep} = 1\,\mathrm{kHz}$. Hereby the transform limited pulse duration is still 145 fs to reach the optimal bandwidth but is stretched to $\sim 150\,\mathrm{ps}$ to seed the last amplification stage. In the last amplification stage the Ti:sapp crystal is cryogenically cooled to increase the possible output power due to a better heat transfer in the crystal. The crystal is pumped from two sides to achieve a good beam profile. The pulses are amplified to 22 W by a single pass through the crystal. The cryogenically cooled CPA produces thus laser pulses with an energy of $E = 22\,\mathrm{mJ}$ at a repetition rate of 1 kHz. The center wavelength of the laser is at $\lambda = 805\,\mathrm{nm}$ with a bandwidth of 10 nm. In an external laser compressor these pulses are compressed to a pulse duration of 145 fs.

This system is used in our laboratory to seed a synthesizer producing ultra-short pulses from the ultra violet (UV) to the MIR. The pump for the last stage of the synthesizer with an energy of $E = 8\,\mathrm{mJ}$ is used for the THz experiments. The external compressor is close to the THz setups to allow a good beam quality at the experiments.

The broad bandwidth of this CPA laser system is used to generate THz pulses via optical rectification. For this thesis the laser is used to generate narrowband THz pulse with a train of compressed pulses (section 4).

ANGUS system

The ANGUS laser system is an improved version of the commercially available chirp pulse amplfication (CPA) system ALPHA 5/XS 200 TW from THALES LASERS [Mai17]. The system is based on Ti:sapp technology and produces broad bandwidth, high energy pulses. The reliability and accessibility of the CPA was significantly improved by adding several diagnostics, active pointing stabilization, and integrating it into a control system.

A schematic of the ANGUS laser system is shown in figure 3.13. A Venteon oscillator with above 100 nm bandwidth and below 15 fs pulse duration at a repetition rate of

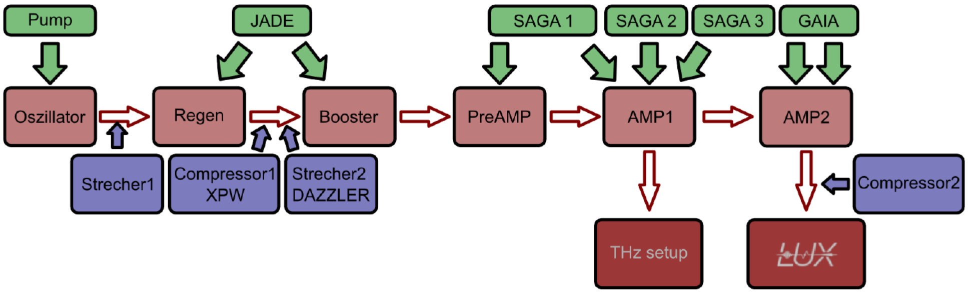

Figure 3.13.: Schematic of the Angus laser system. **Color key:** light red: amplification stages; red: experiments; green: pump lasers; blue: temporal influence.

83 MHz seeds the laser system. Furthermore, the time base for the remaining amplification is set by the oscillator. The first amplification occurs in a regenerative amplifier to roughly 500 uJ after stretching the seed via an Öffner-stretcher (Strecher 1). The regenerative amplifier (Regen) is pumped with a portion of the first high energy pump laser Jade – 25 W at 1 kHz and a center wavelength of 527 nm – and generates pulses at a repetition rate of 1 kHz. The temporal contrast of the pulses is increased in the so-called cross-polarized-wave generation (XPW) stage. There the pulses are compressed in a grating compressor (Compressor 1) and transmitted through a combination of a nonlinear crystal and a polarizer, which cleans the intense central pulse.

Before entering the next amplification stage (Booster) the pulse is again stretched by an Öffner-stretcher – identical but larger than the first stretcher – setting mainly the temporal properties of the laser as 2.3ps^2 for the group delay dispersion (GDD) and -0.0044 ps^3 for the third order dispersion (TOD). The Booster, pumped by the Jade pump laser, amplifies the stretched pulses to an energy of about 100 µJ. A Pockels cell after the Booster reduces the repetition rate to 5 Hz to allow further amplification.

The next two amplification stages (PreAMP and AMP1) are multi-pass amplifiers with 5 and 3 passes amplifying the pulses up to an energy of 30 mJ and 1.2 J, respectively. The stages are pumped by three 1.6 J pump lasers – so called Saga 1, Saga 2 and Saga 3 – where the PreAMP is just using 10% of Saga 1. The uncompressed pulses out of AMP1 are used for the chirp-and-delay experiments. The stretched pulse duration is 240 ± 20 ps. The output energy of the AMP1 can be tuned by decreasing the energy of pump lasers. With just Saga 1 the energy is 70 mJ and Saga 1 and Saga 2 generate 320 mJ. The tunablility is useful for the THz experiments to minimize the risk of damaging optics due to unused laser energy.

The final stage (AMP2) is again a 3 pass amplifier with an output energy greater than 6 J pumped by Gaia, a frequency doubled Nd:YAG laser with an energy of 14 J at 5 Hz. The 40 nm broad pulses (full-width half maximum (FWHM)) are compressed in a large in-vacuum grating compressor (Compressor 2) to below 30 fs for the laser-plasma experiments. The system is optimized for the laser-plasma acceleration and has therefore the possibility to optimize the spatial wavefront as well as the temporal shape (DAZZLER). The system control is well engineered to achieve a reliable source for plasma-wake-field acceleration with a high temporal contrast and a good focusability.

The Angus laser system is a high energy laser with up to 1.2 J for THz experiments and controlled output parameters. For this thesis the laser is used to generate high energy THz pulses via chirp-and-delay pumping (section 5).

3.4. Previous experiments on multi-cycle THz generation with compressed femtosecond pump pulses

This section summarizes the results of *Carbajo et al.* [Car15] which are relevant for the measurements of this thesis. By generating narrowband THz pulses via optical rectification, *Carbajo* achieved a record efficiency of 0.12%. The efficiency was increased with two major steps: first of all, the crystal was cryogenically cooled to reduce the absorption of the generated THz pulse and secondly the bandwidth of the pump laser was optimized to generate an efficient but not too large bandwidth to avoid dephasing effects or an energy transfer into odd harmonics [Car15]. Cryogenic cooling of the crystal allowed a fivefold efficiency increase due to the lower terahertz absorption at the generated frequency of around 0.5 THz. The authors also verified that for optical rectification a forward and backward propagating wave was generated (as described in section 3.1.2). In figure 3.14 (left) the EOS trace of the two waves is depicted. Hereby a bandpass filter was used to select the frequencies higher (forward) or lower (backward) then 0.375 THz. The forward propagating wave was the more dominant wave. By Fourier-transforming this wave via a FFT into the frequency range the spectral amplitude of the generated THz wave could be resolved (figure 3.14 (right)). The frequency of the three crystals with a poling period of $\Lambda = 400\,, 212$ and $125\,\mu$m, which are used in this thesis, were measured. The peak frequency of these PPLNs were $\nu_0 = 0.276$, 0.513 and 0.876 THz. The bandwidth for the 10 mm long PPLN with a poling period of $\Lambda = 212\,\mu$m was measured to be 19.8 GHz at room temperature and 18 GHz at 77 K. This bandwidth $\Delta\nu$ was two times larger than the lower bound of the acceptance bandwidth $\Delta\nu$ calculated via

$$\Delta\nu = \frac{\nu}{N}, \tag{3.4.1}$$

where ν is the THz frequency and N the number of periods in the PPLN. The absorption reduces the effective length and therefore the bandwidth as also explained in section 3.1.6.

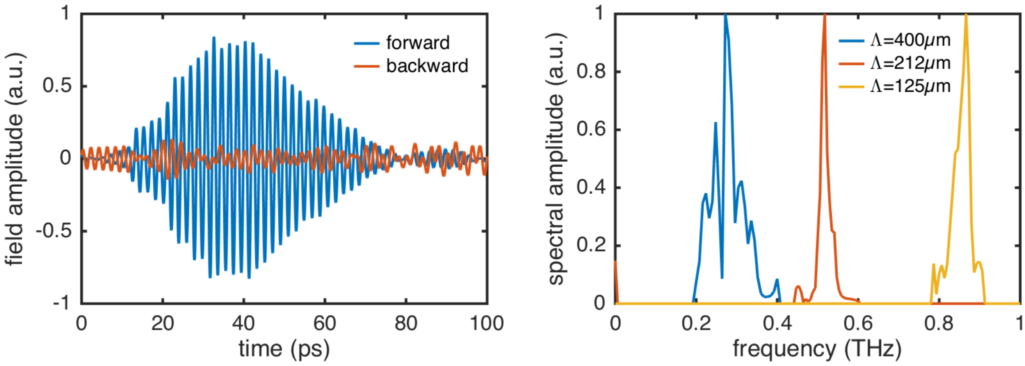

Figure 3.14.: Left: Processed EOS trace for the forward propagating wave (blue, $\nu > 0.375\,\mathrm{THz}$) and the backward propagating wave (red, , $\nu \leq 0.375\,\mathrm{THz}$) in a 5 mm long PPLN with a poling period of $\Lambda = 212\,\mu\mathrm{m}$ at room temperature. **Right:** Spectral amplitude of 10 mm-long crystals with a poling period of $\Lambda = 400,\ 212$ and $125\,\mu\mathrm{m}$ and the corresponding frequencies $\nu_0 = 0.276,\ 0.513$ and $0.876\,\mathrm{THz}$.(data from [Car15])

3.5. Measurement tools

The setup of the multi-cycle THz generation is composed of several technical tools. This section focuses on experimental equipments which are mandatory for all pump sources. They cover the different purposes to measure for example the THz energy or the THz frequency content or to cool down the crystal in the first place. Also the detection setups designed to measure either the THz energy or the frequency content, if possible, are described.

The characteristic parameters like optical input fluence (F), crystal temperature (T), crystal length (L) and domain period (Λ) will not be detailled here but together with the individual measurements.

3.5.1. Experimental setup for cryogenic cooling

The crystal length is one of the crucial parameters determining the efficiency of the THz generation. As described in section 3.1.5 this length is not the actual length but the effective length reduced by the absorption coefficient

$$L_{eff} = \frac{1}{\alpha}\left[1 - \exp\left(-\alpha L\right)\right]. \tag{3.5.1}$$

This corrected length is named effective length of the crystal. As the absorption of the generated THz pulse is depending on temperature of the optical crystal the effective length is temperature dependant. While at room temperature the effective crystal length is limited to a few millimeters ($\approx 1.4\,\mathrm{mm}$), the effective crystal length increases to around 5 mm at cryogenic cooling to liquid nitrogen (LN_2) temperature. Therefore the cryogenic temperature allows to use even longer crystals and reduces the loss of the THz cycles which are generated at the entrance of the crystal.

For the cryogenic cooling a commercially available Liquid Nitrogen Detector Dewar from CRYO Industries is completed with a home-made cryo-chamber. Figure 3.15 shows on the left side the cryo-chamber with the output window, normally an AR-coated fused silica window. Inside the chamber the copper cryo-tail is mounted to the cryo-dewar united with a 250 µm indium foil to compensate for irregularities. The cryo-tail is isolated from the chamber to avoid a heat transfer by a small gap between the cryo-tail and the cryo-chamber of 5 mm. On the cryo-tail the PPLN crystal is mounted with an

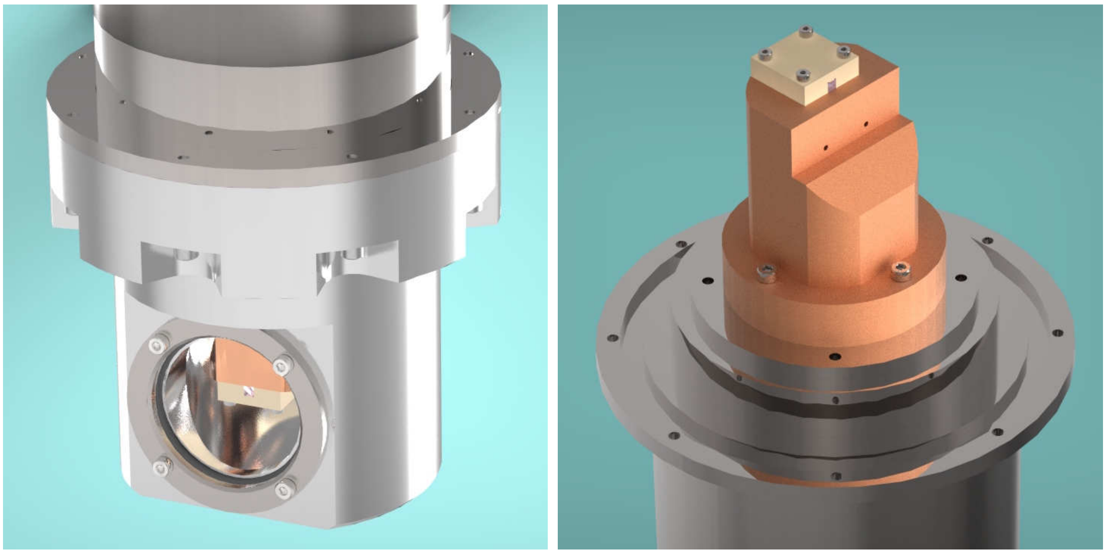

Figure 3.15.: Left: Vacuum chamber for cryogenic cooling of the PPLN. **Right:** Cold finger of a 2 cm long PPLN.

Polyetheretherketon (PEEK) holder as depicted in figure 3.15 (right). The position of the crystal is chosen in such a way that the output surface of the crystal is as close as possible to the output window to be capable to collect as much as possible from the generated THz pulse. This condition could be achieved by an asymmetric cryo-tail. The cryo-finger offers the possibility to mount an aperture made of macor-ceramic at the front surface to be capable to overfill the PPLN with the pump pulse. The distance between the aperture and the crystal is ~5 mm. Due to the asymmetry of the cryo-tail we need to build for each crystal length a specific cryo-tail.

The crystal is mounted onto the cryo-tail with an indium foil of 250 µm to have a good thermal contact between the cooper and the lithium niobate. The indium layer is able to buffer the temperature forces and thus prevents cracking of the crystal. The ceramic aperture should be always installed to prevent the PPLN to be coated either with indium or with PEEK.

The cryo-chamber has on both sides of the PPLN an AR-coated window for the pump wavelength. If the pump energy is low enough, the output window can be exchanged to a TPX window. For the high power operation, TPX can not be used due to the damage threshold of the TPX. Using the fused silica (FS) window as output window, the losses at the fused silica window have been determined as 20% (see chapter 2.2.2).

With this setup the crystal can be cooled to liquid nitrogen temperature and is mounted to collect as much as possible of the generated THz pulses.

3.5.2. THz collection and energy measurement

Once the THz pulses have been generated in the PPLN crystal they need to be collected. Due to the relative small spot size compared to the wavelength of the THz beam, the crystal can be assumed as a focus of the THz beam. As a first step in the collection process the THz beam is collimated with either a parabolic mirror or a TPX lens and then focused onto a pyro detector. If a parabolic mirror with a hole is used as the collimation optic, this mirror can be also used to separate the IR pump from the THz beam allowing to analyze the optical spectra at the same time.

A schematic drawing of one detection setup is shown in figure 3.16. When the beam is larger than the hole in the off-axis parabola (OAP), normally 3 mm diameter, a Teflon plate with a low effect on the THz pulse (see section 2.1.1) is used to block the spectral IR components. The two OAP are aligned as 4f-imaging setup. This allows to focus down the beam to the size of the original beam.

The energy of the THz pulse can be measured with a pyroelectric detector. In this thesis three different pyroelectric detectors are used:

- the Gentec-EO Model THZ9B-BL-BNC as the most sensitive detector,
- the Ophir Spiricon Model 3A-P-THz as a well calibrated power detector and
- the Gentec-EO Model SDX-1152 as a fast detector, which can resolve pulses up to a repetition rate of 1 kHz.

Drawback of the THZ9B is the slow response time of 11.2 ms. This detector is specified to be chopped with 5-25 Hz and is normally used for high repetition rate operation due to the averaging usage. In the interest of using this detector at a laser with a repetition rate of just 5 Hz, *Spencer W. Jolly* determined the detector response for a single THz pulse with a repetition rate of just 5 Hz. The detector operates still in single pulse operation at low repetition rates, but has a 90% lower voltage response compared to the specified 1 kHz, chopped response. The detector voltage response of the THZ9B is 0.96 nJ/mV at a 5 Hz system and 0.09 nJ/mV at a 1 kHz system chopped at 20 Hz. The detector is

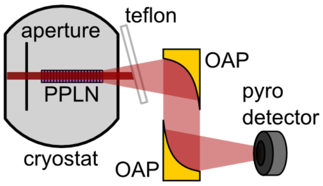

Figure 3.16: Schematic of the collection and energy-measurement setup. The off-axis parabola (OAP) is collimating the THz beam and focus it on the pyroelectric detector.

protected with a piece of PE to prevent the detector from scattered or direct pump light and its second harmonic. Due to the absorption of THz energy in PE (see section 2.2.2), the detector has a voltage response of 1.61 nJ/mV at the repetition rate of 5 Hz and of 0.1515 nJ/mV at a repetition rate of 1 kHz chopped at 20 Hz.

The Ophir detector measure the THz power directly. The protective PE piece has to be considered and calibrated at the THz source directly. Drawback of this detector is the necessary high repetition rate (15 µW - 3W) or energy (20 µJ - 2 J) to be capable to detect the THz pulses.

The Gentec SDX-1152 has a calibration factor of 6 nJ/mV and with the protective PE piece around 10 nJ/mV if the losses at the PE piece are assumed to be 60%.

All used detectors are cross-calibrated to the Ophir power meter at exactly that point where the power meter was calibrated. Therefore all presented results are cross-calibrated energy measurements.

All measured THz energies presented in this thesis are an average of at least 10 pulses to minimize statistical errors on the measured THz pulses.

3.5.3. THz energy and efficiency calculation

To compare different setups is quite difficult as the THz pulse energy of a setup is not uniquely defined. A better descriptor to compare different setups to each other is the conversion efficiency

$$\eta = \frac{E_{\mathrm{THz}}}{E_{pump}}, \tag{3.5.2}$$

the relation of the THz and pump energy. For an even more precise comparison, the losses at different parts of the generation process need to be taken into account to distinguish between the engineering factors and the actual performance of the setup. In figure 3.17 a representation is outlined to explain the calculation of the THz energy and the conversion efficiency in the following paragraph.

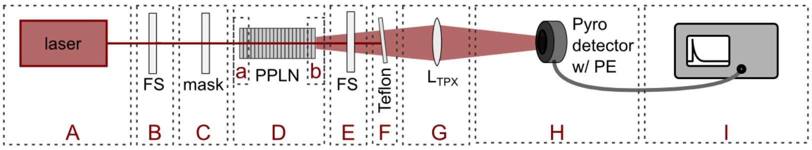

Figure 3.17.: Sketch to explain the calculation of the internal vs external efficiency and THz energy. The sections (A)-(I) are described in the text.

The energy of the laser E_A is measured in A before entering the generation setup. If a cryo-chamber is installed, the fused silica (FS) windows in part B and E are indispensable for the calculation. The input window in B is AR coated for the IR pump. Therefore the pulse energy E_p is varied by

$$E_B = E_A \cdot T_{FS,IR}, \tag{3.5.3}$$

where $T_{FS,IR} = 99.8\%$ is the transmission of the AR-coated FS window. The mask, which is installed in front of the crystal (C) has a transmission T_{mask} depending on the laser beam size and the mask dimensions. The transmission has to be measured at every setup to ensure the right amount of pump energy. With the transmission of the mask the pump energy which determined the pump fluence F_{pump} can be calculated via

$$E_C = E_B \cdot T_{mask} = E_A \cdot T_{FS} \cdot T_{mask} \equiv E_{pump} = F_{pump} \cdot A, \tag{3.5.4}$$

where A is the size of the beam behind the mask.

The last influence on the pump pulse is the transmission loss at the input surface of the lithium niobate crystal (D a). The refractive index of $n_{IR} \approx 2.17$ results in a transmission of $T_{LN,IR} = 0.85$ calculated via equ. 2.1.14 as long the crystal is not AR coated. Therefore the energy in the PPLN crystal is

$$E_{D,a} = E_{pump} \cdot T_{LN,IR}, \tag{3.5.5}$$

which is relevant for the efficiency calculation. The pump energy E_{pump} generates a THz pulse with an energy of

$$E_D = \eta \cdot E_{pump}. \tag{3.5.6}$$

This efficiency η is in this thesis defined as the "internal" efficiency. The "internal" efficiency is the ideal efficiency as all effects resulting from engineering factors like as example AR coatings are neglected. This "internal" efficiency is easier to compare to the simulations. In the experiments of this thesis the "internal" efficiency is named conversion efficiency or efficiency without the extension of "internal".

Due to the high refractive index of $n_{THz} \approx 5$ in lithium niobate in the THz range, the transmission loss is $T_{LN,THz} = 0.55$ (see section 2.1.1). The THz energy after the PPLN is reduced to

$$E_{D,b} = E_D \cdot T_{LN,THz} \equiv E_{THz}. \tag{3.5.7}$$

In this thesis this energy E_{THz} is the presented value if nothing else is mentioned. The additional transmission losses on the THz energy at the FS window ($T_{FS,THz}$), the Teflon plate (T_T) and the TPX lens (T_{TPX}) are highly depending on the generated frequency and thickness as explained in section 2.1.1. If the TPX lens is replaced by two OAPs to detect the energy, this loss has to be taken into account. The energy infront of the detector calculates as

$$E_H = E_{D,b} \cdot T_{FS,THz} \cdot T_T \cdot T_{TPX}. \tag{3.5.8}$$

Using the THz signal U at the detector, which is displayed in (I), the THz energy before the detector can be calculated with the voltage response of the detector $r_d = 1.61\,\mathrm{nJ/mV}$ as

$$E_H = U \cdot r_d. \tag{3.5.9}$$

To conclude, the generated THz energy and the "external" (η_e) as well as the "internal" (η_i) conversion efficiency can be calculated via

$$\begin{aligned}
E_{THz} &= \frac{r_d}{T_{FS,THz} \cdot T_T \cdot T_{TPX}} \cdot U && (3.5.10)\\
\eta_e &= \frac{E_{THz}}{E_{pump}} && (3.5.11)\\
&= \frac{r_d}{T_{FS,THz} \cdot T_T \cdot T_{TPX}} \cdot \frac{U}{E_{pump}} && (3.5.12)\\
\eta_i &= \frac{E_{THz}}{E_{pump} \cdot T_{LN,IR} \cdot T_{LN,THz}} && (3.5.13)\\
&= \frac{\eta_e}{T_{LN,IR} \cdot T_{LN,THz}} && (3.5.14)\\
&= \frac{r_d}{T_{LN,IR} \cdot T_{LN,THz} \cdot T_{FS,THz} \cdot T_T \cdot T_{TPX}} \cdot \frac{U}{E_{pump}}. && (3.5.15)
\end{aligned}$$

After calibrating all transmission losses experimentally the THz energy and the conversion efficiency are just depending on the input energy and the detector signal. The calibration is repeated at all THz generation setups to provide a consistent procedure.

3.5.4. Frequency measurement

The generated THz pulse is defined by its frequency. There are two options to measure the frequency: first of all via EOS or second via an interferometric measurement. We use the second principle. For the high energy lasers like ANGUS the EOS is less suitable as it is not easy to get a compressed laser pulse which is synchronized to the chirped driver pulse. Therefore an interferometric setup was build as depicted in figure 3.18. The setup is based on a Michelson interferometer and uses a 3.5 mm silicon (Si) wafer as beam splitter (BS). Si has a splitting ratio of ∼50% in the THz range.

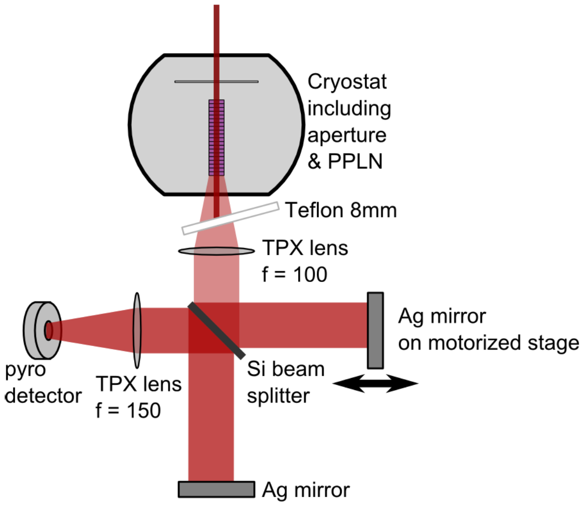

Figure 3.18.: Setup for the THz interferometer to measure the THz frequency.

After dumping the IR in the Teflon plate, the generated THz pulse is collimated with a TPX lens (f=100 mm) and transported to the interferometer. The Si-BS splits the beam into two arms. Two silver mirrors, one of these is mounted on a motorized translation stage, are reflecting the two arms back and the Si-BS is combining them. The second TPX-lens (f=150 mm) is then focusing on the pyroelectric-detector. The setup is aligned, so that both arms are equally long if the motorized mirror is approximately in the middle of the stage. In this case the full beam can be characterized as long as the stage is long enough. When the stage is traveling the two arms are interfering with each other and generate an interferogram. In general, if the delay arm is traveling a distance d the delay between both arms is $\Delta w = 2d$, which correspond to a wavelength $\lambda = 2\,\Delta w$. The time delay between the two arms can be calculated as

$$\Delta t = \frac{\Delta w}{c}. \tag{3.5.16}$$

As the generated pulses are narrowband, also a short measurement over some interference peaks already determined the frequency $\nu = \frac{1}{2\Delta t}$. The interference pattern can be fitted via

$$I(x) = I_0 + C \sin\left(\pi \frac{(x - x_0)}{d}\right) \quad \text{or} \tag{3.5.17}$$

$$I(t) = I_0 + C \sin(2\pi\nu(t - t_0)), \tag{3.5.18}$$

depending on the delay axis. The frequency and the wavelength can be approximated if a short interference pattern is measured. The precision increases with a longer duration of measurement until the whole pulse is evolved. The precise calculation of the frequency and the wavelength is achieved by a FFT of the interference pattern.

Evolving the whole pulse allows to measure also the pulse duration of the THz pulse τ_{THz}. The envelope of the interference pattern is a convolution of two THz pulses with the same pulse duration. The FWHM of the envelope of the convoluted pulse is thus $\sqrt{2}$ times shorter than the pulse duration of the THz pulse. This measurement is limited by the collimation of the THz pulse: the longer the pulse gets the longer the THz has to travel collimated, which is challenging for this wavelength. Therefore the measured pulse duration is a lower bound of the actual duration.

The interferometer is capable to measure the frequency of the THz pulse as well as the lower bound of the pulse duration and is a necessary detection setup to prove the narrowness of the pulses as well as the generated frequency.

3.6. Summary

This section provides an overview about multi-cycle THz generation in periodically poled lithium niobate. The theoretical background of quasi phase-matching and THz generation via OR or DFG is introduced. The general experimental resources such as the crystals and the pump lasers and the measurement tools necessary to conduct the experiments are explained.

The experiments to increase the THz energy by either pumping with a train of compressed pulses or pumping with chirp-and-delayed pulses will be discussed in the next two chapters.

4. Generation of multi-cycle THz pulses via pulse-train pumping

This chapter describes how narrowband THz pulses are generated via optical rectification of compressed pump pulses in a periodically poled lithium niobate crystal. By using a train of pulses instead of a single pulse the pump intensity is reduced while maintaining the total incident pump fluence. This proof of concept shows that a sequence of pulses enhances the generated THz energy without damaging the crystal. The concept of optical rectification with a train of pulses and the results with a pulse-train with two pulses of equal energy followed by several lower-energy pulses are described in the following sections.

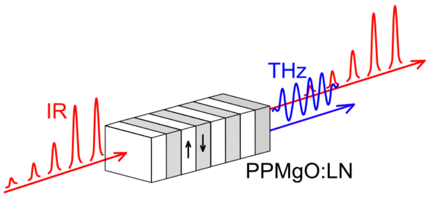

Figure 4.1: Schematic drawing to illustrate the THz generation via pulse-train pumping.

4.1. Concept of pumping with a sequence of pulses

The efficiency of THz generation via optical rectification in a PPLN is proportional to the energy of the pump pulse (see section 3.1.3). By splitting the energy of the pump pulse into N equally distributed pulses the energy of each pulse is $1/N$. Each of the pulses generates a THz pulse with $1/N^2$ of the energy of the single pulse as the energy and the efficiency are reduced by $1/N$. This is valid only if the energy is low enough that the efficiency is linearly varying with pump fluence, which is the case for low pump fluences.

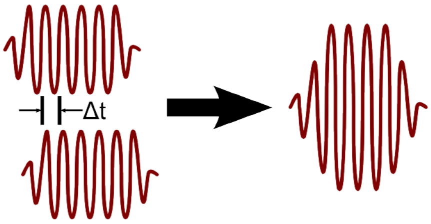

Figure 4.2: The THz waves delayed by a time delay $\Delta t = 1/\nu$ to each other are constructively interfering in the PPLN.

The field of each THz pulse is thus reduced by $1/N$. Each of the generated THz fields add coherently if the delay Δt between the pulses is tuned to the optimal delay Δt_{opt}

$$\Delta t_{opt} = \frac{1}{\nu}, \tag{4.1.1}$$

where ν is the phase-matched frequency of the THz pulses in the PPLN (see figure 4.2). The superposition of the N generated THz fields is $N \cdot 1/N$ and therefore equals the field generated by a single pulse.

However, if the pump energy is so high that the efficiency is saturated, the splitting into several pulses is just changing the energy of the input pulses. The energy of each THz pulse is reduced by $1/N$ as the efficiency at $1/N$ of the energy is unchanged. Coherent addition of the generated THz fields leads to an overall efficiency of $\eta_{tot} = N \cdot \eta$, where η is the efficiency of the single pulse.

The limiting factor for going to higher pump energies is the damage threshold of the PPLN. The efficiency maximally achievable can also be explained with the damage fluence of the crystal. The damage fluence scales with the square root of the pulse duration $\sqrt{\tau}$ [Boy03]. Therefore, a train of N pulses with an effective damage threshold pulse duration $\tau_p = N\tau$ can be loaded with $\sqrt{N}$ times more fluence. The damage peak intensity of the train of N pulses with equally distributed energy is than $1/\sqrt{N}$ times the peak intensity of a single pulse [Rav16b]. The conversion efficiency at the same energy is enhanced by $N/\sqrt{N} = \sqrt{N}$. The efficiency maximally achievable is limited to $\sqrt{N} \cdot \sqrt{N} = N$ times the efficiency η due to the possible higher energy load. The generated terahertz wave has a higher peak-field due to the constructive interference.

The high absorption coefficient of lithium niobate at room temperature of $\alpha = 7\text{cm}^{-1}$ at a frequency of 0.56 THz has to be taken into account as its limits the coherent addition. The total electric field $E^{(t)}_{\text{THz}}$ is then

$$\begin{aligned} E^{(t)}_{\text{THz}} &= E^{(1)}_{\text{THz}} + E^{(2)}_{\text{THz}} \cdot e^{-\alpha \cdot d} + E^{(3)}_{\text{THz}} \cdot e^{-2 \cdot \alpha \cdot d} + \dots & (4.1.2) \\ &= E^{(1)}_{\text{THz}} + E^{(2)}_{\text{THz}} \cdot e^{-\alpha \cdot \Delta t_{\text{opt}} c / n^g_{\text{IR}}} + E^{(3)}_{\text{THz}} \cdot e^{-2 \cdot \alpha \cdot \Delta t_{\text{opt}} c / n^g_{\text{IR}}} + \dots, & (4.1.3) \end{aligned}$$

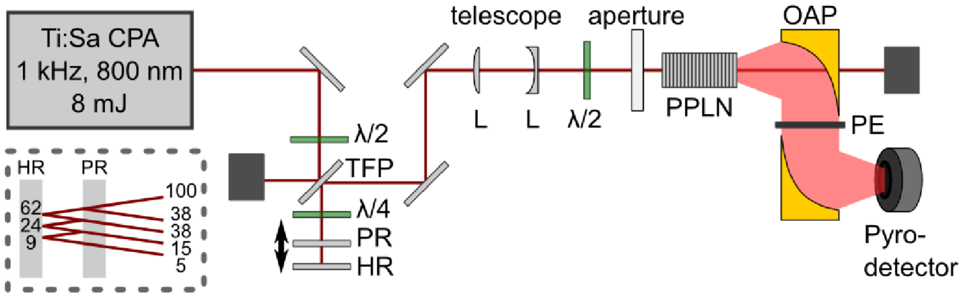

Figure 4.3.: Pulse-train setup using a combination of partial reflector (PR) and high reflector (HR) to generate a pulse-train with a pulse pair plus lower-energy trailing pulses (inset). **KEY:** $\lambda/2$: half wave-plate; TFP: thin film polarizer; $\lambda/4$: quarter wave-plate; L: lens; PPLN: periodically poled lithium niobate; OAP: off-axis parabola; PE: polyethylene.

where d is the distance in the PPLN between the two IR pulses. In the experiment a 38% partial reflector is used to generate two pulses with equal energy followed by several lower energy pulses. Considering the absorption in lithium niobate the efficiency increases by a factor of $(E^{(t)}_{\mathrm{THz}}/E_{SP})^2 = 2.67$ for this train of two pulses of equal energy followed by lower energy pulses compared to a single pulse. The pulse-train pumping opens a new opportunity to increase the overall efficiency of the optical rectification.

4.2. Experimental setup

Figure 4.3 shows the pulse-train setup schematically. A Ti:sapphire (Ti:sapp) cryogenic cooled chirp pulse amplification (CPA) laser system with an energy of up to 8 mJ at 1 kHz repetition rate is used as the pump source for the THz generation. The Ti:sapp laser pulses are compressed to pulse duration of 176 fs with a center wavelength of $\lambda = 807.5\,\mathrm{nm}$. The part of the experimental setup where the pulse-train is generated consists of a 38% beam splitter (BS) and a high reflector (HR) generating a pulse-train with two equal pump pulses and several additional lower-energy pulses (figure 4.3 inset). This combination allows us to use the full input energy and to generate two identical pulses. A tunable delay Δt between these two mirrors allows to match the time period T_0 corresponding to the phase-matched terahertz frequency ν_{opt}.

By using a thin film polarizer (TFP) and a quarter-waveplate ($\lambda/4$) the full energy which is transmitted through the TFP is reflected on the way back. This combination of optical elements protects the laser from backreflections and allows a finetuning of the energy with the half waveplate ($\lambda/2$) in front of the TFP. The pump beam size is adjustable with a telescope in front of the PPLN. The polarization of the pump pulse has to match the axis with the highest nonlinear coefficient (c-axis) to efficiently generate THz pulses. A half-waveplate in front of the PPLN allows tuning of the polarization. In this experiment PPLN crystals of poling periods $\Lambda = 400,\ 212,\ 125\,\mu\text{m}$ with an aperture of 3 mm x 10 mm and a length of 10 mm are characterized. The beam size is restricted to 1.5 mm ($1/e^2$) radius at the input facet of the crystal with a ceramic mask. To increase the pump fluence on the crystal the telescope can be used. The THz beam is imaged with two 90° off-axis parabola (OAP) onto the pyro detector to measure the THz energy. The first OAP has a hole at the center to transmit most of the pump energy and to allow an analysis of the transmitted pump pulse. The residual pump energy is blocked either by a 3mm thick polyethylene window (PE) with a transmittance of 66% at the THz frequency range or a 10 mm Teflon window with a transmittance of 76%. The terahertz power is measured with a pyroelectric terahertz detector (Gentec-EO, THZ9B or SDX-1152) with a PE window. The losses of the OAP, the PE or the Teflon and the Fresnel losses for THz at the output face of the PPLN are accounted.

4.3. Measurement of THz frequency

The poling period, Λ, defines the generated terahertz frequency, ν, according to:

$$\nu = \frac{c}{\Lambda \Delta n}, \tag{4.3.1}$$

where Δn is the difference between the group velocity index of the pump pulse and the refractive index at the desired THz frequency (see section 3.1.2). *Carbajo et al.* [Car15] verified for the poling periods $\Lambda = 400,\ 212,\ 125\,\mu\text{m}$ which are also used for this experiment the phase-matched frequencies of $\nu = 275\,\text{GHz}$, $513\,\text{GHz}$ and $867\,\text{GHz}$, respectively. The pulse-train concept is also well suited to measure the frequency of the generated THz pulse as the optimal delay is inversely proportional to the frequency of the THz pulse. While varying the delay between the pulses by moving the beam splitter, the generated

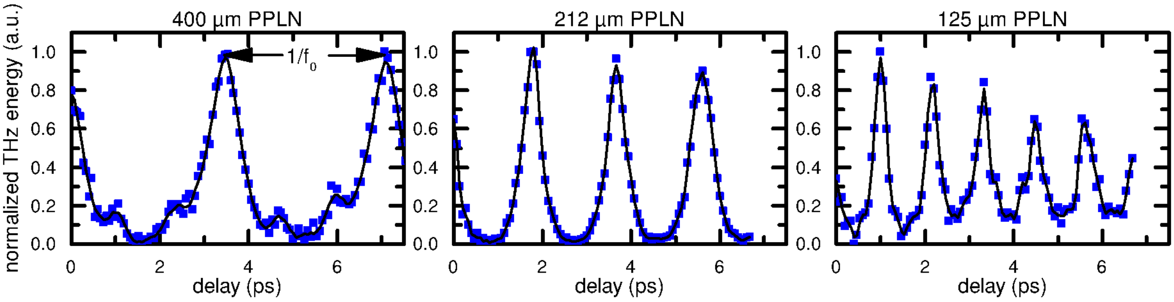

Figure 4.4.: Normalized THz energy vs. pulse train delay for 10 mm long PPLNs with Λ = 400, 212, 125 µm at 300 K. Maximal energy at delay of 3.5 ps, 1.8 ps, 1.1 ps and corresponding peak frequencies of 285 GHz, 535 GHz and 899 GHz. [Ahr16]

terahertz energy for each of the PPLNs is measured. Figure 4.4 shows the normalized terahertz energy as a function of relative delay between the two pulses of the pulse train for different poling periods. At the delay Δt_{opt} corresponding to the inverse of the phase-matched frequency the generated THz pulses interfere constructively. In table 4.1 the results are summarized.

As expected, the measured time delay between the pulses and the corresponding terahertz frequencies ν = 284 GHz, 538 GHz and 901 GHz match the expected values within the measurement uncertainties. An autocorrelator is used to measure the pulse train at the measured optimal pulse delay for the THz generation with the 212 µm poled PPLN crystal. The time delay between the pulses is 1.92 ps corresponding to a frequency of 521 GHz matching the expected value. As seen in figure 4.4 for the 212 µm and the 125 µm PPLN the maxima of the THz energy are decreasing for higher pulse delays. The decay for a longer delay between the pump pulses can be explained by the THz absorption in the PPLN-crystal. This effect has increasing relevance for higher THz frequencies as the THz absorption coefficient is increasing with higher frequencies (see section 2.2.1).

The first part of the experiment already proves, that constructive interference of the generated THz pulses occurs at the expected time delay between the pulses.

4.4. Efficiency increase

The concept of pulse-train pumping is mainly important for high intensities close to damage threshold. As the literature values for the damage threshold of lithium niobate

THz frequency by EOS	Poling period	Pulse delay	THz frequency by pulse-train
275 GHz	400 µm	3.52 ps	284 GHz
513 GHz	212 µm	1.86 ps	538 GHz
867 GHz	125 µm	1.11 ps	901 GHz

Table 4.1.: Measured frequency via EOS ([Car15]), corresponding poling period and measured pulse delay in the pulse-train experiment as well as the calculated THz frequency via equ. 4.1.1 for three different PPLNs.

are not fully consistent [Mas71, Fur91, Men16], the damage threshold for the pulse train and for the single pulse in the experimental configuration has to be measured. A x-cut magnesium oxide doped lithium niobate wafer is used to determine the damage threshold in both pumping schemes:

- for single pulse pumping the wafer damaged at a fluence of $80\,\mathrm{mJ/cm^2}$ or a peak intensity of $454\,\mathrm{GW/cm^2}$,
- for the pulse-train the wafer damaged at a fluence of $164\,\mathrm{mJ/cm^2}$ or a peak intensity of $354\,\mathrm{GW/cm^2}$.

The damage threshold is observed by the scattered light introduced by the surface damage. The following measurements are done ∼20% below the measured damage threshold of the wafer to reduce the risk of damage.

In figure 4.5 the extracted THz energy and the internal conversion efficiency for the pulse-train and for the single pulse are depicted. Compared to the single pulse pumping the pulse-train allows a higher pump fluence on the PPLN resulting in a higher output energy. An energy of around 0.85 µJ is achieved by pumping with the pulse-train. This result is comparable to the results of 1 µJ achieved by *Carbajo et al.* [Car15] where the single pulse generation is optimized by cryogenic cooling of the crystal and optimizing the pump pulse bandwidth. The efficiency of the single pulse pumping is already saturating at 0.02% whereas the the pulse-train saturates at 0.05%. Therefore the efficiency of the pulse-train is 2.6 times higher than for the single pulse. This high increase is a result of the coherent addition combined with the absorption in lithium niobate.

The PPLN with a poling period of 212 µm has the best performance compared to the other two crystals (see figure 4.6). The efficiency is depending on the frequency

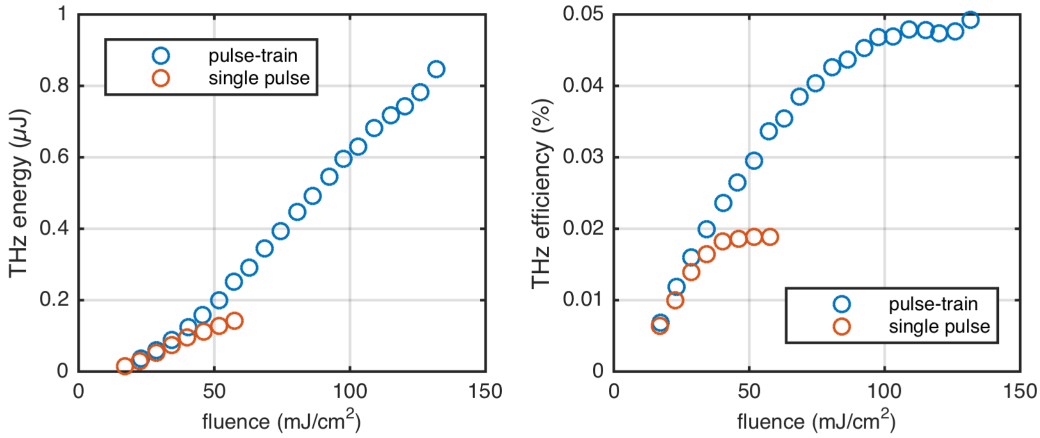

Figure 4.5.: THz energy (left) and internal conversion efficiency (right) of a pulse-train (blue) and a single pulse (red) for different pump fluences.

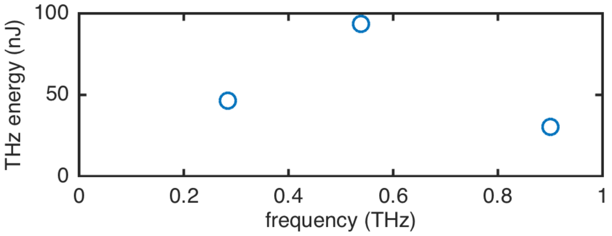

Figure 4.6.: THz energy generated at the optimal delay with a pump energy of 4.75 mJ for 10 mm long PPLNs with a poling period of 400, 212 and 125 μm with generated frequency of 0.284, 0.538 and 0.9 THz, respectively. The efficiency at the low frequency suffer from the frequency dependence Ω^2 and at the higher frequencies from the absorption coefficient α.

and the absorption: the lower the frequency the lower the efficiency of the process and the higher the frequency the stronger the material absorption. The first measurements are done with a 5 mm long PPLN with a poling period of 212 μm at relative low pump fluences of 22 mJ/cm^2. Hereby, the optical-to-terahertz conversion efficiency reaches $\eta = 2.9 \times 10^{-4}$, which matches the conversion efficiency achieved with a single pulse with the same total fluence and higher peak intensity. This experiment is in good agreement with the theoretical prediction for the case of unsaturated efficiency as described in section 4.1. The achieved efficiency with the 5 mm long PPLN is higher than for the 10 mm long crystal. This length scaling was also measured by *Carbajo et al.* [Car15].

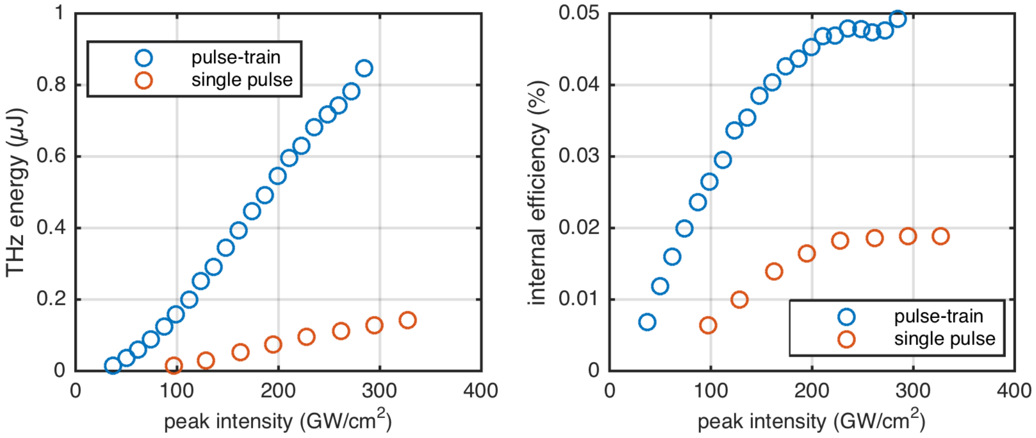

Figure 4.7.: THz energy (left) and internal conversion efficiency (right) of a pulse-train (blue) and a single pulse (red) for the peak intensity calculate via equ. 4.4.1 and 4.4.2.

The benefit of pumping with a pulse-train is even more striking looking at the THz energy versus the peak intensity. In figure 4.7 the THz energy and the internal conversion efficiency for different peak intensities are shown. The peak intensity of the single pulse (I_{SP}) and of the pulse-train (I_{PT}) are calculated via

$$I_{SP} = \frac{p2a \cdot E_p}{A \cdot \tau} \tag{4.4.1}$$

$$I_{PT} = 0.38 \cdot \frac{p2a \cdot E}{A \cdot \tau}, \tag{4.4.2}$$

where A is the 1/e^2 beam area (beam diameter is 2.92 mm), $p2a$ is the measured peak-to-average factor (2.4), τ is the measured pulse duration of 176 fs ($\tau_{\mathrm{IAC}} = 279$ fs) and E the measured energy of the pump pulse. The peak intensity of the pulse train decreases by the factor of 38% due to the splitting ratio. Close to the damage threshold intensity the efficiency of the pulse-train saturates and is increased by the factor of 2.6 compared to the single pulse.

Besides the energy analysis, the spectral analysis in the infrared enables to predict the intrinsic efficiency. Figure 4.8 shows the measured input and output spectra at a pump energy of 3.5 mJ. The optical input spectrum (blue solid line) has a center wavelength of 807.5 nm and the output spectra (red solid line) has a red-shift coming from the cascading due to the THz generation. A part of the photon energy of the input pulse (shadowed blue area) is shifted to higher wavelength (shadowed red area). The center of mass is at $\lambda =$ 821.1 nm corresponding to a frequency shift of 6.12 THz. Therefore the maximal efficiency

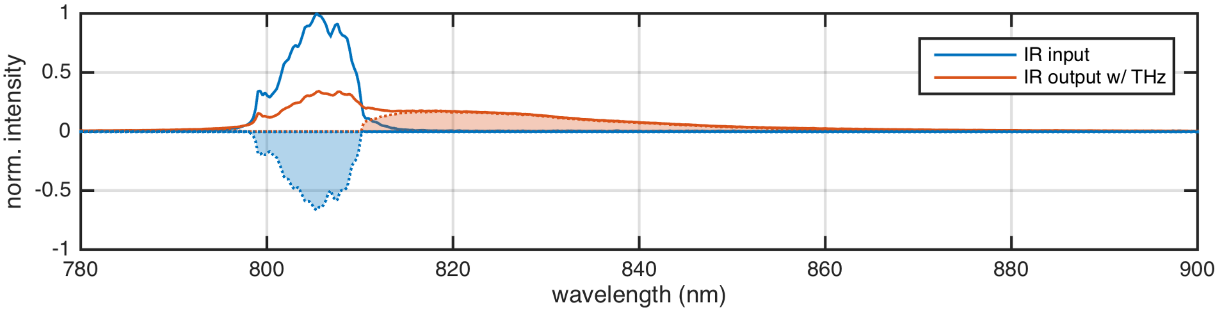

Figure 4.8.: Optical input (blue solid line) and output (red solid line) spectra measured at an energy of 3.5 mJ. The measured conversion efficiency for the THz is $\eta = 0.04\%$. The shadowed area is a guide to the eye for the cascading

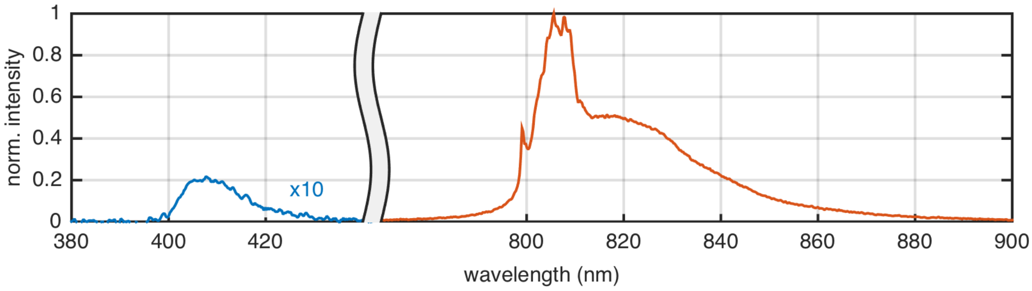

Figure 4.9.: Output spectra at a pump energy of 3.5 mJ with the broaden pump pulse (red line) and the generated, low power second harmonic (blue line) scaled by 10.

calculated from the frequency shift is $\eta_i = 1.65\%$ (see equation 3.1.22). The difference between the intrinsic efficiency and the measured efficiency ($\eta = 0.04\%$) is remarkable. It is explainable with the losses due to absorption in lithium niobate decreasing the outcoupled THz energy and influencing the coherent addition.

Second harmonic generation

At this experiment it is also possible to check if the second harmonic generation (SHG) is also phase-matched. In figure 4.9 the normalized output spectrum is shown around 800 nm and zoomed in around 400 nm. The SHG spectra centered at 405.3 nm is wider with a bandwidth of 15 nm. The SHG has just an efficiency of 1.4% confirming a phase-mismatch as for a phase-matched SHG the efficiency would be in the order of 42% [Mil97] or even 81% [Min05].

4.5. Conclusion and outlook

The concept to increase the efficiency of generating narrowband terahertz radiation in periodically poled lithium niobate by lowering the peak power while maintaining the peak fluence is experimentally proven. Comparing pulse-train pumping and single pulse pumping, an efficiency increase of a factor 2.6 was achieved in a PPLN with a poling period of 212 µm at room temperature. The maximal efficiency of 5×10^{-4} may be further improved by cryogenic cooling of the PPLN, which leads to a fivefold efficiency increase [Car15]. This concept allows new possibilities to increase the pump fluence without damaging the crystals while achieving higher terahertz energies. Further improvements are expected by increasing the number of pump pulses with the optimal delay. Optimizing the energy distribution in the pump pulse-train may also offer opportunities to fine-tune the generated terahertz waveform.

5. Generation of multi-cycle THz pulses with the chirp-and-delay pumping scheme

High energy narrowband terahertz pulses in the mJ-level provide access to several applications like electron acceleration or THz spectroscopy. As the Manley-Rowe relation limits the conversion efficiencies from the IR to the THz range to the range of 10^{-3}, optical pump sources in the Joule-level are required. The ANGUS system provides access to broadband, high energy pulses up to an energy of 6 J. By using the uncompressed laser pulses of the ANGUS system to pump the PPLN with high energy the aimed high energy THz pulses are generated. This section will describe three experiments:

- The technique of chirp-and-delay and the results at the setup with a pulse train generated by a partial and high reflector (section 5.1). The challenges of the first experimental setup will be discussed (section 5.2).
- The chirp-and-delay setup with two identical pulses generated by a Mach-Zehnder interferometer and the achieved results (section 5.3).
- The 2-pulse, chirp compensated setup with the first measurements to circumvent the challenge of having higher order dispersion in the uncompressed pulse (section 5.4).

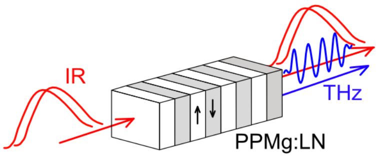

Figure 5.1: Schematic drawing to illustrate the THz generation via chirp-and-delay pumping

5.1. Narrowband terahertz generation with chirped-and-delayed laser pulses in periodically poled lithium niobate[1]

The last couple of decades have seen a tremendous surge in development of terahertz (THz) sources of high energy and high-peak field for applications ranging from linear and nonlinear THz spectroscopy [Heb08], to compact, THz-based electron acceleration [Nan15]. For spectroscopic applications, the low energy of THz photons enables non-ionizing time-resolved studies of material properties [Kam13], while for electron accelerators, the millimeter scale of THz radiation offers the advantages of compactness and high-acceleration gradients which are beneficial for driving ultrashort X-ray sources. Optically generated THz pulses based on difference frequency generation (DFG) are exceptionally promising for these applications due to the high efficiencies, high peak fields and high degree of tunability they offer. With the development of the tilted pulse-front technique [Ste03], percent-level optical-to-THz conversion efficiencies have been achieved – using Fourier limited broadband near-infrared (NIR) drivers incident on bulk lithium niobate (LN) – enabling generation of single-cycle pulses in the mJ-range. By comparison, the performance of equivalent sources of multi-cycle THz pulses has lagged behind. Multi-cycle pulses, which have narrower bandwidths and longer pulse durations in the order of tens of picoseconds, offer complementary parameters relative to single-cycle pulses, and are advantageous for applications such as driving linear accelerators [Nan15] and tuned excitation of specific material transitions [Bec13]. Recent work in THz generation has therefore seen a greater emphasis on development of efficient multi-cycle sources.

Among the primary challenges are achieving high conversion efficiencies and scaling to high energies. High efficiencies in nonlinear optical conversion processes require high incident optical intensities and management of the phase mismatch between optical and THz

---

[1] This subsection reproduces the paper *Narrowband terahertz generation with chirped-and-delayed laser pulses in periodically poled lithium niobate*, F. Ahr, S. W. Jolly, N. H. Matlis, S. Carbajo, T. Kroh, K. Ravi, D. N. Schimpf, J. Schulte, H. Ishizuki, T. Taira, A. R. Maier, and F. X. Kärtner, *Optics Letters* **42**(11), 2118 (2017) [Ahr17]. Together with S. W. Jolly and S. Carbajo I planned the experimental setup. S. W. Jolly and I setup the apparatus, conducted the experiments and performed the data analysis. Together with the other authors, I discussed the results and wrote the published article.

waves, which tends to be large in most nonlinear materials due to differences in the linear index for the two waves. Quasi-phase matching in PPLN has emerged [Lee00, Wei01, Vod06] as a promising candidate for phase-matching in narrowband THz generation due to the large second order susceptibility, χ_2, of lithium niobate. Recently, conversion efficiencies up to 0.12% and THz energies of $\sim 1\mu$J were demonstrated by using Fourier-limited femtosecond pump pulses with optimized bandwidths and by using cryogenic cooling to minimize THz absorption in the PPLN crystal [Car15]. To produce the mJ-level THz pulses needed for acceleration applications [Nan15], however, pump pulses in the range of 1 Joule are required. But scaling to Joule energies with short pump pulses is problematic because the incident energy is limited by the optically-induced damage threshold and by the limited aperture of commercially available PPLNs. A solution is thus to increase the pump pulse duration to allow greater energy to be carried without exceeding the intensity threshold for optical damage.

Temporally stretching of the NIR pump, as proposed in [Vod06, Rav16b], offers one method to increase the pulse duration and therefore scale up the pump-pulse energy. A side effect of chirping, however, is that the instantaneous spectral content of the optical pulse is reduced, limiting the nonlinear conversion process that requires simultaneous presence of optical photons with frequencies separated by the frequency of the generated THz. This effect can be compensated by adding a second chirped pulse with an appropriate delay to provide the required instantaneous spectral content.

The chirp-and-delay concept was first described in 1994 to produce tunable, narrowband THz waves via photoconductive antennas [Wel94]. Chirp-and-delay has been used to produce higher energy pulses of $10\,\mu$J [Che11] in a hybrid approach employing the tilted pulse front technique. These pulses contained around 10 optical cycles and are thus not ideal for applications requiring very narrow-band radiation, like electron acceleration. Here, we demonstrate use of chirp-and-delay in combination with a periodically poled medium for the first time and generate record energies of narrow-band multi-cycle THz radiation. We investigate PPLN with varying poling periods and crystal lengths and study the effect of cryogenic cooling on the conversion efficiency.

DFG requires the presence of two distinct frequency components overlapped in space and time. These components can be provided by a single pulse of sufficiently large bandwidth or by two narrow-band pulses with distinct central frequencies. In the chirp-and-delay concept, two narrow-band components are provided by broadband but chirped pulses combined with well-defined temporal delay, Δt, as schematically illustrated in Fig. 5.2a. In this case, the instantaneous angular frequency of each pulse varies linearly in time, but the instantaneous angular frequency difference, $\Delta\omega$, is fixed by the delay and the chirp rate as shown in Fig. 5.2b. The delay can then be tuned so that $\Delta\omega(\Delta t_{\text{opt}}) = \Omega$,

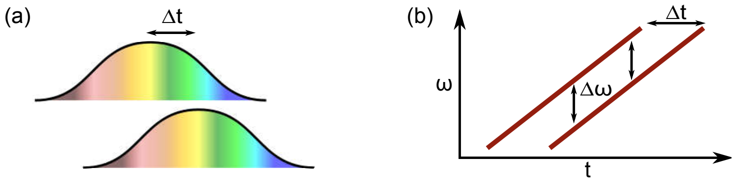

Figure 5.2.: a) Conceptual temporal arrangement of collinear chirp-and-delay pulses. **b)** Wigner-plot illustrating the spectral content of the chirp-and-delay pulses vs. time.

where Δt_{opt} is the optimal delay to achieve the desired THz frequency Ω. Assuming a second order spectral phase coefficient, i.e. group-delay dispersion (GDD), of ϕ_2, which is equivalent to a linear chirp rate of $1/\phi_2$, the optimum delay is

$$\Delta t_{opt} = \Omega\,\phi_2. \tag{5.1.1}$$

Optimizing THz generation in periodically poled crystals requires $\Delta\omega$ to be tuned to the phase-matched THz frequency, $\nu_{\text{THz}} = \Omega/2\pi$, which is primarily determined by the poling period according to

$$\Omega = \frac{2\pi\, c}{\Lambda|n(\Omega) - n_{\text{g}}|}, \tag{5.1.2}$$

with c the speed of light, Λ the poling period, and $n(\Omega)$ and n_{g} are the phase and group refractive indices for the THz and IR waves respectively [Fej92, Yam93]. To a lesser extent, Ω is also determined by the temperature through the temperature-dependent indices of refraction [Yu11, Car15]. The relative THz bandwidth, $\Delta\Omega/\Omega$, and hence the number of cycles generated, N, is decreasing with the crystal length L [Vod06, Cao09]. By contrast, in narrowband THz generation with bulk LN, where direct phase matching via a tilted pulse-front pumping takes place, the THz pulse length, and thus the number of optical cycles, is directly defined by the IR pulse duration [Che11].

Experiments were done using the ANGUS 200 TW double CPA, Ti:Sa-based laser system providing 5 J pulses at 5 Hz, compressible to 25 fs. The spectrum was centered at 800 nm with a 35 nm FWHM bandwidth, resulting in chirped pulses of 260 ps FWHM, duration and GDD of $\phi_2 = 2.3\,\text{ps}^2$ before compression. A train of pulses of identical, nearly linear chirp and tunable delay was created from the uncompressed beam by using a 38 % partial reflector (PR) mounted on a delay stage with the PR coating facing a high reflector (HR), as shown in Fig 5.3a. This combination resulted in two pump pulses of approximately equal intensity followed by a series of pulses with significantly lower energies originating from the multiple reflections. The energy of the pulses was tuned using a waveplate and two thin film polarizers (not shown), while a second half-waveplate (WP) matched the polarization of the chirped-and-delayed pulses to the optical axis of the PPLN. Two cylindrical telescopes matched the beam shape to the clear aperture of the PPLN: the tangential and sagittal telescopes reduce the vertical and horizontal beam size to 3 mm and 10 mm, respectively to match the aperture of the PPLN. The PPLN was mounted in a cryostat for cryogenic cooling using liquid nitrogen to reduce THz absorption in the crystal. A ceramic aperture installed inside the cryostat just in front of the PPLN input surface mitigated the heat load and acted as a mask to shape the beam and ensure it wasn't clipped by the crystal. The entrance and exit ports of the cryostat were fused silica windows anti-reflection (AR) coated for 800 nm. The transmission ratio of the windows

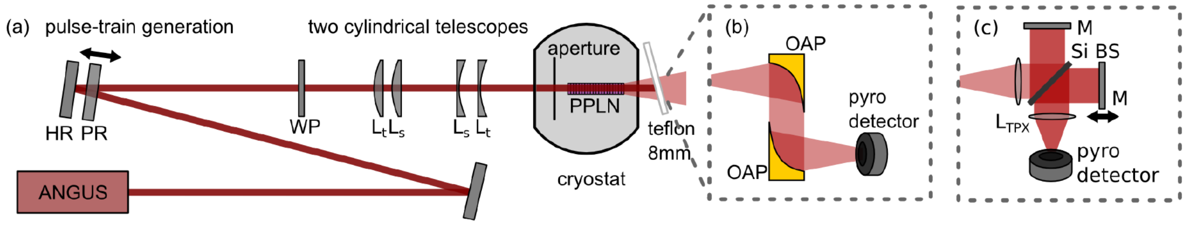

Figure 5.3.: a) Chirp-and-delay setup using a combination of partial reflector (PR) and high reflector (HR) to generate a chirped pulse pair plus lower-energy trailing pulses. **b)** THz pulse energy measurement setup. **c)** THz frequency measurement setup based on Michelson interferometer. **KEY:** WP: half wave-plate; L_s: sagittal lens; L_t: tangential lens; OAP: off-axis parabola; L_{TPX}: TPX lens; M: Silver mirror; Si BS: silicon beam splitter.[2]

---

[2] Figure is slightly modified compared to paper to match the page size

for THz pulses was calibrated independently, and was found to be 80% in our frequency range.

THz was generated using PPLN crystals of four different poling periods: $\Lambda = 125\,\mu$m, $212\,\mu$m, $330\,\mu$m, and $400\,\mu$m, obtained from HC Photonics (excluding the PPLN at $330\,\mu$m, which is provided by Prof. T. Taira). To measure the THz pulse energy, two 2" gold-coated off-axis parabolas of 4" focal length were used to collect the THz and focus it onto a pyro-detector (Gentec-EO: THZ9B-BL-BNC). In an interchangeable setup, the frequency of the THz was measured using a Michelson interferometer with a 3.5 mm thick silicon wafer as a beamsplitter and a variable delay on one arm. The THz was collimated into the interferometer using a 100 mm focal length TPX lens. The interference pattern was determined by focusing the THz with a second TPX lens onto the pyro-detector and scanning the variable delay. An 8 mm thick teflon plate (THz transmission of 80 %) was used to dump the IR pump before the THz detection setups and to allow measurement of the transmitted optical spectra using an HR4000 fiber spectrometer (Ocean Optics).

In order to verify the chirp-and-delay mechanism we measured the dependence of the optimum delay on the frequency of the generated THz, which, from Eq. 5.1.1, we expect to be linear. The THz frequency was varied by using crystals of different poling period, and the THz output was measured as a function of the delay, (by scanning the position of the PR), for each of the four poling periods (Fig. 5.4). Panel 5.4a) shows that the optimum delay depends inversely on the poling period, as expected from Eqns. 5.1.1 & 5.1.2. We note the development of additional substructure for higher delays, which we attribute to the presence of residual third-order dispersion in the chirped pulses and the presence of a pulse train from the HR/PR combination rather than the ideal case of two isolated pulses. A detailed analysis of these effects has been done, but is beyond the scope of this work and will be presented elsewhere [Jol17][3].

The connection between the poling period and the THz frequency is well established, and has been measured previously [Car15]. For completeness, however, the frequency of the THz generated by the $330\,\mu$m and $212\,\mu$m poling period crystals, (which produced the larger signals), was measured using the interferometer. Figures 5.4b & c are showing these interferometic traces, which are subsets of longer measurements, that show greater than 60 cycles for the $330\,\mu$m PPLN. Using sinusoidal fits, THz wavelengths of 0.83 mm

---

[3] Analysis is done in section 5.2

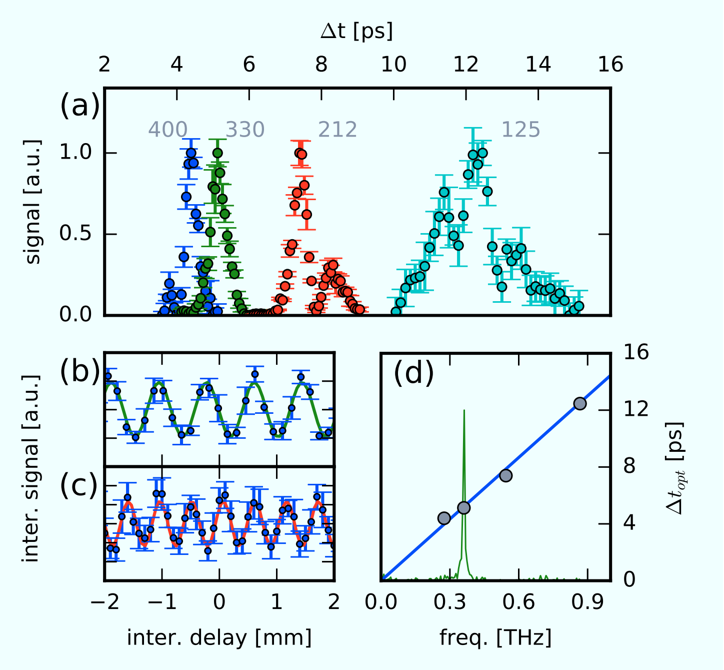

Figure 5.4.: a) Normalized THz signal vs. delay for PPLN poling periods of 400 μm, 330 μm, 212 μm and 125 μm. **b) & c)** Interferometer data (dots) and sinusoidal fits (lines) for crystals of poling period 330 μm and 212 μm yielding THz wavelengths of 0.83 mm and 0.55 mm, respectively. **d)** Comparison of measured (red dots) and predicted (blue line) optimum delays for four poling periods.

and 0.55 mm, corresponding to frequencies of 0.361 THz and 0.544 THz were determined, in good agreement with the values of 0.341 THz and 0.532 THz, respectively, predicted by Eq. 5.1.2 and using refractive indices from [Wu15]. For the 125 μm and 400 μm poling period crystals, which produced smaller THz signals, we used values for the frequencies of 0.867 THz and 0.275 THz respectively, which we measured using the identical crystals in a previous work [Car15].

The dependence of the optimal delay on THz frequency is plotted in Figure 5.4d. The measured delays (red dots) agree well with the prediction based on Eq. 5.1.1 and using the GDD of the Angus system, verifying the chirp-and-delay mechanism. For example, the 330 μm poling period crystal had a measured optimum delay of $\Delta t = 5.13$ ps in very good agreement with the predicted delay of 5.22 ps at 0.361 THz

The chirp-and-delay scheme was optimized by studying the THz output as a function of the incident pump fluence for varying crystal temperatures and interaction lengths.

To distinguish between the intrinsic performance of the scheme and engineering factors such as transport of photons to and from the crystal or Fresnel losses at the surfaces, the performance was characterized using two primary metrics: 1) the internal conversion efficiency (hereafter, "efficiency"), defined as the ratio of the THz energy before exiting the crystal rear surface and the IR input energy after entering the crystal front surface and 2) the THz energy extracted from the crystal. A so-called extracted efficiency in this case would be 2.1 times lower than the internal efficiency due to Fresnel losses. Figure 5.5 shows the conversion efficiency vs. incident pump fluence at room and cryogenic temperatures for two crystal lengths of 212 μm-poled PPLN.

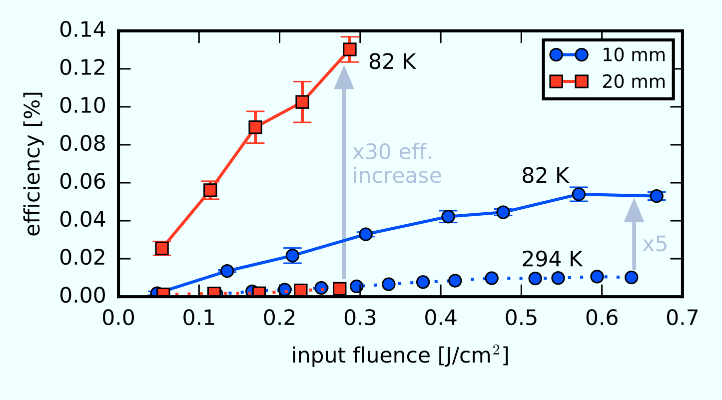

Figure 5.5.: Conversion efficiency of 212 μm poling period PPLNs at room- (dotted) and cryogenic (solid) temperature as a function of pump fluence, showing drastic improvement with cooling.

At room temperature (294 K), the efficiency is nearly identical for the 10 mm and 20 mm long crystals. This can be explained by the large absorption coefficient of lithium niobate (5.2 cm^{-1} [Wu15]) at room temperature which limits the effective interaction length to only a few millimeters for both crystals [Lee00, Car15]. By cooling the crystals to 82 K the absorption coefficient was reduced to 2.8 cm^{-1} [Wu15], which significantly increased the effective interaction length, allowing greater advantage to be taken of longer crystals and thus improving the conversion efficiency. Compared to room temperature, the cryo-cooled 10 mm long crystal showed a five-fold increase in conversion efficiency, while the 20 mm long crystal showed a 30-fold increase, demonstrating the compounding benefits of reducing the THz absorption. For the 10 mm crystal, the efficiency saturated at a value of 0.054 % at a pump fluence of 0.571 J/cm^2, still below the damage threshold. For the

20 mm crystal by contrast, damage was observed at a lower threshold than expected, and limited the efficiency to 0.13 % at a pump fluence of 0.287 J/cm^2, where saturation had not yet occurred.

A record multi-cycle THz energy of 40 μJ was achieved at a frequency of 0.544 THz, using the 10 mm, 212 μm-poled PPLN crystal (with an aperture of 3 mm × 10 mm) at cryogenic temperature. Although the 20 mm piece exhibited a higher peak efficiency, the energy output was limited to 12.8 μJ by a smaller aperture of 3 mm × 3 mm.

The transfer of energy between the optical and THz fields necessarily results in a modification of the optical spectrum, providing another means of diagnosing the nonlinear process. For instance, conservation of energy dictates that the centroid shift of the optical spectrum represents an upper limit to the conversion efficiency. In addition, for efficient terahertz generation an energy transfer process known as cascading is required to circumvent the Manley-Rowe limit [CG04]. During cascading, optical photons interact nonlinearly multiple times, producing multiple THz photons for each optical one. This process can result in both red- and blue-shifting of these photons by multiple times the frequency of the THz photons. These effects are illustrated in figure 5.6. The transmitted optical spectrum shows an overall red-shift of the centroid from 798.1 nm before the interaction to 801.4 nm after the interaction, corresponding to an energy loss of 0.41%. The difference spectrum (shaded gray) also shows evidence of the cascading process since the red- and blue-shifts of ~20 nm correspond to roughly 17× the THz photon energy.

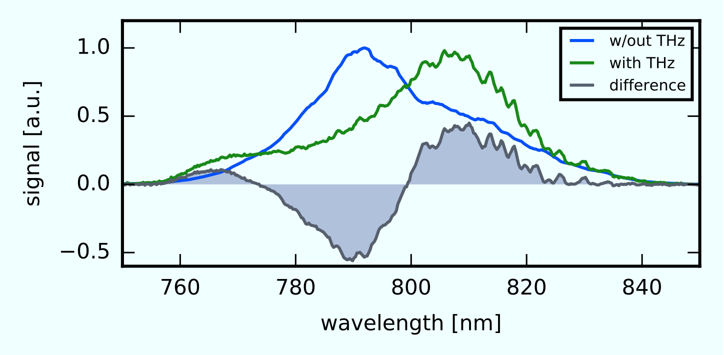

Figure 5.6.: Transmitted pump spectra before (blue) and after interaction with the 212μm PPLN (green). The shadowed graph demonstrates an energy transfer due to THz generation. For this measurement the crystal was cooled to 82 K and operated with a pump fluence of $F = 0.287$ J/cm^2.

The proof-of-principle results demonstrated here can be improved upon in several ways. Of particular importance is implementation of an AR coating to reduce the ∼44% loss to the extracted THz energy from Fresnel reflections at the crystal exit face. In addition, the small amount nonlinear chirp imparted to the optical beam by the ANGUS stretcher is estimated to induce a frequency difference that varies over the spectrum of the two chirped pulses such that only a portion of the pump pulses are phase-matched to the THz frequency. Compensating for the higher order dispersion in the pump pulse, we estimate a significantly increased conversion efficiency, approaching the 1 % level for a 212μm-poled PPLN crystal [Jol17]. Finally, by increasing the crystal aperture sizes to the maximum that is currently possible [Ish12], it may be possible to increase pump energies to the Joule level and take full advantage of the capabilities of current Ti:Sa laser systems. Chirp-and-delay pumping of PPLN is thus a promising scheme for generating narrowband THz pulses at the mJ level required by future applications.

5.2. Challenges at chirp-and-delay pumping with train of pulses

This section presents the results on the chirp-and-delay setup with a train of pulses which are in addition to or beyond the measurements of section 5.1. As mentioned both the higher order dispersion and the presence of a pulse train results in some uncertainties and deviations compared to the expected result for two chirped-and-delay pulses. In the case of two chirped-and-delayed pulses the delay of them should depend only on the chirp rate ϕ_2 as described in equation 5.1.1. With an additional TOD on the input pulses the frequency delay is affected as explained in the following paragraph.

5.2.1. Higher order dispersion

To visualize the undesired effect introduced by the higher order dispersion on the pump pulse a spectral analysis of the generation process is well suited. As seen in figure 5.7 (left), just a small part of the spectrum around a wavelength of $\lambda = 800\,\mathrm{nm}$ has the correct time delay to match the QPM bandwidth of the PPLN. In this example the optical spectrum (blue) and the transmitted spectrum through a 10 mm long PPLN with a poling period of $\Lambda = 212\mathrm{\mu m}$ (red) are plotted for the optimal delay $\Delta t = 1.18\,\mathrm{mm}$ pumped with an energy of $E_{pump} = 47.5\,\mathrm{mJ}$. The interference noise on the transmitted spectra traces back to the high attenuation of the ANGUS pulse. The attenuator – a waveplate and two thin film polarizers – generate post pulses but these are not affecting the chirp and delay process.

The other parts of the spectra are not phase-matched in the PPLN for that particular time delay. By varying the time delay the part of the spectrum generating the THz pulse is traveling through the optical pump pulse (figure 5.7 (right)). This result supports the assumption that the TOD is influencing the chirp-and-delay concept.

The width of the phase matched spectra is around 1/5 of the full bandwidth of the input pulse. This leads to the assumption that compensating the effect of the TOD on the pump pulse increases the THz energy by a factor of 5.

To prove experimentally the hypothesis, that the TOD is influencing the chirp-and-delay concept, the optical spectrum is further analyzed. The analysis is based on the

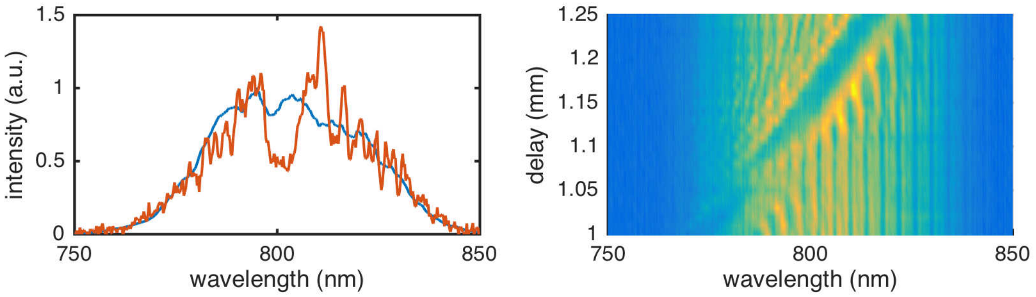

Figure 5.7.: Left: Optical pump spectrum entering the 10 mm long PPLN with a poling period of $\Lambda = 212\,\mu\text{m}$ as reference (blue) and the transmitted spectrum (red) at the optimal delay $\Delta t = 1.18\,\text{mm}$ with a pump energy of $E_{pump} = 47.5\,\text{mJ}$. Corresponding THz energy and conversion efficiency is $E_{\text{THz}} = 6.9\,\mu\text{J}$ and $\eta = 0.04\%$. **Right:** 2D intensity plot of the spectra versus the delay of the pulses.

general knowledge about dispersion. The spectral phase $\phi(\omega)$ of a pulse $E(\omega)$ is typically described as Taylor expansion around ω_0 as

$$\phi(\omega) = \left.\frac{d\phi}{d\lambda}\right|_{\omega_0} (\omega - \omega_0) + \frac{1}{2}\left.\frac{d^2\phi}{d\lambda^2}\right|_{\omega_0} (\omega - \omega_0)^2 + \frac{1}{6}\left.\frac{d^3\phi}{d\lambda^3}\right|_{\omega_0} (\omega - \omega_0)^3 + \dots \tag{5.2.1}$$

$$= \phi_1(\omega - \omega_0) + \frac{\phi_2}{2}(\omega - \omega_0)^2 + \frac{\phi_3}{6}(\omega - \omega_0)^3 + \dots, \tag{5.2.2}$$

where ϕ_1, ϕ_2 and ϕ_2 are known as group delay (GD), group delay dispersion (GDD) and third order dispersion (TOD). The higher dispersion components are regarded as low and are neglected. The GD, GDD and the TOD can be calculated via

$$\phi_1 = \frac{d\phi}{d\lambda} = \frac{1}{c}\left(n - \lambda\frac{dn}{d\lambda}\right) \cdot d \qquad \text{(GD)}, \tag{5.2.3}$$

$$\phi_2 = \frac{d^2\phi}{d\lambda^2} = \frac{\lambda^3}{2\pi c^2}\frac{d^2 n}{d\lambda^2} \cdot d \qquad \text{(GGD)}, \tag{5.2.4}$$

$$\phi_3 = \frac{d^3\phi}{d\lambda^3} = -\frac{\lambda^4}{4\pi^2 c^3}\left(3\frac{d^2 n}{d\lambda^2} - \lambda\frac{d^3 n}{d\lambda^3}\right) \cdot d \qquad \text{(TOD)}, \tag{5.2.5}$$

which is discussed in details for example by M. Hemmer [Hem11] in the analysis of a prism compressor. For the analysis of the effective GDD resulting from the higher order dispersion on the pump pulse the second order spectral phase ϕ_2 is important. As *Weiner* [Wei11] describes in his textbook the dispersion introduced by a material results in a temporal difference

$$\Delta\tau(\omega) = \Delta\omega \cdot \phi_2. \tag{5.2.6}$$

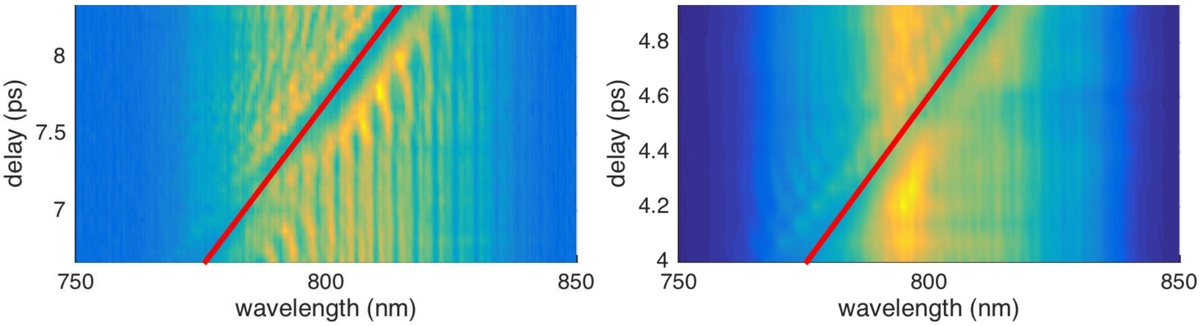

Figure 5.8.: Left: A 2D intesity plot of the transmitted optical pump spectrum through a 10 mm long PPLN with a poling period of $\Lambda = 212\mu m$ for varying delay between the two pump pulses. The white line indicates the GDD calculated via equ. 5.2.11. **Right:** A 2D intensity plot of the transmitted optical pump spectrum through a 36 mm long cryogenically cooled PPLN with a poling period of $\Lambda = 330\mu m$ for varying delay between the two pump pulses. The white line indicates the GDD calculated via equ. 5.2.13.

To write the temporal difference in dependence of the wavelength

$$\lambda = \frac{2\pi c}{\omega} \qquad \text{and} \qquad \frac{d\omega}{d\lambda} = \frac{-2\pi c}{\lambda^2} \tag{5.2.7}$$

have to be taken into account. The temporal difference can be written as

$$\Delta t(\lambda) = \frac{-2\pi c}{\lambda^2}\Delta\lambda \cdot \phi_2. \tag{5.2.8}$$

The effective GDD resulting from a material or other processes can be therefore written as

$$\phi_2(\lambda) = \frac{\Delta t}{\Delta\lambda}\frac{\lambda^2}{-2\pi c}. \tag{5.2.9}$$

The 2D intensity plots for two PPLN with a poling period of $\Lambda = 212\,\mu m$ (left) and $\Lambda = 330\,\mu m$ (right) is depicted in figure 5.8. The fitted curves (red) are indicating the "dip" traveling through the optical spectrum and can be calculated as

$$\Delta t_{212} = \frac{t_{min} - t_{max}}{\lambda(t_{min}) - \lambda(t_{max})} \cdot \lambda + t_{max} - \frac{t_{min} - t_{max}}{\lambda(t_{min}) - \lambda(t_{max})} \cdot \lambda(t_{max}) \tag{5.2.10}$$

$$= 0.0431\frac{\text{ps}}{\text{nm}} \cdot \lambda + 8.339\text{ps} - 0.0431\frac{\text{ps}}{\text{nm}} \cdot 814.6\,\text{nm} \tag{5.2.11}$$

for the PPLN with a poling period of $\Lambda = 212\,\mu\mathrm{m}$ as well as

$$\begin{aligned}\Delta t_{330} &= \frac{t_{min} - t_{max}}{\lambda(t_{min}) - \lambda(t_{max})} \cdot \lambda + t_{max} - \frac{t_{min} - t_{max}}{\lambda(t_{min}) - \lambda(t_{max})} \cdot \lambda(t_{max}) && (5.2.12)\\ &= 0.0259\frac{\mathrm{ps}}{\mathrm{nm}} \cdot \lambda + 4.937\mathrm{ps} - 0.0259\frac{\mathrm{ps}}{\mathrm{nm}} \cdot 813.3\,\mathrm{nm} && (5.2.13)\end{aligned}$$

for the PPLN with a poling period of $\Lambda = 330\,\mu\mathrm{m}$, where $\lambda(t_{min})$ is the center wavelength of the "dip" at the lowest delay and $\lambda(t_{max})$ is the center wavelength of the "dip" at the highest delay. The difference in the effective GDD of the laser pulses is therefore

$$\begin{aligned}\Delta\phi_{2,l} &= \left|\frac{\Delta t}{\Delta\lambda}\frac{-\lambda^2}{2\pi c}\right| && (5.2.14)\\ &= \left|0.0431\frac{\mathrm{ps}}{\mathrm{nm}}\frac{-\lambda^2}{2\pi c}\right| = 14650\mathrm{fs}^2 \qquad \text{for } 212\,\mu\mathrm{m} && (5.2.15)\\ &= \left|0.0259\frac{\mathrm{ps}}{\mathrm{nm}}\frac{-\lambda^2}{2\pi c}\right| = 8800\mathrm{fs}^2 \qquad \text{for } 330\,\mu\mathrm{m} && (5.2.16)\end{aligned}$$

introduced by the TOD in the initial pulses when they are delayed by a time delay $\Delta t = 2\pi\nu\phi_{2,l}$ with the corresponding frequency of $\nu = 0.545\,\mathrm{THz}$ or $\nu = 0.36\,\mathrm{THz}$ of the two PPLNs.

The mismatch in the GDD affects the chirp-and-delay concept as it is depending on the chirp rate $(1/\phi_{2,l})$. The calculation neglects the higher order effects as they are not as dominant as the GDD introduced by the TOD. The experiment to circumvent this mismatch will be explained and discussed in section 5.4.

5.2.2. Effects of the lower energy pulses in the pulse-train

In section 5.1 a 38% partial reflector and a high reflector is used to generate a pulse train with two pulses of equal energy followed by lower energy pulses. Due to the pulse train no energy is lost while generating the two main pulses. The additional pulses in combination with the TOD modify the electric field of the IR input due to the small pulse delay compared to the pulse duration and the different arrival time of the frequencies. For a pulse without TOD the generated THz pulses coherently add.

Figure 5.9 shows a schematic Wigner plot of such a pulse train. The variation of the frequency content results from the TOD in the pulse. At a delay Δt_1 the two main pulses are phase-matched in the PPLN for a frequency Ω. Furthermore the other pulses are generating the same frequency content. All generated THz pulses therefore add coherently

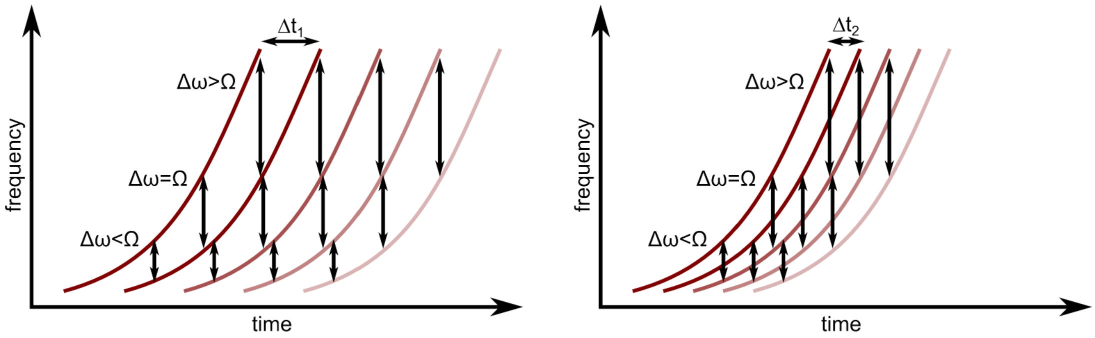

Figure 5.9.: Schematic Wigner-plot of a pulse train with two equally loaded pulses followed by several lower energy pulses generated by a broadband pulses with TOD. **Left:** At a time delay Δt_1 the two main pulses are phase-matched for a frequency Ω. Due to the TOD the frequency difference $\Delta\omega$ varies over the full pulse. The lower energy pulses add coherently to the process. **Right:** At the time delay $\Delta t_2 = \frac{1}{2}\Delta t_1$ every second pulse generates the nessessary frequency content.

to the two first pulses. Evidence is achieved that it is also possible to generate THz at half of the delay $\Delta t_2 = \frac{1}{2}\Delta t_1$. There the first and the third pulse overlap in the crystal and allow phase-matching in the PPLN.

To simplify the experiment, a Mach-Zehnder interferometer is built to generate two isolated pulses, which will be described in section 5.3 in detail.

5.2.3. Total internal reflection

Due to the high refractive index of lithium niobate in the low frequency range of $n_{\mathrm{THz}} \sim 5$ the critical angle for total internal reflection θ_c is just

$$\theta_c = \arcsin\left(\frac{1}{n_{\mathrm{THz}}}\right) = 11.5^\circ. \tag{5.2.17}$$

Therefore the alignment of the IR pump pulses into the PPLN has to be precise to couple the THz out of the PPLN. A misalignment of the two optical IR beams of just 0.6 mrad leads to total internal reflection of the generated THz beam. A slight detuning of the two pump pulse leads to an angled out-coupling at the PPLN which should be controlled for proper application and characterization of the THz radiation.

As the crystal is used without AR-coating back reflections of the input surface have to be considered. The crystal is slightly rotated by approximate 1° to eliminate the back

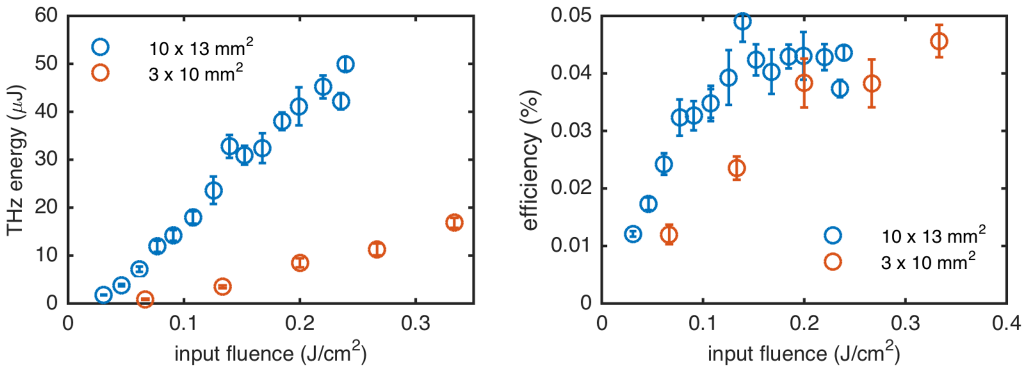

Figure 5.10.: Left: THz pulse energy of the large aperture crystal vs. the input fluence for a elliptical 3x10 mm^2 and a elliptical 13x10 mm^2 pump beam. **Right:** Corresponding internal conversion efficiency.

reflections to the optical axes of the laser, a further challenge for the alignment of the IR pump pulses.

5.2.4. Energy scaling of large aperture crystal

The part of the ANGUS laser system used for the chirp-and-delay experiments is capable to supply high energies up to 1.2 J. The crystal size of 3x10 mm^2 limits the pump energy which can be applied to the crystal to a maximum of 0.225 J assuming the measured damage threshold of 750 mJ/cm^2. The full potential of the laser system could not be explored for crystals of this size. The large aperture crystals with a clear aperture of 10x15 mm^2 manufactured by Prof. Taira and Dr. Ishizuki (see section 3.3.1) allows us to generate higher energy THz pulses and and is the largest crystal available.

This crystal offers the opportunity to check the scalability of the chirp and delay concept. The THz energy is measured for a pump pulse with the 3x10 mm^2 beam size as well as with the full beam of the laser which has a beam size of 10x13 mm^2 (figure 5.10 left). The energy increases by a factor of 3.6 and reaches an energy of $E_{\mathrm{THz}} = 50\,\mu\mathrm{J}$ for the full beam compared to an energy of $E_{\mathrm{THz}} = 17\,\mu\mathrm{J}$ for the small rectangular beam. The maximal conversion efficiency was the same for both cases at around $\eta = 0.045\%$. It has to be mentioned that the efficiency is lower than the maximal efficiency of the measurements in section 5.1, which is due to the frequency scaling of the efficiency by Ω^2. For a crystal phase-matched for a frequency of 0.545 THz an efficiency of

$$\eta_2 = \frac{\Lambda_1^2}{\Lambda_2^2} \cdot \eta_1 = 2.42 \cdot 0.045\% = 0.11\% \tag{5.2.18}$$

can be estimated, where $\Lambda_1 = 0.33\,\mathrm{mm}$ and $\Lambda_2 = 0.212\,\mathrm{mm}$ the poling period to the phase-matched frequencies, respectivly. This scaling only provides a rough estimation of the frequency scaling, since other influences on the efficiency as for example the absorption as well as the refractive index itself are neglegted.

With these advantages of the larger crystal aperture only the large aperture crystal is used in further experiments.

5.2.5. Summary of chirp-and-delay with pulse-train

The chirp-and-delay setup with a pulse train allows to generate high energy pulses up to 40 µJ with an efficiency of up to $\eta = 0.13\%$ at a frequency of 0.545 THz. The effects of the third order dispersion as well as the pulse-train itself limit the usable pump spectrum and thus the generation of the THz pulses. By applying two pulses and controlling the effect of the TOD the limitations are circumvented.

5.3. Generation of THz pulses via chirp-and-delay in a Mach-Zehnder interferometer

To study the chirp-and-delay concept the simplest case with two identical pulses is exploited. As described in section 5.2 a pulse-train setup is well suited to transport more energy, but the lower energy pulses of the pulse train in combination with the higher order dispersion of the pump pulse result in undesired effects leading to a lower conversion efficiency. To overcome this problem a Mach-Zehnder setup is introduced to generate two identical pulses (figure 5.11). The high energy laser pulse of the ANGUS laser is split with a 50/50 beam splitter into two arms. One arm has a motorized delay stage to fine-tune the delay between the two generated pulses. With a careful alignment it is possible to overlap the two pulses again at a 50/50 beam splitter to ensure a collinear pumping geometry. The Mach-Zehnder interferometer generates two outputs where one is temporarily blocked, which can be neglected or may be used for a second THz generation setup. At the beam splitter the transmitted pulse experiences material dispersion in the fused silica substrate. To compensate for these dispersion the setup is built in the way that the second beam splitter transmits the arm which is reflected at the first beam splitter to ensure the same dispersion on both arms as well as the same energy in both pulses. The wave-plate before the PPLN crystal allows fine tuning of the polarization to match the optical axes of the PPLN.

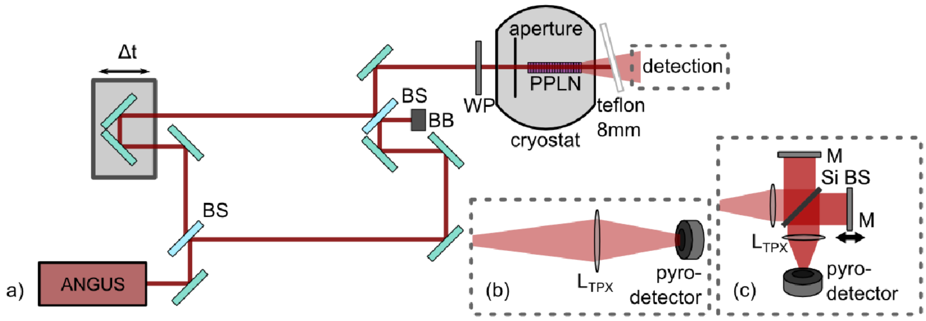

Figure 5.11.: a) Mach-Zehnder setup to generate a chirped pulse pair with a time delay Δt. **b)** THz pulse energy measurement setup with one TPX lens (L_{TPX}). **c)** THz frequency measurement setup based on Michelson interferometer. **KEY:** BS: 50 % beam splitter; BB: beam block; WP: wave plate; M: Silver mirror; Si BS: silicon beam splitter.

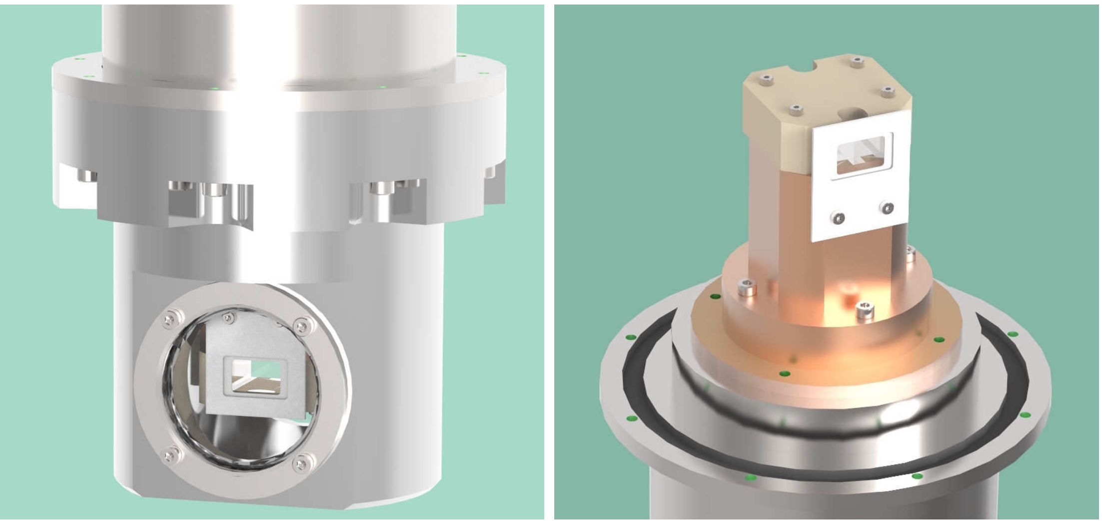

Figure 5.12.: Left: Input window of vacuum chamber for cryogenic cooling of the large aperture PPLN. The symmetric cold finger allows crystals up to a size of 4 cm. **Right:** Cold finger of the 3.6 cm long large aperture PPLN with the ceramic mask at the input surface.

For generating the multi-cycle THz pulses a large aperture PPLN with a poling period of $\Lambda = 330\,\mu\text{m}$ mounted in the cryogenic dewar is pumped with a beam diameter of 13 mm $1/e^2$-beam diameter. A mask with a size of 9.5 x 14.5 mm^2 protects the cold finger from residual pump light exceeding the crystal size (figure 5.12). This results in a pump beam area of $A = 1.3\,\text{cm}^2$. The pump beam is dumped on a 11 mm thick Teflon plate. To detect the energy of the generated THz pulse the beam is focused onto the pyro detector with a single TPX lens ($f = 100\,\text{mm}$) placed 240 mm behind the exit surface of the crystal. The frequency of the THz is measured with the Michelson interferometer (see section 3.5.4).

Finding time zero t_0 of the Mach-Zehnder interferometer is important to determine the time delay between the two pulses. In figure 5.13 the waterfall plot of the measured optical spectra around the zero delay is shown. The interference pattern of the pump pulses is obvious. At time zero the arrival time for the two pulses is the same for a given frequency content. The measurement of time zero confirms that the pulse arrive at the same point in time and space. This fine alignment has to be conducted for the whole range of the translation stage to ensure the collinear pumping geometry.

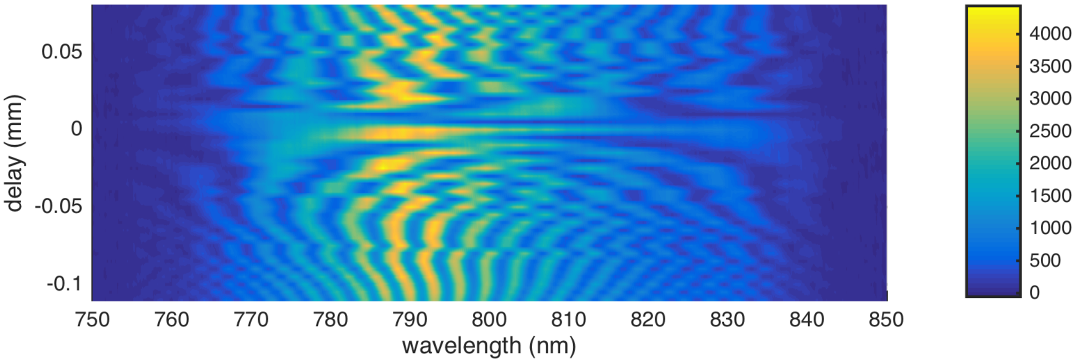

Figure 5.13.: Interference pattern in the optical spectra for different delays of the two pulses to each other.

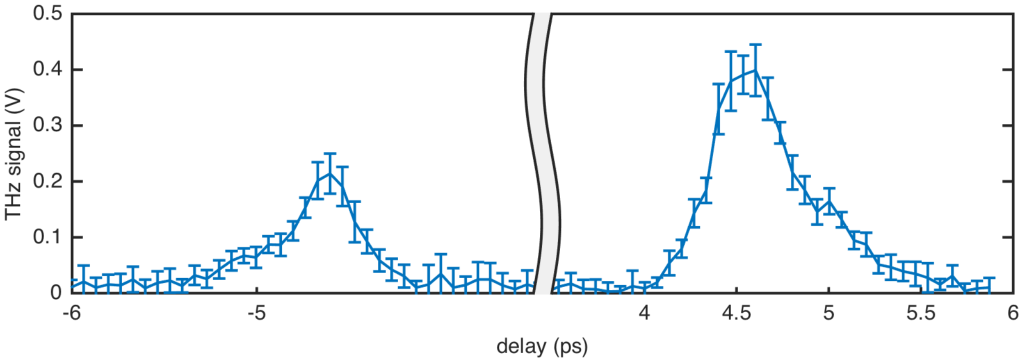

Figure 5.14.: Delay behavior of the Mach Zehnder setup. The optimal time delay is $\Delta t_{\text{opt}} = \pm 4.6\,\text{ps}$ corresponding to a group delay $\phi_2 = 2.03\text{ps}^2$.

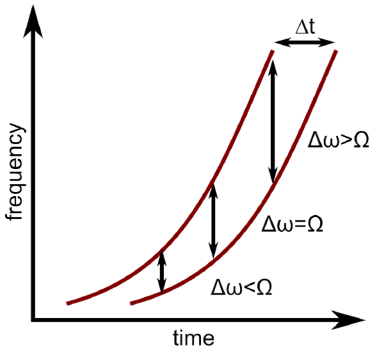

Figure 5.15: Wigner-plot to illustrate the chirp-and-delay concept at the Mach Zehnder setup. TOD results in a nonlinear frequency-vs.-time behavior.

The delay between the two pump pulses is scanned to find the optimal time delay Δt_{opt} for the chirp-and-delay concept. The optimal time delay Δt_{opt} can be calculated via

$$\Delta t_{opt} = 2\pi\nu\,\phi_2, \tag{5.3.1}$$

where ϕ_2 is the GDD of the pump pulses and ν the generated frequency of the THz pulse. In figure 5.14 the dependence of the generated THz signal on the delay between the two pulses for the positive and the negative delay is presented. The optimal delays are $\Delta t_{\pm\mathrm{opt}} = \pm\,4.6\,\mathrm{ps}$ corresponding to a GDD of $\phi_2 = 2.03\mathrm{ps}^2$. The stretcher of the laser produces a GDD of $\phi_2 = 2.3\mathrm{ps}^2$ but due to the 6 mm BS and other optical materials in the IR beam path the GDD is reduced.

In the ideal case the THz signal should be just generated at the optimal delay with a narrow linewidth. Due to the higher orders dispersion in the beam and the unequal distributed energy the delay sweep as seen in figure 5.14 has a broader spread. Figure 5.15 shows the Wigner plot of the two pulse case with higher order dispersion. At the optimal delay, more than just the corresponding THz frequency is covered by the difference frequency content. Therefore by tuning the delay different parts of the pump - frequency spectrum are used to generate the THz as already described in section 5.2.

One has to bear in mind that the optical spectrum of the driver laser has less energy at the red part than at the blue part. Therefore, if the delay of the two pulses increases, the higher energy parts are generating first the THz pulse and then it travels to the lower energy part of the spectra. The trace of the delay scan looks similar to the optical spectra. The negative delay (see figure 5.14) is less efficient than the positive delay which is not yet fully understood. It is either a combination of higher order dispersion and the energy distribution effecting the difference frequency content or it is simply an alignment uncertainty.

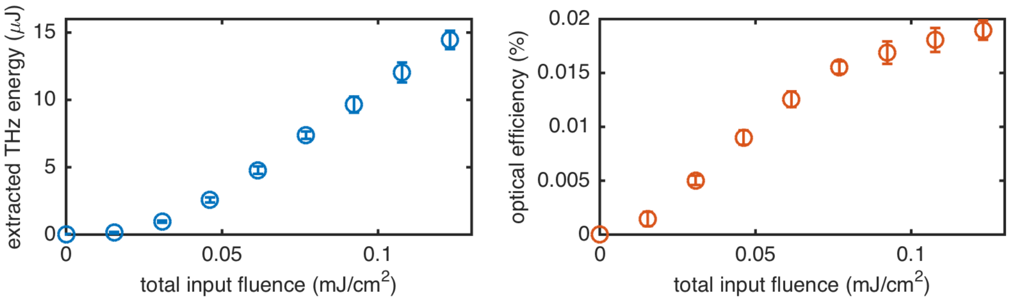

Figure 5.16.: Left: Extracted THz energy vs. input fluence. **Right:** conversion efficiency vs. input fluence

Figure 5.16 shows the dependence of THz energy on the input fluence at the optimal delay, keeping the beam size the same and varying the input energy. The energy increases as expected quadratically at low fluences and at higher fluence linearly (figure 5.16 left) confirming the nonlinear behavior and the saturation of the conversion efficiency. With this chirp-and-delay setup an extracted THz energy of 14.45 µJ is achieved. The internal conversion efficiency as shown in figure 5.16 right reaches a maximal efficiency of 0.02%. The maximal pump fluence is limited to $F = 0.123\,\mathrm{J/cm^2}$ to avoid the risk of damaging the crystal or other optics in the beam path. At this fluence an energy of $E = 159\,\mathrm{mJ}$ at the crystal is required for the beam size. As we loose 50% of the energy in the Mach-Zehnder configuration the ANGUS is pumped with two pump lasers to reach the necessary pump energy of $E \approx 0.32\,\mathrm{J}$. To go to higher fluences, the last pump laser for the ANGUS laser is available, which provides directly an energy of $E \approx 1.2\,\mathrm{J}$. The risk of damaging either the crystal or the optics on the way are too high at this point of measurements. We switch to the more promising measurements with the chirp compensation which are explained in the following section 5.4.

Besides the energy of the THz pulse the frequency content of the pulse is important to confirm the narrowness and the frequency of the pulse. Due to the relative high energy of the pulse it is possible to measure the frequency with the Michelson interferometer (see section 3.5.4). In figure 5.17 (left) the interferometric trace of the THz pulse generated by the Mach-Zehnder setup is depicted. If both THz pulses which are generated by the Si-BS are not overlapping and interfere the energy of a single THz pulse is detected with an THz signal of 0.2 V corresponding to an energy of $E_{\mathrm{THz}} \approx 0.32\,\mu\mathrm{J}$. As the two pulses are overlapping the interference pattern occurs and the pulse duration can be

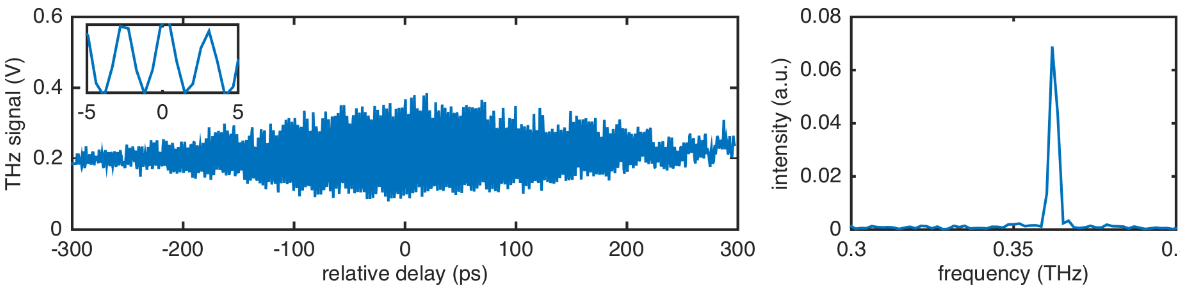

Figure 5.17.: Left: Interferometer trace over 600 ps. **Inset:** Zoom around the t_0 to show the period of the interferometric trace $T = 2.75\,\mathrm{ps}$. **Right:** Spectral amplitude of THz pulse generated by the the Mach-Zehnder setup.

estimated assuming no spectral phase on the THz pulse. The envelope of the interference pattern has a FWHM of $\tau_i = 200\,\mathrm{ps}$. Therefore the THz pulse has a pulse duration of $\tau = \sqrt{2}\cdot\tau_i = 283\,\mathrm{ps}$ matching the estimated pulse duration calculated by the convolution of the pulse durations

$$\tau = \sqrt{\tau_c^2 + \tau_l^2} \tag{5.3.2}$$

resulting from the effective crystal length ($\tau_c = 148\,\mathrm{ps}$) and the laser ($\tau_l = 240\,\mathrm{ps}$).

The spectral content of the THz pulse can be calculated by an FFT of the interferometric trace as seen in figure 5.17 (right). The THz pulse has a center frequency of 0.361 THz as expected. The bandwidth of the pulse is 3.4 GHz which matches to the expected value of

$$\Delta\Omega = \frac{\Omega}{N} = \frac{0.36\,\mathrm{THz}}{109} = 3.3\,\mathrm{GHz}. \tag{5.3.3}$$

This bandwidth as well as the interferometric trace confirm that narrowband THz pulses are generated. Knowing the pulse duration of the THz pulse as well as the energy of the pulse the THz peak field can be estimated via

$$E = \sqrt{\frac{2I}{c\epsilon_0}} \qquad \text{with} \quad I = \frac{E_p}{A\tau} \tag{5.3.4}$$

by using the diffraction limited spot size $w_0 = 0.53\,\mathrm{mm}$ (see section 3.2). Therefore the intensity and the electric field is

$$I = 60\,\mathrm{GW/m^2} \qquad \text{and} \quad \epsilon = 6.7\,\mathrm{MV/m}, \tag{5.3.5}$$

if the THz pulse can be focused down to the diffraction limited spot size. Using a spot size of $w_0 = 4.5\,\mathrm{mm}$, which is the spot size at detector, the intensity and the electic field is reduced to

$$I = 0.8\,\mathrm{GW/m^2} \qquad \text{and} \quad \epsilon = 0.83\,\mathrm{MV/m}. \tag{5.3.6}$$

Therefore either more energy or an improved beam propagation has to be used for further experiments which need high electric fields like for example electron acceleration in a waveguide.

The measurements at the Mach-Zehnder setup confirm that the chirp-and-delay pumping concept produces narrowband THz high energy THz pulses. The mismatch of the chirp rate due to higher order dispersions via introducing dispersion on just one arm of the interferometer is well taken. Steps to control this mismatch will be explained and discussed in the next section.

5.4. Experimental compensation of phase-mismatch due to third order dispersion: Asymmetric chirp concept

The driving pulse for the difference frequency generation comes along with higher order dispersion as the chirped pulses are generated by an Öffner strecher (see section 3.3.2). This results as depicted in figure 5.18 (left) in a broader difference frequency content in the overlapped pulses than the PPLN can cover. The mismatch identified in section 5.2 on the pulse train measurements and measured in section 5.3 with the Mach-Zehnder setup leads to the assumption that the full optical spectra should be phase-matched to reach higher efficient generation. We developed the concept to flatten the difference between the instantaneus frequency of the two pulses to allow phase-matching over a broader part of the optical pump spectrum. To compensate for the additional GDD resulting from the higher orders (see section 5.2) *N. H. Matlis* suggested to add material dispersion to one of the pump pulses. The expectation for this setup are depicted in figure 5.18 (middle and right). The additional GDD on one of the pulses leads to a tilt of the curve representing the time-frequency relationship. Adding dispersive material into one of the pulses is named as the "asymmetric chirp concept", which will be discussed in this section.

In the chirp concept both pulses have the same spectral content but different phases. Dispersion within the propagation medium are regarded as comparable. In the asymmetric chirp concept additional dispersion is added by dispersive medium in one of the arms leading to a different GDD in one of the pulses. Therefore one carefully has to consider on which pulse the additional dispersion is added and if it is positive or negative dispersion. As most of the optical materials have a normal dispersion (positive), further discussions focus on this case.

Adding GDD on the second pulse will slightly compress the pulse. Hereby, the difference frequency content will be flattened as depicted in figure 5.18 (middle). The difference frequency of the optical pulses remains close to the phase matched THz frequency for a broader part of the spectra. However, there is the risk to add GDD on the wrong pulse which is contra-productive and the possible usable part of the spectrum is stronger reduced than without additional GDD (figure 5.18 right).

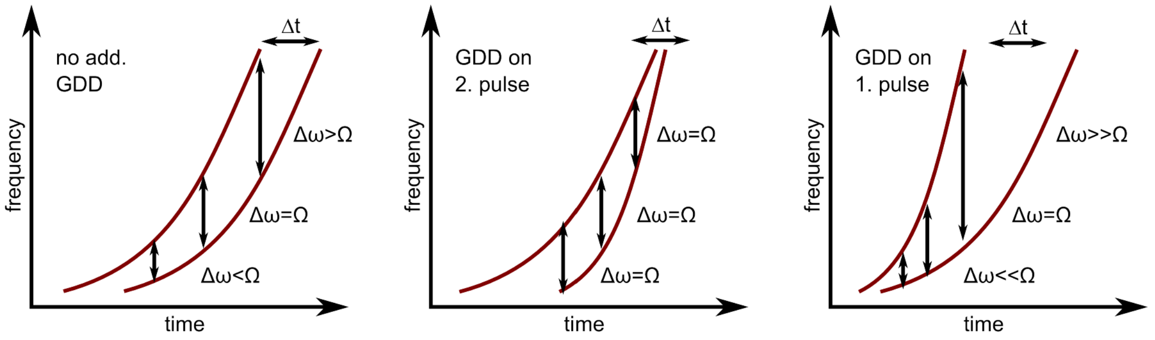

Figure 5.18.: Wigner-plot to illustrate the asymmetric chirp concept to compensate the phase-mismatch due to higher order dispersion. **Left:** two pulses without additional GDD. The possible frequency content is broader than the phase-matched frequency of the PPLN. **Middle:** Compensated TOD, the second pulse experience stronger GDD than the first. The frequency content matches the QPM frequency. **Right:** Only the first pulse is subject to the additional GDD. The frequency content deteriorates through compensation.

Every optical material introduces material dispersion to the optical pulse. The main parameters GD (group delay), GDD (group delay dispersion) TOD (third order dispersion) and even higher order dispersion follow from the Taylor expansion of the spectral phase $\phi(\omega)$ of the optical pulse. They can be calculated via

$$\phi_1 = \frac{d\phi}{d\lambda} = \frac{1}{c}\left(n - \lambda\frac{dn}{d\lambda}\right)\cdot d \qquad \text{(GD)}, \tag{5.4.1}$$

$$\phi_2 = \frac{d^2\phi}{d\lambda^2} = \frac{\lambda^3}{2\pi c^2}\frac{d^2n}{d\lambda^2}\cdot d \qquad \text{(GDD)}, \tag{5.4.2}$$

$$\phi_3 = \frac{d^3\phi}{d\lambda^3} = -\frac{\lambda^4}{4\pi^2c^3}\left(3\frac{d^2n}{d\lambda^2} - \lambda\frac{d^3n}{d\lambda^3}\right)\cdot d \qquad \text{(TOD)}, \tag{5.4.3}$$

which is discussed in details for example by M. Hemmer [Hem11] in the analysis of a prism compressor. For the additional GDD needed in the asymmetric chirp concept a dense flint glass (SF11) is chosen. Table 5.1 summarizes the material dispersion of SF11 at 800 nm calculated with the Sellmeier equation of SF11 [SCH15]

$$n^2 - 1 = \frac{1.73759695\lambda^2}{\lambda^2 - 0.013188707} + \frac{0.313747346\lambda^2}{\lambda^2 - 0.0623068142} + \frac{1.89878101\lambda^2}{\lambda^2 - 155.23629}. \tag{5.4.4}$$

Therefore each additional mm of SF11 adds GDD of $\phi_2 = 187.5\,\text{fs}^2$ to the pulse. The GDD and TOD of the laser pulses from the ANGUS laser system are defined by the

n	λ	$\frac{dn}{d\lambda}(\mu m^{-1})$	$\frac{d^2n}{d\lambda^2}(\mu m^{-2})$	$\frac{d^3n}{d\lambda^3}(\mu m^{-3})$	ϕ_1 (ps/mm)	ϕ_2 (fs^2/mm)	ϕ_3 (fs^3/mm)
1.7646	0.8	-0.05859	0.2068	-1.1780	6.0425	187.5	-123.99

Table 5.1.: Optical properties of SF11 calculated from the Sellmeier equation 5.4.4

stretcher before the pre-amplifier to be $\phi_{2,l} = 2.3 \cdot 10^6\,\mathrm{fs}^2$ and $\phi_{3,l} = -4.4 \cdot 10^6\,\mathrm{fs}^3$. This additional TOD results in a GDD difference if the two pulses are delayed for the desired frequency $\nu = 0.36\,\mathrm{THz}$. The difference for the GDD is $\Delta\phi_{2,l} = 8800\,\mathrm{fs}^2$ as calculated in section 5.2.1. Adding SF11 material on one arm should match this difference. Therefore the optimal length of SF11 is

$$\frac{\Delta\phi_{2,l}}{\phi_{(2,\mathrm{SF11})}} = 46.9\,mm. \tag{5.4.5}$$

Just for completness, using a crystal phase-matched for 0.545 THz the GDD difference would be $\Delta\phi_{2,l} = 14653\,\mathrm{fs}^2$ which could be compensated by a prism with a length of 78.15 mm. The experiment with the additional SF11 is discussed in the next subsections.

5.4.1. Experimental setup

The experimental setup of the asymmetric chirp concept is the experimental setup of the Mach-Zehnder extended with two SF11 Brewster prisms as seen in figure 5.19. The SF11 prisms have a side length of 50 mm and an apex angle of 59°. SF11, a dense flint glass, has an refractive index of 1.76 [SCH15] therefore the Brewster angle is 60.5° perfectly matching the dimensions of the SF11 prisms and very little energy is lost due to reflections. The length of the optical path through the prism can be calculated via the triangle spanned by the input and the output surface of the first prism as well as the apex angle of the prism. For a perfect overlap of the prisms the length of SF11 is 49.2 mm. By shifting the second prism relative to the virtual output surface of the first prism the length and therefore the utilized material thickness can be varied to adjust the material GDD. The remaining experimental setup is unchanged to the Mach-Zehnder setup especially the THz setup and the detection as well as the PPLN crystal.

To proof the collinear pumping geometry and the arrival time of the pump pulses the zero delay of the setup has been measured. Due to the SF11 in the path way and the resulting group delay of the one pulse, the zero point is expected much later than

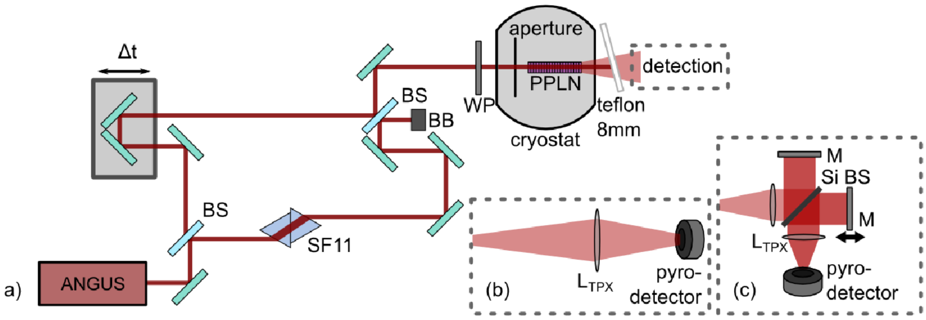

Figure 5.19.: a) Mach-Zehnder setup for asymmetric chirp compensation to generate a asymmetric chirped pulse pair with a time delay Δt. **b)** THz pulse energy measurement setup with one TPX lens (L_{TPX}). **c)** THz frequency measurement setup based on Michelson interferometer. **KEY:** BS: 50 % beam splitter (BS); BB: beam block; SF11: prism pair of SF11; WP: wave plate; M: Silver mirror; Si BS: silicon beam splitter.

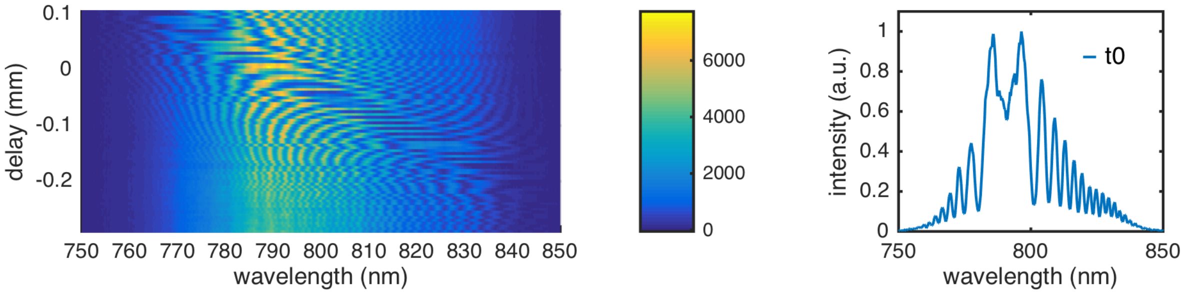

Figure 5.20.: Left: Interference pattern in the optical spectra for different delays of the two pulses to each other. **Right:** Optical spectra the chosen zero delay defined as t_0.

with the Mach-Zehnder setup. A complication in this case is that the two pulses do not have the same chirp rate. Therefore the "time zero" travels through the pulse as seen in figure 5.20. From the earlier chirp-and-delay measurements the part of the optical spectrum generating THz pulses most efficiently is known to be in the range of $\lambda = 790\,\mathrm{nm}$. The zero delay is set to that value as seen in 5.20 (right). These results confirm our expectation. Furthermore, the chirp difference is also visible in the optical spectrum. Just at a wavelength of $\lambda = 790\,\mathrm{nm}$ no interference occur, for higher frequencies as well for lower frequencies the fringe density in the interference pattern increases more and more.

5.4.2. Efficiency increase due to asymmetric chirp

To judge about the efficiency a delay scan with the Mach-Zehnder and with the asymmetric chirp concept (Figure 5.21 (top)) are compared. The THz signal in the case of the asymmetric chirp concept increases at the positive delay of $\delta t = 0.69\,\mathrm{mm}$ by a factor of 5.15 compared to the THz signal generated by two equal pulses for a pump fluence of $0.03\,\mathrm{J/cm^2}$. Furthermore, the delay behavior has a smaller spread confirming that a broader part of the pulse is phase-matched for the PPLN. The width of the delay scan for the compensated case is just 30% of the uncompensated case.

THz generation was measured for both, positive and negative delays. At the negative delay we could confirm that the asymmetric chirp concept works as expected. The phase matched frequency content is reduced and therefore the delay is much wider and less efficient which can be seen in figure 5.21 (top). The width of the delay scan with the SF11 is doubled compared to the scan without the SF11.

At the positive delay the THz energy was measured. In figure 5.21 the comparison of measured THz energy for the two cases of two pulses with the same dispersion and two pulses where one has additional dispersion from the SF11. The maximal energy is increased by a factor of 6 from $13\,\mu\mathrm{J}$ to $78\,\mu\mathrm{J}$ at an input fluence of $0.12\,\mathrm{J/cm^2}$. The conversion efficiency increases to 0.15% which is already a promising result compared to the uncorrected case ($\eta = 0.02\%$). It has to be mentioned that at this point the material thickness was not optimized. Therefore we investigated how the energy can be further improved by optimizing the path length through the SF11.

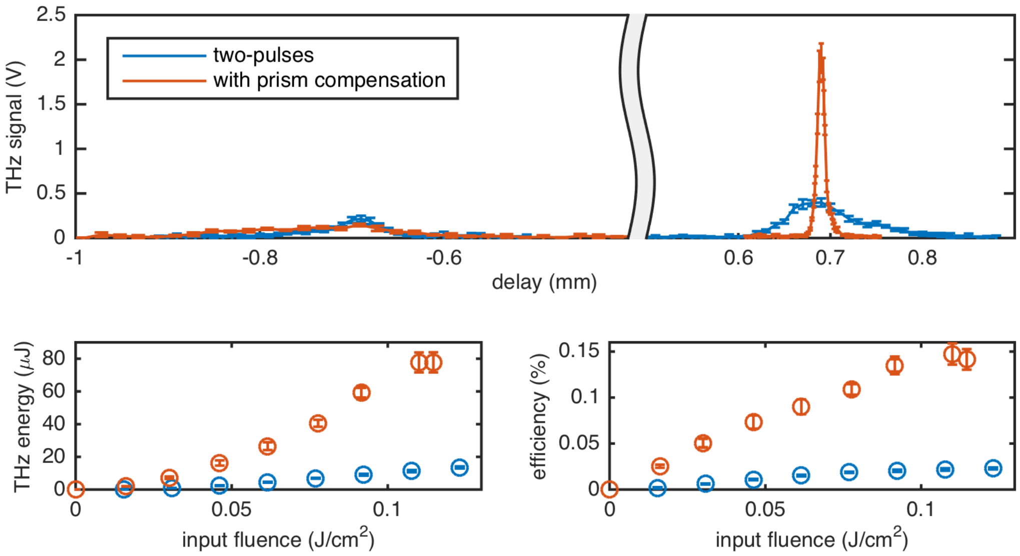

Figure 5.21.: Top: Comparison of the delay behavior of two equal pulses and two pulses with asymmetric chirp. **Bottom left:** THz energy (µJ) at the optimal positive delay of two equal pulses with TOD and two pulses with asymmetric chirp for increasing input fluence (J/cm^2). **Bottom right:** Corresponding conversion efficiency (%) of the THz pulse versus the IR input fluence (J/cm^2).

Figure 5.22 shows the delay behavior for different path length through the SF11 prism pair. The thickness was tuned by shifting the second SF11 prism parallel to the contacting surfaces. Table 5.2 gives an overview of the group delay (GD), the group delay dispersion (GDD) and the third order dispersion (TOD) of SF11 for different thicknesses (d). The corresponding delay behavior is depicted in figure 5.22. By increasing the length of SF11 the peak shows smaller spread and higher peak-height until the maximum is reached at a length of $d = 50.2\,\mathrm{mm}$. Afterwards the GDD of the SF11 greater than the GDD mismatch $\Delta_{2,l}$ due to the TOD of the laser and the curve of the delay behavior is getting broader and the generated THz signal is decreasing. Figure 5.22 (right) shows the maximal generated THz signal for the different lengths of SF11. Around the optimal length of SF11 the energy remains unchanged and varies just slightly. The depicted fitting function was done by *S. W. Jolly* with a numerical simulation of two gaussian beams with asymmetric chirp which will be presented in [Jol17]. The mismatch between the fitted function and the measured THz signal for longer SF11 as the maximum is ongoing research.

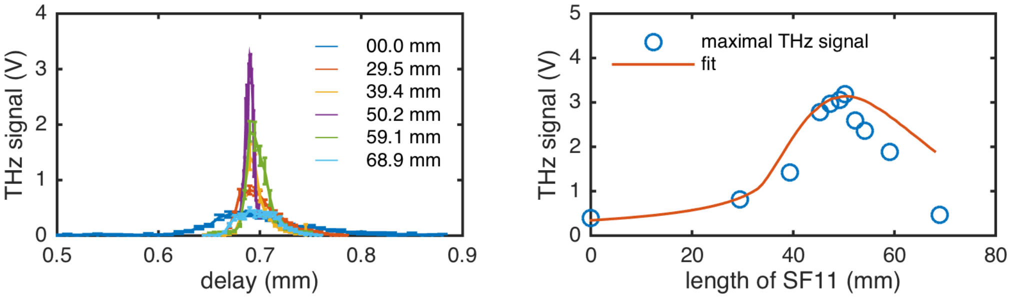

Figure 5.22.: Left: Delay behavior for different SF11 path length. **Right:** Maximal THz signal versus the length of SF11 (blue dots) and the simulated fit done by S. W. Jolly.

d	GD (ps)	GDD (fs^2)	TOD (fs^3)
29.5	178	5531	-3658
39.4	238	7388	-4885
50.2	303	9413	-6225
59.1	357	11081	-7328
68.9	416	12919	-8543

Table 5.2.: Additional group delay (GD), group delay dispersion (GDD) and third order dispersion (TOD) for different SF11 thicknesses (d).

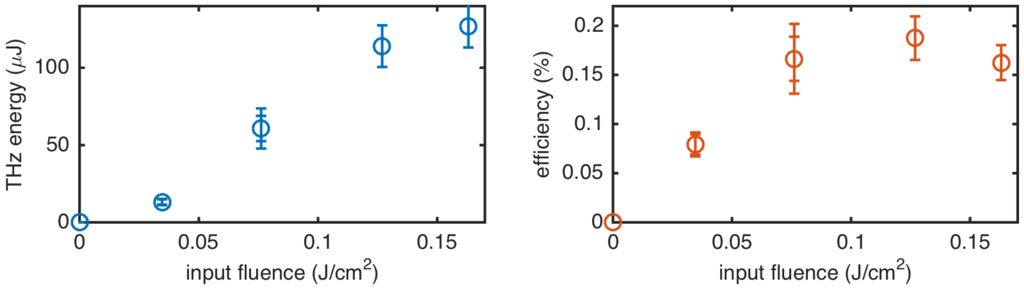

Figure 5.23.: Left:THz pulse energy at the optimal length of SF11. **Right:** Corresponding conversion efficiency.

SF11 is well suited to compensate the mismatch in GDD, but the opposite sign of the TOD results in additional TOD, which has to be compensated. The additional TOD at the optimal thickness is TOD $= 6225\,\mathrm{fs}^3$. A deeper analysis showed that the efficiency could increase by at least a factor of 2 if the TOD would be compensated, again an ongoing research.

In the experiment the optimal length of SF11 is determined to be $d_{\mathrm{opt}} = 50.2\,\mathrm{mm}$. The expected value calculated with the traveling "dip" is $d = 46.9\,\mathrm{mm}$. The error of 6.5% may come from different sources: either the uncertainty in the initial chirp of the laser, the unequal additional material dispersion at the two beam-splitters or more likely the uncertainty in which beam path was taken through the SF11. Furthermore, the uncertainty of the calculated dispersion mismatch seems rather high. The two prisms were aligned in such a way that the beam path is the length of the third side of the triangle, which is spanned by the input surface and the overlap between the two prisms as well as the apex angle. Already a slight unintended imprecision on the input angle influences the length of material. Therefore, the achieved result matches the predictions well.

At the optimal length of SF11 a energy scan was performed to determine the maximal THz energy as well as the conversion efficiency of this process (figure 5.23). The THz pulse has an energy of $E_{\mathrm{THz}} = 127\,\mathrm{\mu m}$. With a conversion efficiency of this process of $\eta = 0.187\%$ a new record in efficiency was achieved especially in this frequency range for multi-cycle THz pulses. Furthermore, the internal THz energy is $E = 227\,\mathrm{\mu J}$ and both energy are beyond the state of the art of narrowband terahertz radiation.

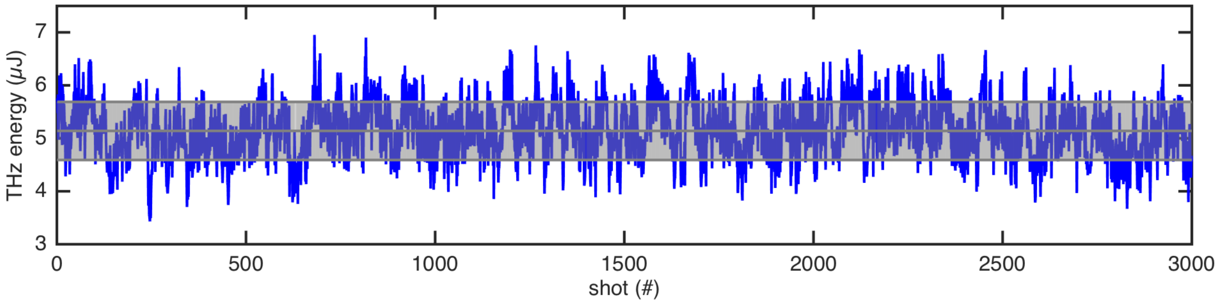

Figure 5.24.: Long term measurement of THz energy (blue) over 3000 shots. Grey area shows the average THz energy of $E_{\mathrm{THz}} = 5.14\,\mu\mathrm{J}$ and standard deviation of $\sigma = 0.55\,\mu\mathrm{J}$.

5.4.3. Long term energy measurements

To assure the reliability of the achieved improvements the long term stability of the generated THz energy was measured over 3000 shots in a time of more than 11 minutes (figure 5.24). The data aquisition (DAQ) tool was used to read out the THz energy. DAQ is capable to measure the THz energy every 230 ms, so that 6 of 7 shots were measured. The THz energy shows minor fluctuations and can be regarded as stable over the 3000 shots with an average energy of $E_{\mathrm{THz}} = 5.14\,\mu\mathrm{J}$. The standard deviation of the THz energy is $\sigma = 0.55\,\mu\mathrm{J}$ and corresponds to an RMS of 10.69%. To compare, the input energy of $E_{\mathrm{in}} = 34\,\mathrm{mJ}$ has already a RMS of 3.5%, which would lead to an error of 7% for the second order process. The THz error is slightly higher than the source error. Reason may reside in the DAQ or alignment of the setup. The DAQ has a relative high noise level, therefore the error of the THz signal should be higher than the laser fluctuations. As the RMS is only slightly higher than expected, major changes in the alignment that would decrease the THz signal significantly are unlikely. The long term measurement prove that the THz energy has no decrease over time for this energy level.

5.4.4. Frequency measurement via Michelson interferometer

To determine the optical spectra of the THz pulse an interferometric measurement with a Michelson interferometer (see section 3.5.4) was done. Figure 5.25 (left) shows the THz signal (V) versus the delay between the two at the silicon BS generated pulses with the zoom around the zero delay $t = 0$ (inset) showing the period of the interferometric trace as $T = 2.77\,\mathrm{ps}$. The THz signal of a single interferometer arm is around 0.4 V corresponding

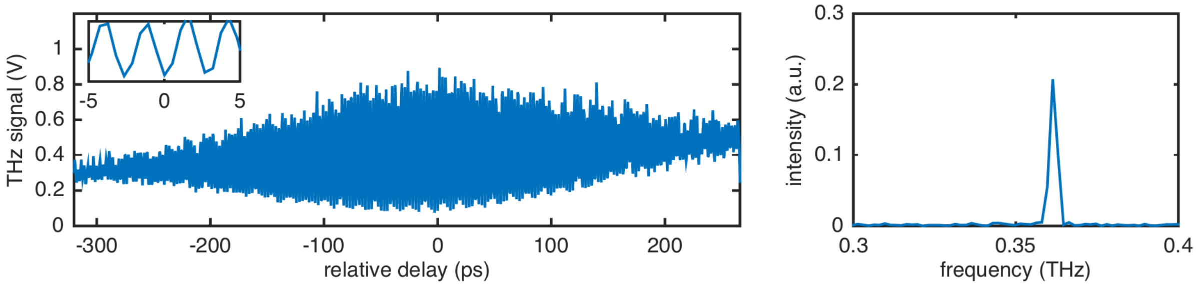

Figure 5.25.: Left: Interferometer trance over 600 ps. **Inset:** Zoom around the zero delay $t = 0$ to show the period of the interferometric trace $T = 2.77$ ps. **Right:** Spectral amplitude of THz pulse generated by the the Mach-Zehnder setup.

to an energy of $E_{\mathrm{THz}} \approx 0.364\,\mu\mathrm{J}$. At the destructive peaks the THz signal does not reach zero but remained at the noise on the detector.

The spectral amplitude is calculated via FFT of the trace of the interferometer (figure 5.25 (right)). The frequency of the PPLN with a poling period of $\Lambda = 330\,\mu\mathrm{m}$ is $\nu = 0.36\,\mathrm{THz}$ matching the expected value calculated via

$$\nu = \frac{c}{\Lambda\,\Delta n}. \tag{5.4.6}$$

The bandwidth of the spectra is 3.4 GHz well in agreement with the expected value of 3.3 GHz (see equ. 5.3.3).

Besides the frequency, the interferometer provides an estimate over the pulse duration. The FWHM of the envelope is $\tau_i = 200\,\mathrm{ps}$ and therefore the pulse duration of the THz pulse is $\tau = \sqrt{2} \cdot \tau_i = 283\,\mathrm{ps}$. Compared to the THz pulse generated by the Mach-Zehnder setup the pulse duration did not change significantly.

5.4.5. Measurement of the beam profile

The measurement of the beam profile of the terahertz beam is challenging due to the low sensitivity of the beam profile camera based on pyro detectors in combination with the low repetion rate of the laser. Therefore, a knife edge measurement was done to determine the lower bound of the beam size. The THz energy was measured while a beam block with a knife edge is propagating through the beam. In figure 5.26 the raw data of such a knife edge measurement is shown (blue line): for a distance smaller than ~5 mm the

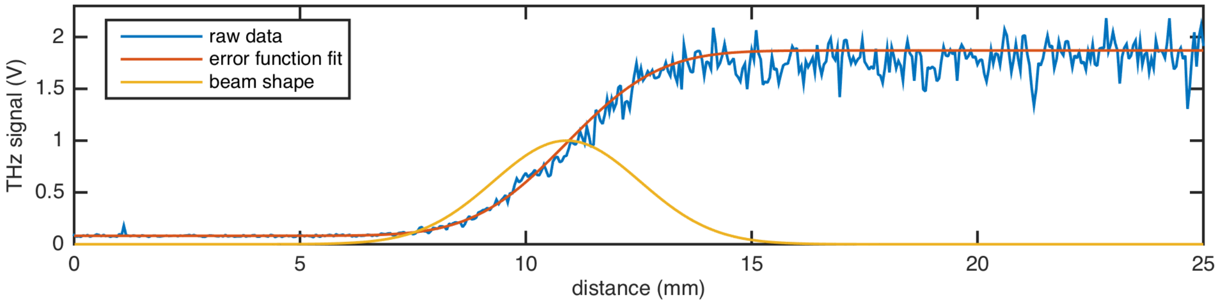

Figure 5.26.: Example for the knife edge measurement: The raw data (blue) is fitted with an error function (equ. 5.4.7, red). The derivation (yellow) determine the lower bound beam size.

full beam is blocked, for a distance greater than ~15 mm the full beam is detected. This shape of the curve can be fitted with an error function via

$$fit(x) = a \cdot \mathrm{erf}(b \cdot (x - x_0)) + c, \tag{5.4.7}$$

where a, b, c and x_0 have to be determined. In figure 5.26 such a error function is fitted accordingly to the raw data. The fit is necessary to compensate the higher noise for the unblocked case compared to the blocked case. The beam size is determined by the derivation of the fitted errorfunction (figure 5.26, yellow line). The FWHM beam size is in this example 3.81 mm. As mentioned before this is a lower bound for the beam size. The sensitivity of the detector does not allow to measure low power signals. Therefore, the low energy part of the error function may be lower and the beam size would increase. Despite these constraints this measurement offers a great opportunity to estimate the lower bound of the beam size. It provides the evidence that the beam is at least of this size.

To measure the beam propagation is important to confirm the collection of the beam as well as to proof the focusability. Therefore, the beam size is measured at different positions of the knife edge after the PPLN (z = 51 mm, 79 mm and 334 mm). The beam divergence can be estimated with the first two positions. At a distance of 231 mm the 2” TPX lens was placed to focus down the THz onto the detector placed at a position of z = 369.1 mm (see figure 5.19 b)). The last position (z = 334 mm) briefly before the detector confirms that the full THz pulse is on the detector. In figure 5.27 the beam line out at the three positions are shown with the FWHM beam size in the legend. The THz beam in the

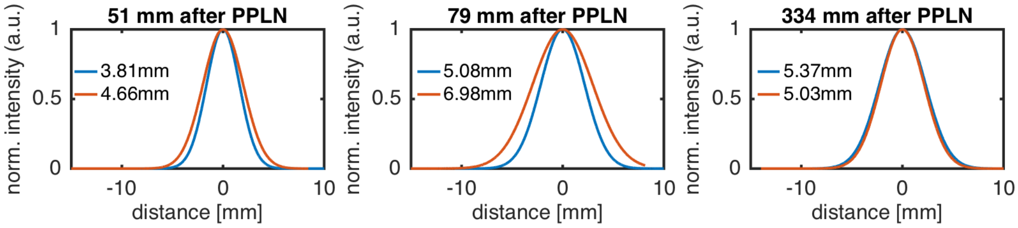

Figure 5.27.: Calculated beam size at three positions after the PPLN. The horizontal beam size (blue) is diverging less than the vertical beam size (red). Both can be focused to approximately the same size (right graphic). The legend indicates the FWHM beam size.

horizontal direction (blue) is smaller and diverges less than in the vertical direction (red). At the last position both beams have approximately the same beam size and a beam size smaller than the detector size, which allows an accurate detection. The estimated beam size at the lens position is smaller than the aperture of the lens. Therefore the full beam is collected.

Figure 5.28 shows for a reconstruction of the 2D beam profile based on the beam sizes measured via the knife edge measurement and the estimated gaussian beam propagation. For the gaussian beam a beam waist w_0 of 3.53 mm (red line, vertical beam) and 4.59 mm (blue line, horizontal beam) is assumed, which correspond to the $1/\sqrt{2}$ of the input beam waist of the IR pump beam (horizontal 6.5 mm, vertical 5 mm). The violet line at z = 231 mm is a guide to the eye for the lense position. The black box at the end represents the detector chip. The measured beam sizes are always slightly lower than expected, but the divergence and the height compared to each other are matching with the expected values.

To visualize the THz beam, the beam shape is calculated in 2D using the line outs of the knife edge measurement. In figure 5.29 the beam shape at the three measured positions is depicted. The beam is diverging as seen in the first two pictures: the beam is bigger at a position of z = 79 mm than at z = 51 mm. As mentioned before the lens at a position of z = 231 mm is refocusing the beam. The measurement at z = 334 mm – 35 mm before the detector chip – indicates that the full beam is captured at the detector with a chip size of 9 mm in diameter.

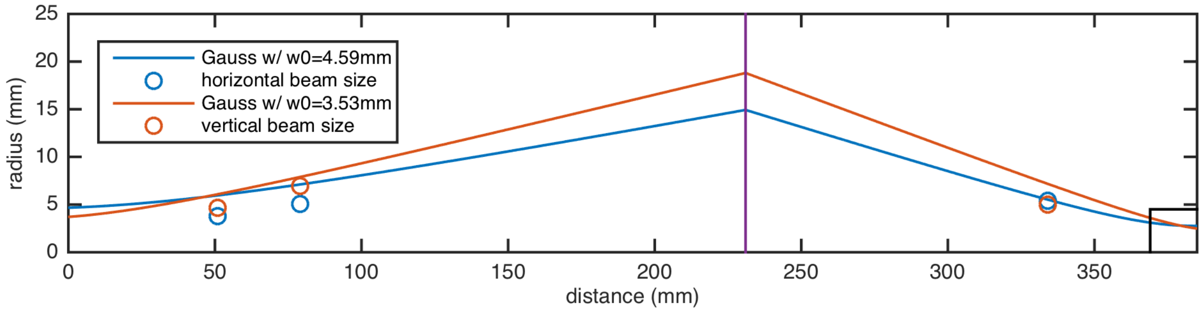

Figure 5.28.: Knife edge beam size at three positions after the PPLN. The horizontal beam size (blue dot) is diverging less than the vertical beam size (red dot) confirmed by the calculated gaussian beam propagation for a beam waist of $w_0 = 3.53\,\mathrm{mm}$ (red line) and $w_0 = 4.59\,\mathrm{mm}$ (blue line). The beam is focused with a lens (violet line) at z = 231 mm into the detector (black line).

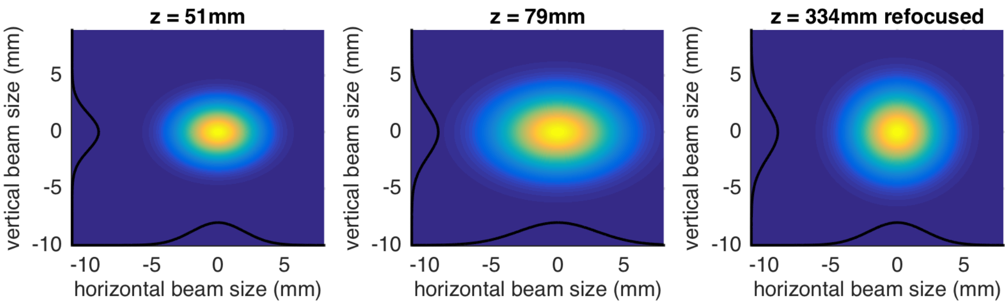

Figure 5.29.: Calculated THz beam shape at the two positions before a focusing lens (z = 231 mm) and one after refocusing. The normalized line outs (black) used for the calculation are drawn on the corresponding axes.

The calculated beam shape appears perfectly round which traces back the calculation itself. The line out is an integration over the full beam, the 2D beam shape appears more symmetric than it actually will be. Therefore the calculated 2D-beam shape is just for visualization.

5.4.6. Electric field of the generated pulse

Using the focused beam size as predicted from the gaussian beam propagation mentioned in the section 5.4.5 of $w_0 = 2.77\,\mathrm{mm}$ and the measured pulse duration of $\tau =$282 ps the THz pulse intensity and the electric field can be estimated as

$$I = 196\,\mathrm{GW/m^2} \qquad \text{and} \quad \epsilon = 12.2\,\mathrm{MV/m}. \tag{5.4.8}$$

Focusing these THz pulses to a smaller spot size would be necessary to reach higher fields. the electric field of $\epsilon = 19.6\,\mathrm{MV/m}$ at the diffraction limited spot size has not yet reached the limit for an efficient electron acceleration.

5.5. Summary and conclusion of the chirp-and-delay experiments

The chirp and delay technique is a promising method to generate high energy, narrowband THz pulses. Several experiments to reach the range of µJ-level pulse energies are demonstrated. Either a train of chirped pulses or two chirped pulses are used to generate the necessary frequency content via delaying them to each other to allow difference frequency generation in periodically poled lithium niobate. Higher order dispersion on the pump pulse leads to a mismatch of the frequency content over full spectral bandwidth of the driving pulses. First experiments to compensate this effect of the TOD are presented and discussed in detail.

Adding material dispersion on one of the pump pulses compensate the mismatch due to TOD. A record THz pulse energy of $E_{\mathrm{THz}} = 0.127\,\mathrm{mJ}$ was achieved. The corresponding conversion efficiency of $\eta = 0.187\%$ is also beyond state of the art. The generated pulse has a frequency of 0.36 THz, a pulse duration of at least 282 ps and an electric field of $\epsilon = 12.2\,\mathrm{MV/m}$.

To reach the goal of mJ-level pulses which are necessary for efficient electron acceleration this concept may be improved furthermore. The three key parameters for optimization are identified as

- AR coating of the crystal for IR and THz,
- further compensation of higher order dispersion on the driving pulse, and
- increase of pump fluence.

An AR coating for the IR on the crystal predicts an energy increase of 15%. The AR coating may also reduce the risk of back reflections into the laser system and therefore allow an even higher pump fluence. The experiments with the higher pump energy run at risk of damaging the crystal and have to be planned carefully. The deeper understanding of effects associated with such high energies are still under progress.

The large aperture crystal is meanwhile AR coated for 800 nm and first measurements are ongoing. Furthermore, an AR coating for the THz should allow an increase of the extracted THz pulse energy up to 45% depending on the quality of the AR coating. Based on the results of this thesis a quartz plate (refractive index of $n = 2.24 = \sqrt{n_{\mathrm{THz}}}$ with a thickness of around 100 µm ($\lambda/4n_{\mathrm{THz}}$)) was regarded as promissing as AR coating for THz with a frequency of 0.36 THz. First investigation with an similar AR coating were done at a single-cycle source and showed an improvement of at least 30%. The final measurements with the AR coating are beyond the scope of this thesis.

The analysis in the asymmetric chirp concept showed that additional GDD introduced by the SF11 compensates the mismatch due to the TOD but additional TOD is introduced by the negative TOD of SF11. Therefore, more sophisticated techniques has to be developed to compensate the TOD. S. W. Jolly suggested to use TOD mirrors on one of the arms to compensate for the additional TOD. The simulations to determine the correct amount of TOD are done by S. W. Jolly and it is ongoing research. An efficiency increase of a factor of 2 will be resonable.

Adding these new ideas to the achievements of the thesis it seems possible to reach the mJ-energy level of multi-cycle THz pulses and to meet the goals of Axsis.

6. Conclusions and outlook

In the framework of this thesis the generation of strong field, multi-cycle THz pulses in periodically poled lithium niobate (PPLN) was demonstrated. Special attention was paid to the pumping mechanism as well as to the physical properties of the optical materials. Two different pumping mechanisms to increase the THz pulse energy were evaluated.

The investigations of material properties focused on the refractive index and the absorption coefficient. With the presented experiments a better understanding of the factors that determine the conversion efficiency in the low frequency range of 0.2 - 1 THz was achieved. Several optical crystals mainly lithium niobate ($LiNbO_3$), but also polymers were investigated with a terahertz time domain spectrometer (THz-TDS) or a Fourier transform infrared spectrometer (FTIR).

The two different pumping mechanisms to generate Multi-cycle THz pulses were experimentally demonstrated: Optical rectification with a train of compressed broadband pulses and difference frequency generation with either a pulse train or two chirped-and-delayed pulses.

Optical rectification with a train of pulses: The performance of a train of two compressed pulses with equal energy followed by several lower energy pulses is compared to that of the single pulse. The split of pulses leads to an increase in efficiency due to coherent addition of the generated THz pulses of each pump pulse. Due to the lower individual peak intensity the presence of the train increases the incident pump fluence ($F = 164\,\mathrm{mJ/cm^2}$) compared to a single pulse ($F = 80\,\mathrm{mJ/cm^2}$). A maximal THz energy of $E_{THz} = 0.8\,\mu\mathrm{J}$ with an energy conversion efficiency of $\eta = 0.05\%$ was achieved at room-temperature in a PPLN matched for a frequency of 0.52 THz. The efficiency increased by a factor of 2.6 compared to the single pulse.

These experimental results can be regarded as proof of the principle. An even higher conversion efficiency is expected to be possible by cryogenic cooling of the PPLN. A possibility to extend the concept is to pump with 4, 8, 16 or even more pulses to reach even higher energies.

Difference frequency generation with chirped-and-delayed pulses: For difference frequency generation with chirped-and-delayed pulses a broadband pump pulse is used to supply sufficient spectral components in the pulse to generate the required frequency content and high energy multi-cycle THz pulses. In the first experiment a THz pulse at a frequency of 0.545 THz reached an energy of 40 µJ outperforming earlier results for similar pulse characteristics. As the pump pulse delivers also higher order dispersion, only a part of the pump spectrum is generating the THz pulse. First experiments to compensate the effects of higher order dispersion on the pump pulse were encouraging. Compensating the higher order dispersion with asymmetric chirp on the two pump pulses an energy up to 127 µJ was generated at a frequency of 0.36 THz by using a large aperture PPLN. To the best of our knowledge this energy is the highest presented energy for a narrowband THz pulse [Che11, Car15]. Furthermore the reported conversion efficiency of $\eta = 0.187\%$ for the frequency of 0.36 THz can be assessed as an extraordinary conversion efficiency. The THz pulse has a duration of at least 283 ps and a bandwidth of 3.4 GHz proving the narrowness of the spectrum of the THz pulse.

These results give confidence to reach mJ-level THz pulses. As described in section 5.5, the energy of the multi-cycle THz pulses may be increased with an AR coating for the IR and the THz as well as a higher pump fluence closer to the damage threshold of lithium niobate at this laser system. Compensating the residual delay mismatch due to the TOD on the broadband pump pulses is expected to increase the efficiency at least by a factor of 2. In addition to the improvements on the THz generation the unused pump pulse generated in the Mach-Zehnder interferometer can be used to generate a second beam line with another crystal. Combining both identically generated pulses and adding them coherently may help to reach the goal of THz pulses with an energy of more than $E = 5\,\mathrm{mJ}$. THz pulses with this energy have a peak field of more then 100 MV/m, if they are focused to the diffraction limit, which is the appropriate range for efficient electron acceleration with THz pulses.

The experiments of this thesis contribute to the further source development for the AXSIS project but the design of the AXSIS machine requires a high energy laser at repetition rate of about 100-1000 Hz. With high energy Ti:sapphire based systems with energies of about 1 J used for this thesis the requested repetition rates are not achievable. Therefore the AXSIS machine will be based on high energy Ytterbium based laser systems with a wavelength centered at 1.03 µm which are capable to reach the required repetition rate. So far these laser systems have reached energies up to 100 mJ [Zap15, Rea12] and energies of up to 1 J are already demonstrated at a repetition rate of 500 Hz [Bau16]. Further improvements are in development to achieve even energies up to 1 J at a repetition rate of 1 kHz. The bandwidth of the Ytterbium laser systems are narrower than the bandwidth of Ti:sapphire based systems. Therefore generating THz pulses with the Ytterbium based laser systems requires further development as the frequency content necessary has to be generated beforehand. The THz cascaded optical parametric amplifier (THz-COPA) is the first experiment to reach highly efficient multi-cycle THz pulse with a narrowband pump laser [Cir17]. Conversion efficiencies up to 10% are theoretically predicted [Rav16a].

The experiments to generate high energy multi-cycle THz pulses at the Ti:sapphire based laser systems provided useful information to understand the scalability and the behavior of narrowband THz pulses. Based on on the results presented, mJ-level, multi-cycle THz pulses as required for the AXSIS project finally come into reach.

Appendices

A. Lithium niobate

This appendix summarizes all interesting properties of lithium niobate ($LiNbO_3$), the crystal structure and symmetry, how it can be produced, his optical properties as well as further technological properties. $LiNbO_3$ is a man-made dielectric and ferroelectric material, which was first described in 1929 [Zac29]. The first single crystals were synthesized and investigated in detail regarding their physical properties by Bell Labs in the 1960s [Boy64, Nas66a, Nas66b, Abr66c, Abr66a, Abr66b]. $LiNbO_3$ is a dielectric, birefringent, non-centrosymmetric, uniaxial negative crystal and exhibits favorable properties:

- ferroelectric
- linear and nonlinear optical
- electro-optical
- pyroelectric
- piezoelectric
- photorefractive

This following sections will detail principle properties reported in publications [Boy64, Nas66a, Nas66b, Abr66c, Abr66a, Abr66b].

A.1. Crystal structure and symmetry

Lithium niobat is synthesized in a Czochralski process via a solid state or melting reaction of lithium carbonate with niobium(V) oxide [Nas66a, Nas66b, O'B85]:

$$Li_2CO_3 + Nb_2O_5 \longrightarrow 2\ LiNbO_3 + CO_2 \uparrow \qquad \text{(A.1.1)}$$

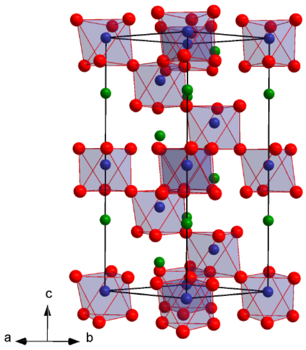

Figure A.1: Crystal structure of lithium niobate (Wikimedia-commons [WC08]). The niobium atoms (blue) are surrounded by 6 oxygen atoms (red) in an octahedral structure. The lithium atoms (green) are in the vacancies of the three dimensional grid of niobium and oxygen.

Due to its rotation and mirror symmetry, $LiNbO_3$ belongs in the space group $R3c$ and the point group $3m$.

Figure A.1 shows the crystal structure of $LiNbO_3$. The niobium atoms (blue) are surrounded by 6 oxygen atoms (red) in an octahedral structure. The lithium atoms (green) are in the vacancies of the three dimensional grid of niobium and oxygen. The crystal with his hexagonal structure in the projection of the z-axis has 4 axes, a_1, a_2, a_3 and c, where the 3 a axes are in one plane 120° apart and normal to the c-axis. The angle between the c-axis and the cleavage plane indicating the x-and y-axes is 32.75°[Abr66c].

Along the c-axis the crystal is structured with the octahedral interstices as niobium, vacancy lithium vacancy, niobium, vacancy, etc. The relative position of the lithium and the niobium in respect to the oxygen octahedral defines the para-electric and ferro-electric phases of the crystal. They are defined in relation to the the Curie temperature of 1210°C [Wei85].

- In the para-electric phase, the positions of niobium atoms are equally probable to be either above or below the oxygen layers by 0.37 angstrom, while the lithium atoms are located right on the oxygen layer.
- At temperatures below the Curie temperature, elastic forces become dominant and induce a new charge separation, resulting in a spontaneous polarization P_S. This makes $LiNbO_3$ to be a displacement ferroelectric.

As the Curie-temperature is 1210°C the $LiNbO_3$ crystal resides at room-temperature in its ferroelectric phase.

The ferroelectric phase $LiNbO_3$ exhibits three-fold rotation symmetry about its c-axis. These types of crystals are called trigonal $R3c$. It exhibits mirror symmetry about three planes that are 60 degrees apart and intersect forming a three-fold rotation axis. The two most common methods to determine the direction of the $c+$-axis are compression or cooling. In either, the lithium and niobium ions move relative to the oxygen octahedral. Upon compression the ions move closer to their para-electric positions with respect to the oxygen layers, thereby reducing the net polarization. In the case of cooling, the elastic forces pull the ions further from their corresponding oxygen layers and increase net polarization, a contrary effect [Wei85].

A.2. Stoichiometry and doping

Stoichiometric lithium niobate has the formula $Li_{1.0}Nb_{1.0}O_{3.0}$ [O'B85]. Violations of the stoichiometry of $LiNbO_3$ can occur either as a change of the degree of oxidation or as change in the Li/Nb ratio. Growing stoichiometric $LiNbO_3$ is possible with solid solutions deficient in oxygen produced by annealing $LiNbO_3$ in vacuum, or in an inert or reducing atmosphere, and also by passing an electric current through heated $LiNbO_3$. Oxygen-deficient $LiNbO_3$ results in an intense color and an increased electric conductivity. The deficiency can be removed by an oxidizing annealing process. Changing the ratio of lithium to niobium, the congruent $LiNbO_3$ can be grown with the ration of 0.945 of lithium to 1 of niobium. To reduce the defects in the crystal, the congruent grown $LiNbO_3$ can be doped with several dopants. Magnesium doping is here the most prominent dopant and can be used to achieve similar electric and optic properties on congruent $LiNbO_3$ as for stoichiometric $LiNbO_3$.

A.3. Physical effects and optical properties

$LiNbO_3$ has favorable properties which leads to several applications [Wei85, Mül04, Jen10]:

A.3.1. Ferroelectricity

As described before, $LiNbO_3$ is a ferroelectric crystal which has a spontaneous polarization P_S. The ferro-electricity of $LiNbO_3$ was found in 1949 [Mat49]. The orientation of this polarization can be inverted via introducing a electrical current onto the crystal. This effect is utilized to produce periodically poled lithium niobate (PPLN).

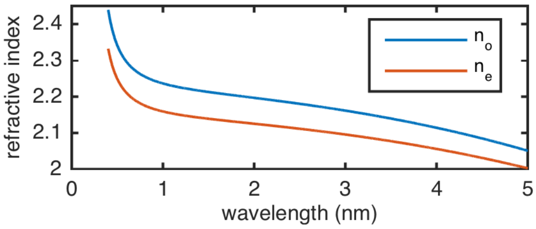

Figure A.2: Refractive index of the ordinary (blue) and extraordinary (red) crystal orientation of lithium niobate to visualize the negative birefringence (Data from [Zel97]).

A.3.2. Pyroelectric effect

The spontaneous polarization P_S changes with temperature. As the lithium and niobium atoms are just movable in z direction the pyroelectric vector are be described by [Sav66]

$$\vec{p_i} = p_z = -4 \times 10^{-9} \mathrm{C/cm^2 {}^\circ C} \tag{A.3.1}$$

A.3.3. Permittivity and birefringence

LiNbO$_3$ is a non-gyrotropic material [Wei85]. Therefore only the diagonal elements of the permittivity tensor are non-zero. Since LiNbO$_3$ crystal is symmetric about the c-axis, the permittivity can be represented by

$$D_i = \sum_i \epsilon_{ij} E_j \qquad \text{with} \qquad \epsilon_{ij} = \begin{pmatrix} \epsilon_{11} & 0 & 0 \\ 0 & \epsilon_{11} & 0 \\ 0 & 0 & \epsilon_{33} \end{pmatrix}, \tag{A.3.2}$$

where D_i is the electric flux density, E_i the electric field and $i = x, y, z$ the directions [Wei85]. As $n_e = \sqrt{\frac{\epsilon_{33}}{\epsilon_0}}$ and $n_o = \sqrt{\frac{\epsilon_{11}}{\epsilon_0}}$ describes the refractive index of the crystal, LiNbO$_3$ is negatively birefringent [Wei85]. The wavelength dependent extraordinary refractive index of lithium niobate is [Zel97]

$$n_e^2 - 1 = \frac{2.9804\lambda^2}{\lambda^2 - 0.02047} + \frac{0.5981\lambda^2}{\lambda^2 - 0.0666} + \frac{8.9543\lambda^2}{\lambda^2 - 416.08}. \tag{A.3.3}$$

The refractive indices for the extraordinary and ordinary axis of lithium niobate are depicted in figure A.2 after the data from [Zel97]. At a wavelength of 800 nm the refractive index is [Zel97, Jun97]

$$n_e = 2.1755 \qquad\qquad n_o = 2.2553 \tag{A.3.4}$$

The refractive index is furthermore temperature dependent, for more detailled description *Schlarb et al.*[Sch93] or *Gayer et al.* [Gay08] may be used.

A.3.4. Linear electro-optic effect

Non-centrosymmetric crystals, like lithium niobate, produce changes of the refractive index that are proportional to the applied field, which is named the linear electro-optic (EO) effect or Pockels effect. When an electric field, E_k, is applied to the crystal, the refractive index changes according to

$$\Delta\left(\frac{1}{n^2}\right)_{ij} = \sum r_{ijk} E_k \tag{A.3.5}$$

$$\Delta n = -\frac{n_0^3}{2} r_{ij} E_j, \tag{A.3.6}$$

where r_{ijk} is the EO tensor. This tensor also depends on the crystal symmetry and is closely related to the piezoelectric tensor [Len66].

A.3.5. Piezoelectric effect

Applying physical stress or mechanical forces onto the crystal results in electric field and therefore polarization in one of the directions of crystal, the piezoelectric effect. It also workes the other way around, the electric field onto the crystals results in a length change or a shearing effect. The piezoelectric effect results in an induceed polarisation change which can be written as

$$P_i = \sum_{j,k} e_{ijk} \cdot \sigma_{jk} \tag{A.3.7}$$

or in a strain tensor

$$S_{jk} = \sum_i d_{ijk} \cdot E_i. \tag{A.3.8}$$

For all crystals in the point group $3m$ the piezoelectric strain tensor can be written as [Wei85]

$$d_{ijk} = \begin{pmatrix} 0 & 0 & 0 & 0 & d_{15} & -d_{22} \\ -d_{22} & d_{22} & 0 & d_{15} & 0 & 0 \\ d_{15} & d_{15} & d_{33} & 0 & 0 & 0 \end{pmatrix}. \tag{A.3.9}$$

For the stress tensor e_{ijk} the same relation occur. The coefficients where determind by *Smith et al.* [Smi71] as

$$e_{15} = 2.72, e_{22} = 1.67, e_{31} = -0.38, e_{33} = 1.09 \qquad \times \mathrm{C/m^2} \tag{A.3.10}$$

$$d_{15} = 2.64, d_{22} = 0.75, d_{31} = -0.30, d_{33} = 0.57 \qquad \times 10^{-11}\mathrm{C/N}. \tag{A.3.11}$$

The thickness d of a lithium niobate crystal changes with an external field E via

$$\frac{\Delta d}{d} = \frac{e_{33}}{C_{333}} E \tag{A.3.12}$$

in the direction of the c-axis [Lue03]. Hereby is $e_{33} = 1.785\mathrm{C/m}^2$ und $C_{333} = 2.357 \times 10^{11}\mathrm{N/m}^2$ [Jaz02].

A.3.6. Photorefractive effect

Another important property to consider is the photorefractive (PR) effect, which is an optically induced change in refractive index. PR effects can cause beam distortion and scattering, so have to be considered as a detrimental effect. It is not a single-effect per se, but rather a combination of effects. In the case of lithium niobate, when light propagates through the crystal, an optically induced space charge is generated, in which ion impurities (such as Iron) can be photoexcited and produce electrons and holes [Gla74]. The movement of charges results in an electric field, and via EO effect, it causes a change in refractive index. Since both electrons and holes can contribute to this migration of charge, the PR susceptibility of the material is controlled by the oxidation state ratio of the 2+ and the 3+ Iron ions. Optimizing or balancing that ratio is a possible approach to reduce PR effects. Other solutions have been found to self-anneal at 180°C and above reduces effect for visible radiation, and at 100°C for infrared [Ram00]. Furthermore, increasing the conductivity by using dopants helps to reduce the PR effects [Sch11].

A.3.7. Transparency range

$LiNbO_3$ is transparent from 0.32 µm to 5.6 µm. The band edge in UV can be shifted by the concentration of the dopants [Wen05]. Furthermore, at wavelengths around $\lambda = 2.8$µm the OH^--binding vibrates leading to an absorption peak. This peak can be again shifted by the concentration of dopants [Wen05].

In the far-infrared (FIR) range the $LiNbO_3$ crystals are not transparent. The reflectivity in the FIR is dominated by the soft vibrational modes [Ser79]. The lowest frequency mode around a wavenumber of 250 cm^{-1} corresponding to a frequency of 7.6 THz. Thus is also analyzed in detail by *Feuer et al.* [Feu07]. Below that lowest phonon the transparency of the crystal is increasing (see section 2.2.1).

A.3.8. Nonlinear optical effect

$LiNbO_3$ is an efficient nonlinear optical crystal [Boy64]. The optical field of a laser pulse changes the polarization density $\vec{P}$, which can be expressed by [Lee09]

$$\begin{pmatrix} P_x \\ P_y \\ P_z \end{pmatrix} = 2\epsilon_0 \begin{pmatrix} 0 & 0 & 0 & 0 & d_{15} & -d_{22} \\ -d_{22} & d_{22} & 0 & d_{15} & 0 & 0 \\ d_{15} & d_{15} & d_{33} & 0 & 0 & 0 \end{pmatrix} \begin{pmatrix} E_x^2 \\ E_y^2 \\ E_z^2 \\ 2E_yE_z \\ 2E_zE_x \\ 2E_xE_y \end{pmatrix} . \tag{A.3.13}$$

This tensor provides mainly the reason for the wide spread as nonlinear optical media. They deliver the responsible coefficients for frequency mixing. For example if two waves both in the direction of z mix with each other the polarisation can be calculated with $P_z = 2\epsilon_0 d_{33} E_z^2$, which is for example the DFG in lithium niobate.

The highest nonlinear coefficient is $d_{33} = 42$pm/V [Boy64, Sho97] in the optical range, which corresponds to interactions that are parallel to the c-axis. In the THz range, which is well below the phonon resonances, the effective nonlinear coefficient is constant and can be calulated via

$$d_{jkl} = -\frac{n^4}{4r_{jlk}}, \tag{A.3.14}$$

where n is the refractive index in the optical and r_{jlk} the linear electro-optical coefficient [Boy71]. For periodically poled MgO:LN, the effective nonlinear coefficient d_{eff} is the nonlinear coefficient of the bulk lithium niobate in the direction of the c-axis and thus $d_{eff} = d_{33}$. In lithium niobate the effective nonlinear coefficient is thus $d_{eff} = 152.4$ [Vod08]. Experimentally the nonlinear coefficient was obtained to be $d_{eff} = 93$pm/V in the THz regime [Sow10].

A.4. Periodically poled lithium niobate

Periodically poled lithium niobate is produced via domain inversion of single parts in the optical crystal. The oxygen levels are staying the same in this process, just the position of the lithium and niobium atoms is changed so that the spontaneous polarization is changed by 180°. To achieve this inversion for lithium niobate a rather high coercive field strength has to be applied [Yam93].

Due to the high fields it is tricky to pole thick lithium niobate wafers. Therefore the thickness of PPLN is limited to a few millimeters to achieve a homogeneous poled structure. Only *T. Taira* [Ish12] provides crystals with a thickness of 10 mm.

G. Miller [Mil98] describes in his thesis the fabrication of PPLN. On a wafer, where the z-axis is pointing to the top, a mask with electrodes is glued. The current on the mask introduce the domain walls changing the orientation to the opposite site. Optimizing the current at the electrodes resolves in a homogeneous poled crystal or if wanted in more fancy structures. Poling periods for a wide range from a $\sim$ 1µm [Bus02] to millimeters are possible. Generation of THz radiation requires poling periods from 0.125 mm to 1.2 mm phase-matched for 0.9 THz to 0.1 THz, respectively.

B. THz-TDS and FTIR data

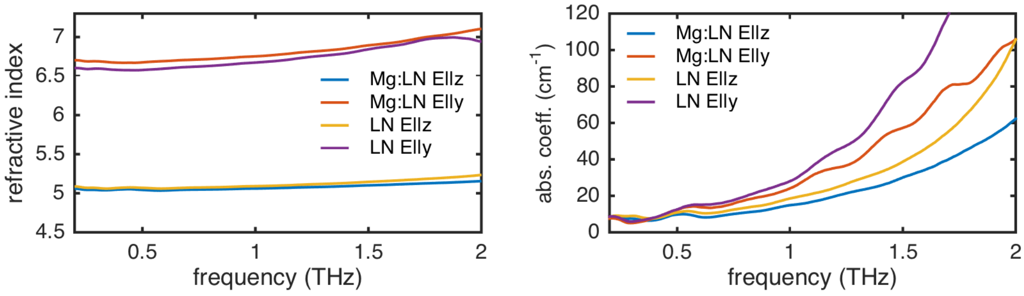

Figure B.1.: Refractive index (left) and absorption coefficient (right) of lithium niobate and 5 mol% magnesium doped lithium niobate. Full frequency range of the zoomed figure 2.10.

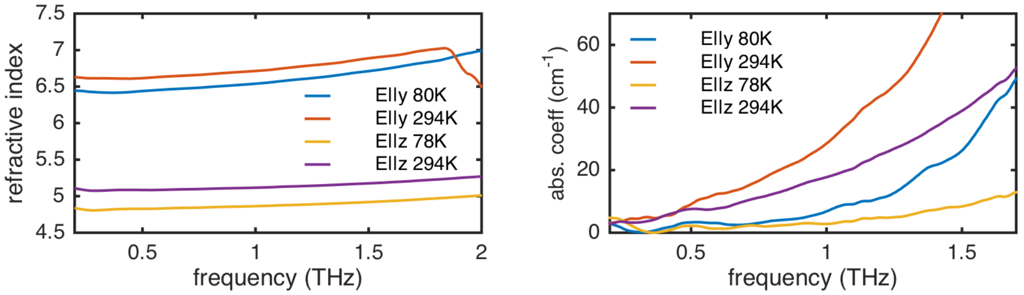

Figure B.2.: Temperature dependence of the refractive index (left) and absorption coefficient (right) of 5 mol% MgO:LN. Full frequency range of the zoomed figure 2.12.

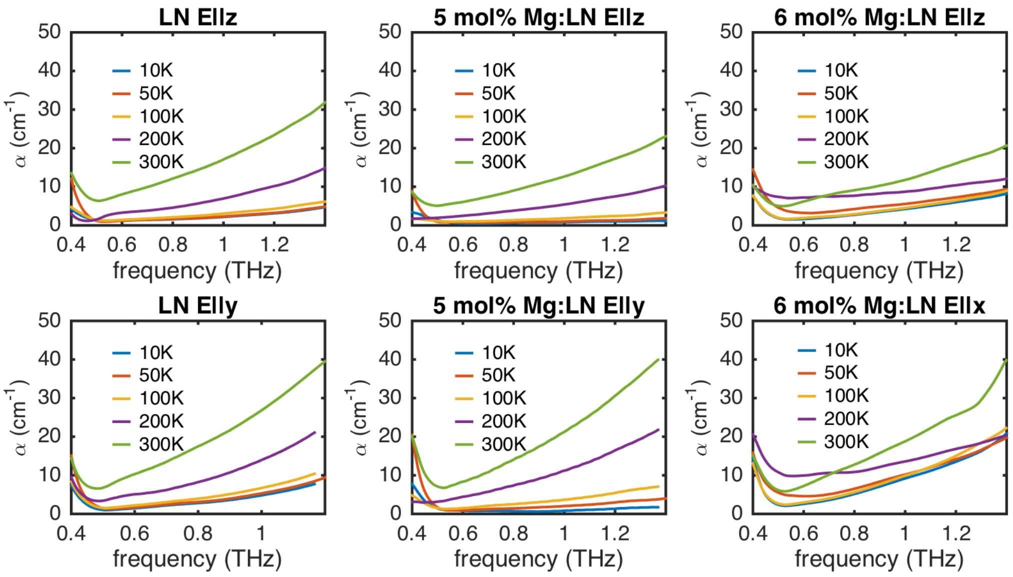

Figure B.3.: Temperature dependence of the absorption coefficient for a x-cut lithium niobate wafer, a x-cut 5 mol% magnesium doped lithium niobate wafer and a y-cut 6 mol% magnesium doped lithium niobate wafer measured at the FTIR. Full frequency range of the zoomed figure 2.13.

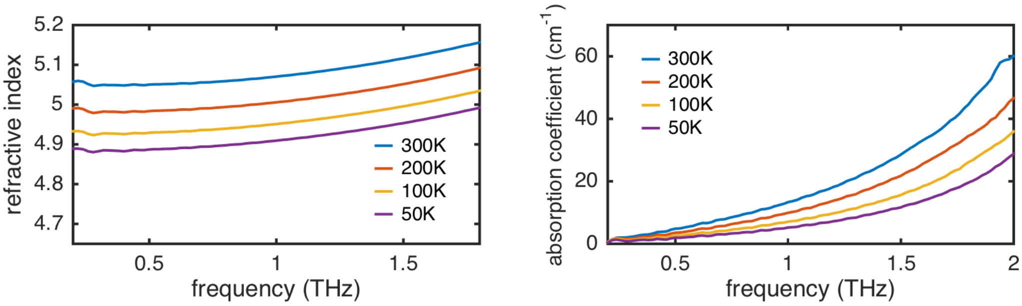

Figure B.4.: Temperature dependent refractive index (left) and absorption coefficient (right) of 5 mol% MgO:LN for the extraordinary axis ($E||z$) (Data of [Wu15]). Full frequency range of the zoomed figure 2.14.

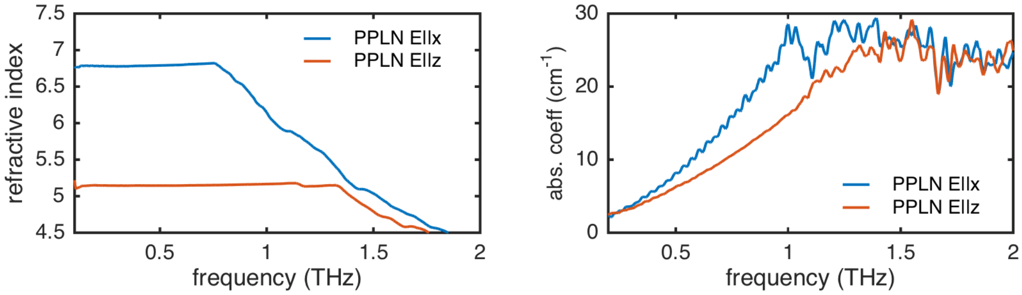

Figure B.5.: Refractive index (left) and absorption coefficient (right) of 5 mm long 5 mol% periodically poled MgO:LN at room temperature. Full frequency range of the zoomed figure 2.15.

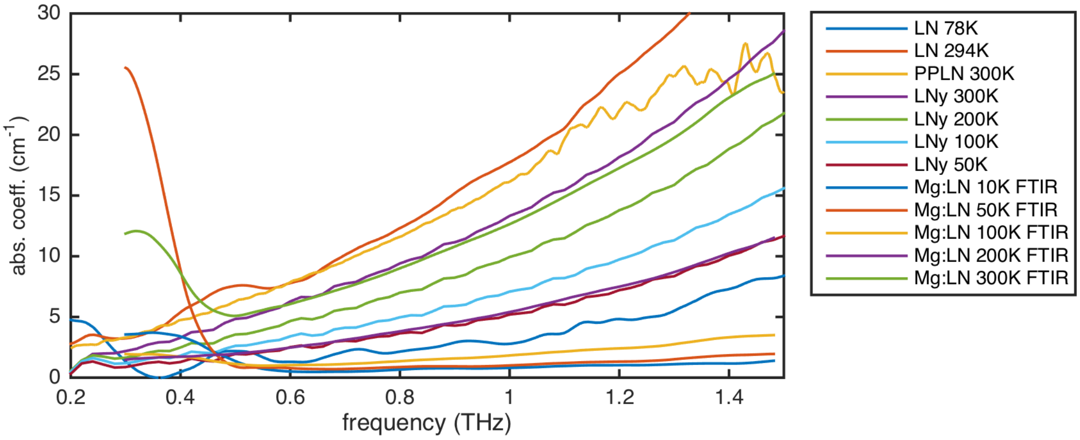

Figure B.6.: Comparison of the absorption coefficient between various 5 mol% periodically poled MgO:LN samples at different temperatures measured at the THz-TDS and the FTIR. Full frequency range and all temperatures of the zoomed figure 2.15.

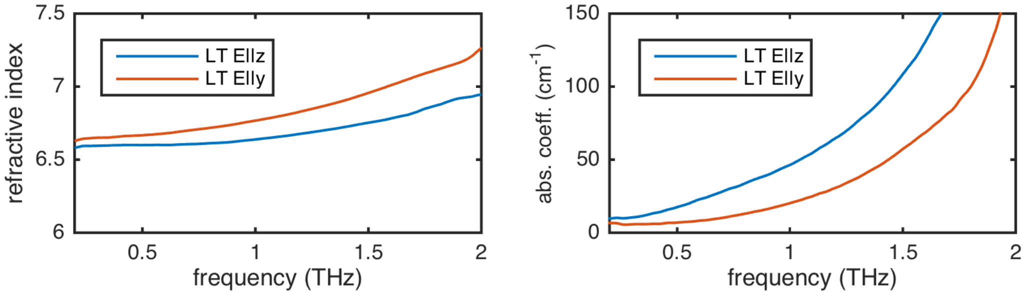

Figure B.7.: Refractive index (left) and absorption coefficient (right) of lithium tantalate. Full frequency range of the zoomed figure 2.18.

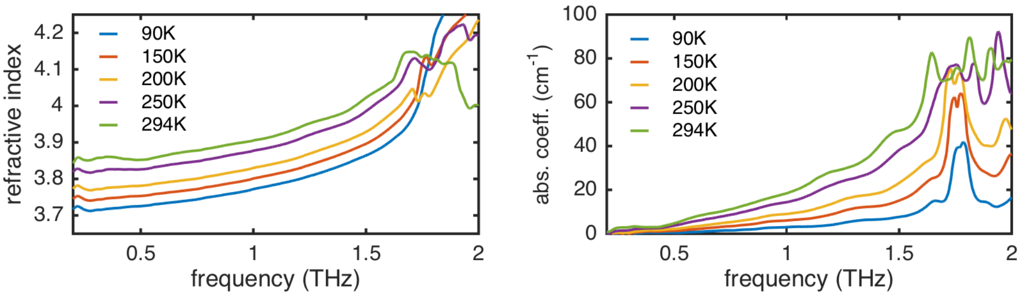

Figure B.8.: Refractive index (left) and absorption coefficient (right) of Rb:KTP for various temperatures. Full frequency range of the zoomed figure 2.23.

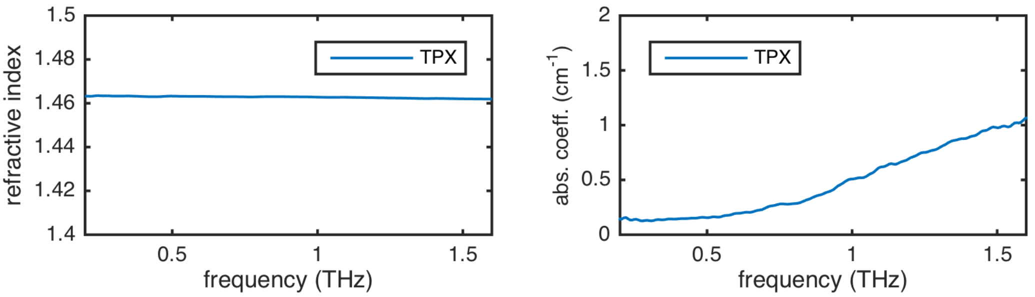

Figure B.9.: Refractive index (left) and absorption coefficient (right) of TPX. Full frequency range of the zoomed figure 2.25.

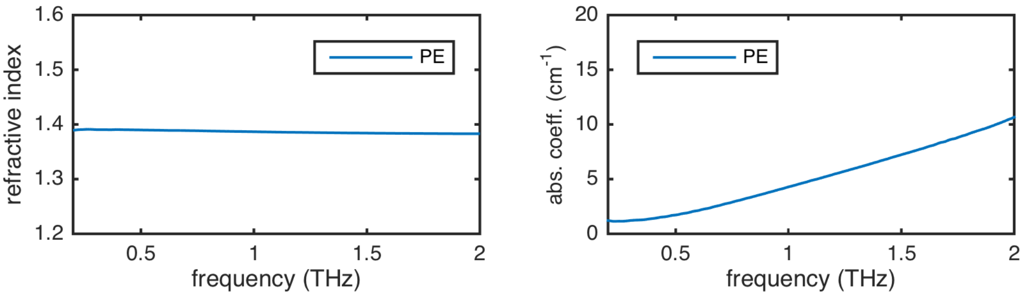

Figure B.10.: Refractive index (left) and absorption coefficient (right) of polyethylene. Full frequency range of the zoomed figure 2.26.

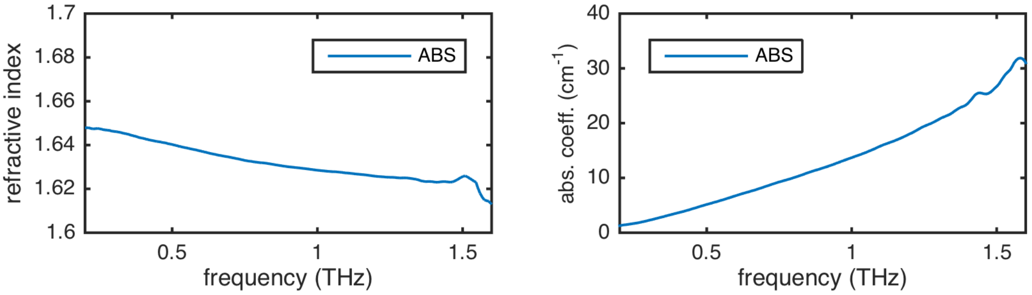

Figure B.11.: Refractive index (left) and absorption coefficient (right) of ABS. Full frequency range of the zoomed figure 2.27.

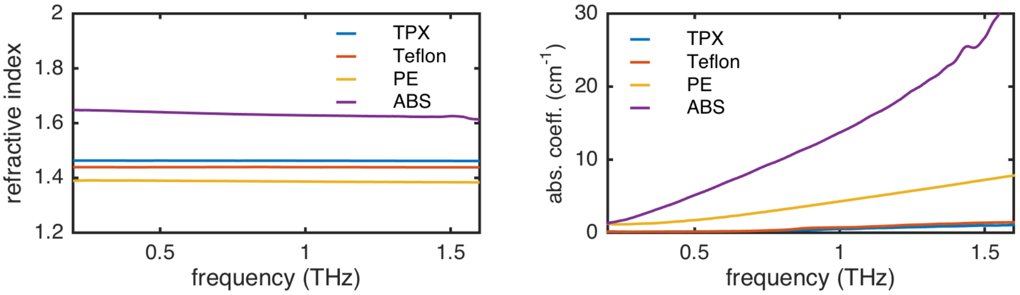

Figure B.12.: Summary of refractive index (left) and absorption coefficient (right) of different polymers. Full frequency range of the zoomed figure 2.28.

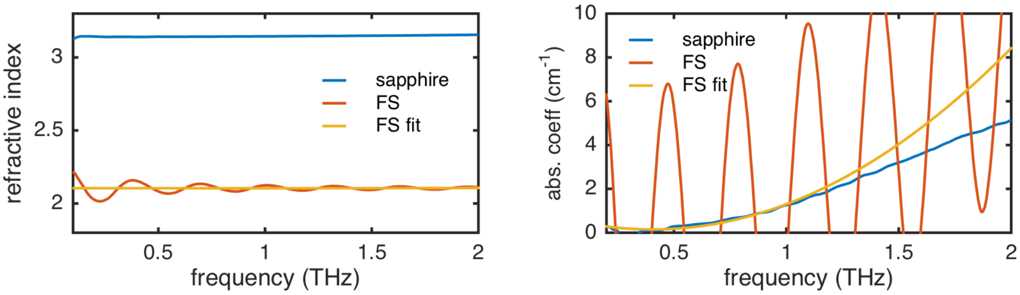

Figure B.13.: Summary of refractive index (left) and absorption coefficient (right) of a sapphire and a fused silica window. Full frequency range of the zoomed figure 2.29.

C. Analysis of measurement uncertainties in the THz-TDS

The investigations described in chapter 2 and especially in section 2.2.1 and the results achieved have to be considered together with the uncertainty of the underlying parameters. The appendix C reviews the data regarding possible errors and error propagation similar to literature like [Wit08, Naf13] describing the uncertainties and systematic errors in TDS systems.

C.1. Instrumental error

The THz-TDS system itself is described in detail in section 2.1.1. In the following the instrumental limitations and statistical errors are discussed.

C.1.1. Instrumental limitations leading to derived errors

Determination of upper limit of frequency

Reliable measurement results are reached if the signal values exceed the noise level. From visual inspection in figure C.1 (left) the FFT spectrum of the reference (blue) and especially the FFT spectrum of the sample (red) have a part which disappears in the noise level. From that sample trace it can be conducted that frequencies above 1 THz are not resolvable for this sample. The dynamic range (see figure C.1 right) of the system indicates the highest possible frequency for measurements to be 4 THz. The noise level is 40 dB below the maximum signal at 0.513 THz. The 3 dB area is from 0.19 to 1.08 THz.

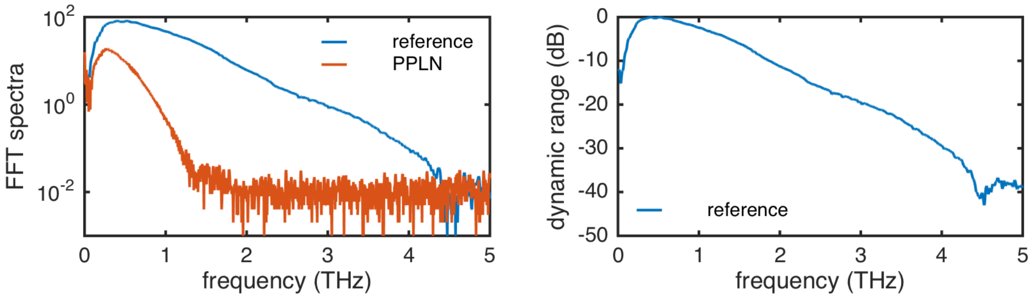

Figure C.1.: Left: FFT spectra of the THz signal of the reference and the PPLN sample. **Right:** Dynamic range of the THz-TDS.

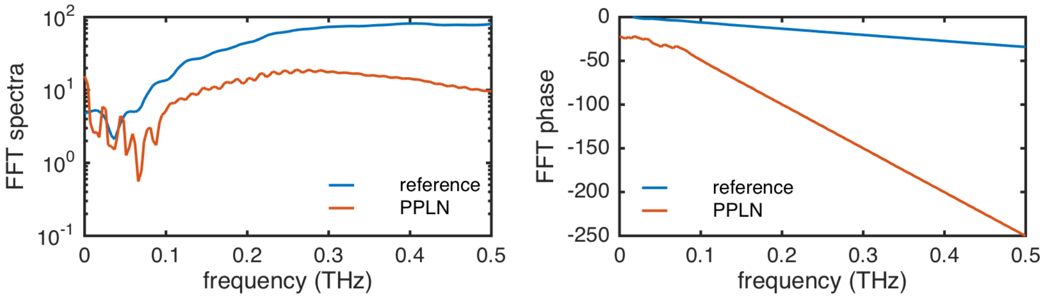

Figure C.2.: Zoom into the FFT spectra (left) and the FFT phase (right) of the reference and the PPLN in the low frequency range 0 to 0.5 THz.

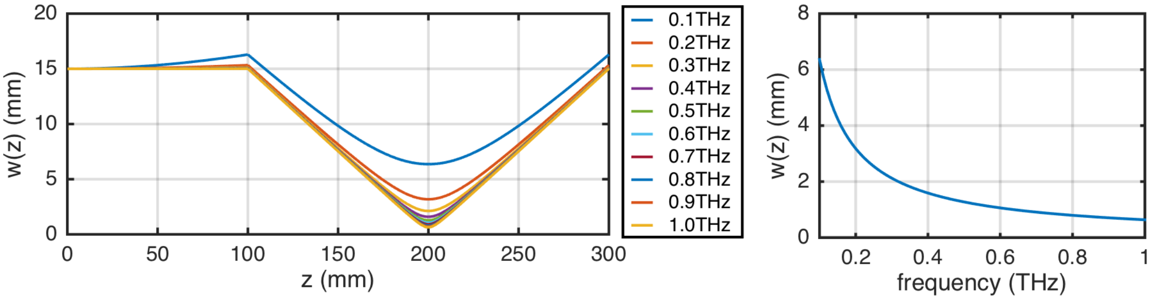

Figure C.3.: Left: Beam waist for the imaging setup of the THz-TDS for THz frequencies of 0.1 to 1 THz. **Right:** Line out of the beam size at the sample position.

Determination of lower limit of frequency

In figure C.2 the FFT spectrum and FFT phase at low frequencies are depicted for the reference and the PPLN sample. Visual inspection indicates steady data at high frequencies. Below 0.1 THz the antenna emits signals with a high statistical error resulting in high fluctuations on the FFT spectra and phases. The data in this range are not reliable and can no longer be used to calculate the refractive index and the absorption coefficient.

Assembly risks on beam path

As the THz-TDS is using THz radiation, the Gaussian beam propagation and its divergence have to be considered to describe the frequency dependence of the beam spot size at the sample position. As described in section 2.1.1, the THz pulse is focused with a lens onto the sample (see figure 2.2). Figure C.3 (left) shows the beam path of a collimated beam with a beam radius of 15 mm focused with a lens (f = 100 mm) at z = 100 mm onto the sample position. The interrelation of the frequency and the beam radius at the sample position is lined out in figure C.3 (right). Using a sample with a clear aperture of 4 mm all frequencies above 0.32 THz are transmitted without losses due to the aperture. To resolve frequencies below 0.32 THz without perturbations from the Gaussian beam propagation the sample requires a larger clear aperture: for example to reach 0.2 THz a clear aperture of 6.4 mm is necessary, at 0.15 THz a sample size of 8.5 mm and at 0.1 THz a sample size of 12.7 mm are necessary.

These values for the clear aperture are only valid if the sample is perfectly aligned. In addition this estimation is based on the diffraction limited spot size which is the lower

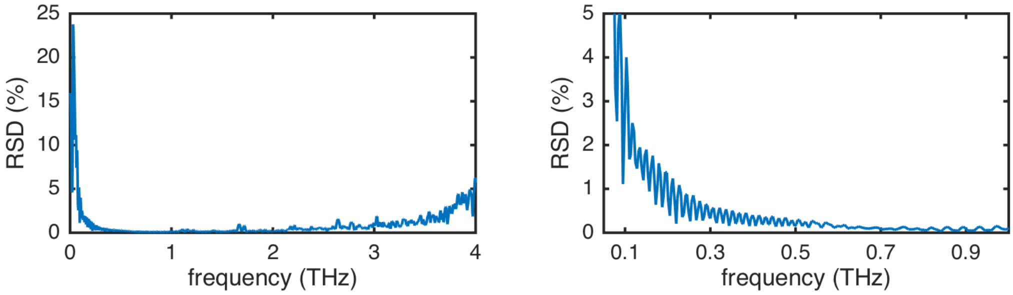

Figure C.4.: Relative standard deviation of the reference signal in 10 measurements for the full spectrum (left) and for a zoom into the low frequency range of 0.05 to 1 THz (right).

bound of the spot size. Furthermore, having passed the sample the divergence of the THz wave in this frequency range (see chapter 3.2) can misalign the optical beam path and influence the detected signal. In this case the reference signal, which is required for the calculation of the optical properties, and the sample signal are not matching. To have no influence from the THz beam itself and its divergence the clear aperture should be in the order of 15 to 20 mm.

C.1.2. Statistical error

All measurements on the THz-TDS conducted for this thesis are averaged over 400 or more waveforms to minimize the statistical error. The mean of 400 waveforms can be reach either with a measurement range of 200 ps and the integration time of 100 s or a range of 100 ps and integration time of 50 s. With a mean of 400 waveforms or more the fluctuations on the system are minimized and the statistical error is minimized.

Figure C.4 shows the dependence of relative standard deviation (RSD) of 10 measurements against the frequency for the reference signal in full scale to 4 THz (left) and zoomed into the low frequency range of 0.1 to 1 THz. From the RSD of the reference the possible performance of the THz-TDS can be judged. In the range between 0.2 and 3 THz the RSD is below 1% which allows an accurate measurement in this range. Below 0.2 THz the statistical error increases steep by reaching 5% at 0.1 THz. This statistical error (RSD) is taken as the error in the FFT signal required for the calculation of the absorption coefficient which will be discussed in the following.

C.2. Uncertainty in parameter extraction

C.2.1. Error propagation of the refractive index and the absorption coefficient

The determination of the refractive index is based on

$$n(\nu) = 1 + \frac{c}{2\pi\nu d}\left(\phi_s(\nu) - \phi_r(\nu)\right). \tag{C.2.1}$$

Accordingly the error on the refractive index Δn is depending on the error of the thickness Δd and the error of the phase of the sample $\Delta\phi_s$ and the reference $\Delta\phi_r$. The error of the refractive index is calculated via

$$\Delta n(\nu) = \sqrt{\left(\frac{\partial n}{\partial d}\Delta d\right)^2 + \left(\frac{\partial n}{\partial \phi_s}\Delta\phi_s\right)^2 + \left(\frac{\partial n}{\partial \phi_r}\Delta\phi_r\right)^2} \tag{C.2.2}$$

$$= \frac{n\ c}{2\pi\nu d}\sqrt{\frac{\left(\phi_s(\nu) - \phi_r(\nu)\right)^2}{d^2}\Delta d^2 + \Delta\phi_s^2 + \Delta\phi_r^2}. \tag{C.2.3}$$

The determination of the absorption coefficient is based on

$$\alpha(\nu) = -\frac{2}{d}ln\left(\rho(\nu)\frac{[n_2(\nu)+1]^2}{4n_2(\nu)}\right), \tag{C.2.4}$$

where $\rho(\nu) = \frac{E_s}{E_r}$. The error on the absorption coefficient $\Delta\alpha$ is depending on the error of the thickness Δd, the error of the refractive index Δn and the error on the THz signal of the sample ΔE_s and the reference ΔE_r. It is calculated via

$$\Delta\alpha(\nu) = \sqrt{\left(\frac{\partial\alpha}{\partial d}\Delta d\right)^2 + \left(\frac{\partial\alpha}{\partial n}\Delta n\right)^2 + \left(\frac{\partial\alpha}{\partial E_s}\Delta E_s\right)^2 + \left(\frac{\partial\alpha}{\partial E_r}\Delta E_r\right)^2} \tag{C.2.5}$$

$$= \sqrt{\left(\frac{\alpha}{d}\Delta d\right)^2 + \left(\frac{2-2n}{d(n^2+n)}\Delta n\right)^2 + \left(\frac{2}{dE_s}\Delta E_s\right)^2 + \left(\frac{2}{dE_r}\Delta E_r\right)^2}. \tag{C.2.6}$$

The error propagation of the refractive index and the absorption coefficient has to consider five errors of underlying variables:

- error of thickness: Δd,
- error of reference phase: $\Delta\phi_r$,
- error of sample phase: $\Delta\phi_s$,

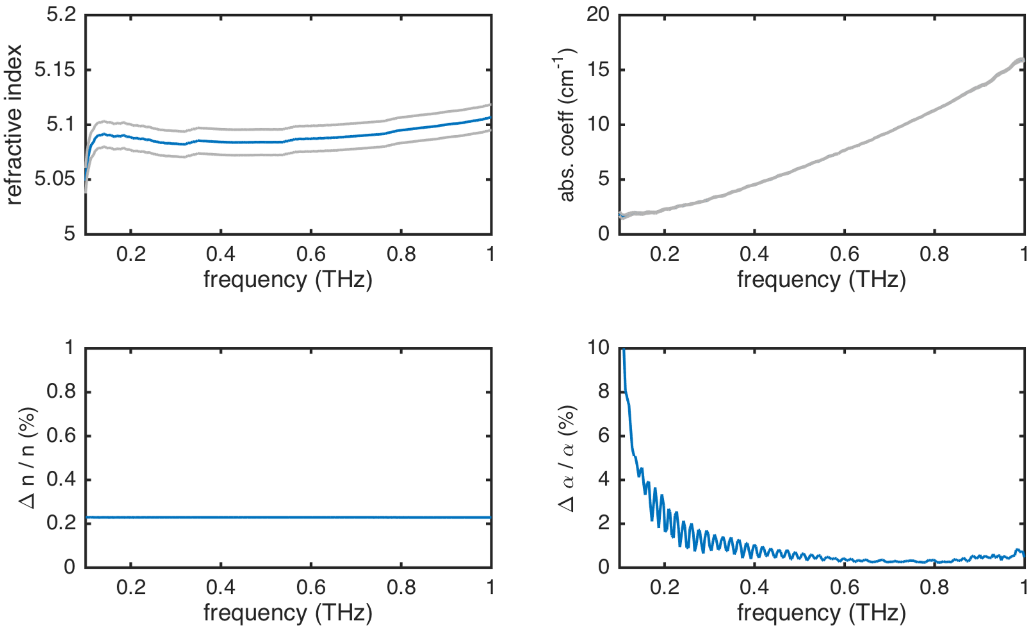

Figure C.5.: Top: Refractive index (left) and absorption coefficient (right) with the corresponding error range (grey) of a PPLN with a length of 5.05 mm. **Bottom:** Corresponding relative error of the refractive index and absorption coefficient.

- error of reference THz signal: ΔE_r,
- error of sample THz signal: ΔE_s.

Hereby the errors are either known as physical measurement inaccuracy (Δd), they can be calculated from a measurement inaccuracy ($\Delta\phi_r$) or they are based on the statistical error. The statistical errors determine the errors of the THz signals. The error of the phase $\Delta\phi$ can be calculated from error of the time $\Delta t = 0.1\,\text{ps}$ on the waveform via

$$\Delta\phi = 2\pi\nu \cdot \Delta t. \tag{C.2.7}$$

Figure C.5 (top) shows the refractive index and the absorption coefficient (blue) with the corresponding error range (grey) of a PPLN with a length of 5.05 mm at room temperature. The relative error of the refractive index is in the order of 0.23%, for example at 0.5 THz

$$n = 5.088 \pm 0.01. \tag{C.2.8}$$

The error on the refractive index is constant over the analyzed frequency range as seen in figure C.5 (bottom, left). The absorption coefficient is at 0.5 THz

$$\alpha = 5.983 \pm 0.03, \tag{C.2.9}$$

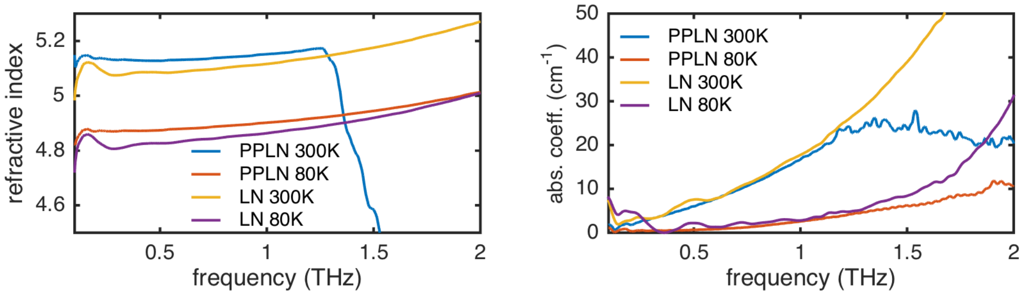

Figure C.6.: Extraordinary refractive index (left) and absorption coefficient (right) of 5.05 mm long 5 mol% periodically poled MgO:LN and a 0.52 mm long 5 mol% Mg:LN wafer at room and cryogenic temperature.

leading to a relative error of 0.4%. This error is pretty low due to the long length of the PPLN. For lower frequencies the relative error increases. Below 0.2 THz the relative error exceeds 2%. For frequencies lower then 0.1 THz the error increases to above 10% and therefore the measured values can not be regarded as reliable anymore.

C.2.2. Influence of the sample thickness

Measuring the refractive index and the absorption coefficient of a long PPLN reduces the error, but values above 1 THz are not measurable at room temperature as the THz pulse is already absorbed (see figure C.6 blue curve). At cryogenic temperature the limit can be increased due to lower absorption (see figure C.6 red curve). To reach higher frequencies, shorter samples are required (see figure C.6 yellow and purple curve). But the shorter sample of 0.52 mm increases the error on the optical parameters. The main contribution here is the precision of the thickness measurement which is about 10 µm. This relative error on a 5 mm thick sample is around 0.2%, on a 0.5 mm sample it is already 2%. Therefore the overall error is increased. As the samples are all optical polished with a precision of much less then 1 µm the error from the variation of the thickness in a sample can be neglected.

In figure C.7 the refractive index and the absorption coefficient with the corresponding error range are depicted for two samples of different length to indicate the influence of sample thickness on the measurement uncertainties. The two top graphics show the refractive index (left) and the absorption coefficient (right) of a PPLN with a length of

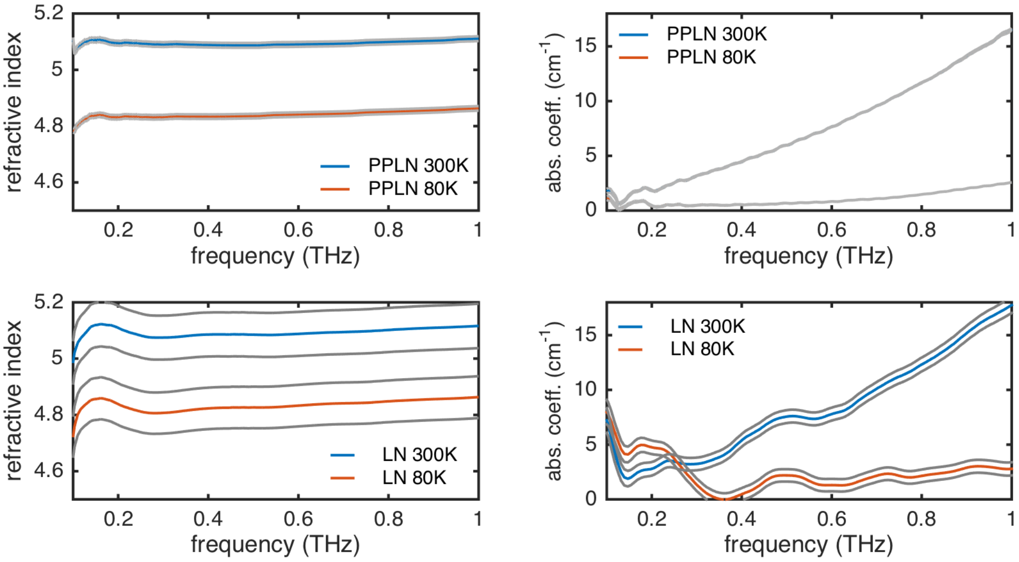

Figure C.7.: Error on the refractive index (left) and absorption coefficient (right) for two different samples: PPLN with 5.05 mm (top) and LN wafer with 0.52 mm (bottom) thickness.

5.05 mm at room temperature (300K) and cryogenic temperature (80K). The error is here smaller then 1%. The two bottom graphs show the same measurements for a LN wafer with a thickness of just 0.52 mm. Here the relative error of the refractive index increases to 1.5% and the relative error of the absorption coefficient increases to 7.6%.

Besides the increased overall error on the thin LN sample, the error in the low frequency range is further increased, as the frequency resolution for a thin sample of $dl = 0.5\,\text{mm}$ is reduced:

$$d\nu = \frac{2\pi}{dt} = \frac{\pi\ c}{dl\ n} = 0.37\,\text{THz}. \tag{C.2.10}$$

For a longer sample of $dl = 5\,\text{mm}$ the frequency resolution is increased to

$$d\nu = \frac{2\pi}{dt} = \frac{\pi\ c}{dl\ n} = 0.04\,\text{THz}. \tag{C.2.11}$$

A sufficient thickness of the sample is therefore mandatory to extract valid data in the low frequency range.

C.3. Conclusion

A 5 mm thick PPLN sample in the THz-TDS allows a precise measurement in the range of 0.3 to 1 THz at room and cryogenic temperatures with an error of less then 1%. Below 0.3 THz the errors are rapidly increasing reaching 2% at 0.2 THz and 10% at 0.1 THz. To maintain adequate precision from 0.1 to 0.3 THz the clear aperture of the sample has to be increased to 6.4 - 12 mm. The clear aperture reduce the losses due to gaussian beam propagation. For lower frequencies than 0.1 THz the THz-TDS is not suited due to instrumental errors. In the frequency range of 0.3 to 3 THz this instrument is a great tool to analyze optical properties in the THz range delivering valid data.

Bibliography

[Abr66a] S. Abrahams, W. Hamilton and J. Reddy, *Ferroelectric lithium niobate. 4. Single crystal neutron diffraction study at 24°C*, Journal of Physics and Chemistry of Solids **27**, 1013 - 1018 (1966).

[Abr66b] S. Abrahams, H. Levinstein and J. Reddy, *Ferroelectric lithium niobate. 5. Polycrystal X-ray diffraction study between 24° and 1200° C*, Journal of Physics and Chemistry of Solids **27**, 1019–1026 (1966).

[Abr66c] S. Abrahams, J. M. Reddy and J. Bernstein, *Ferroelectric lithium niobate. 3. Single crystal X-ray diffraction study at 24 C*, Journal of Physics and Chemistry of Solids **27**, 997–1012 (1966).

[Agg77] R. Aggarwal and B. Lax, *Optical mixing of CO 2 lasers in the far-infrared*, Nonlinear infrared generation, 19–80 (1977).

[Ahr16] F. Ahr, K. Ravi, S. Carbajo, S. Jolly, T. Kroh, D. N. Schimpf, N. H. Matlis, A. R. Maier and F. X. Kaertner, *Pulse-train pumping for efficient narrowband terahertz generation in periodically poled lithium niobate*, Conference on Lasers and Electro-Optics, Optical Society of America, 2016, p. JTh2A.58.

[Ahr17] F. Ahr, S. W. Jolly, N. H. Matlis, S. Carbajo, T. Kroh, K. Ravi, D. N. Schimpf, J. Schulte, H. Ishizuki, T. Taira, A. R. Maier and F. X. Kärtner, *Narrowband terahertz generation with chirped-and-delayed laser pulses in periodically poled lithium niobate*, Optics Letters **42**, 2118–2121 (2017).

[Ant14] V. Antsygin, A. Kaplun, A. Mamrashev, N. Nikolaev and O. Potaturkin, *Terahertz optical properties of potassium titanyl phosphate crystals*, Optics express **22**, 25436–25443 (2014).

[Ash66] A. Ashkin, G. D. Boyd, J. M. Dziedzic, R. G. Smith, A. A. Ballman, J. J. Levinstein and K. Nassau, *Optically-induced refractive index inhomogenities in LiNbO3 AND LiTaO3*, Applied Physics Letters **9**, 72-74 (1966).

[Aus83] D. Auston and P. Smith, *Generation and detection of millimeter waves by picosecond photoconductivity*, Applied Physics Letters **43**, 631–633 (1983).

[Bac17] F. Bach, M. Mero, M.-H. Chou and V. Petrov, *Laser induced damage studies of LiNbO3 using 1030-nm, ultrashort pulses at 10-1000 kHz*, Opt. Mater. Express **7**, 240–252 (2017).

[Bau16] C. Baumgarten, M. Pedicone, H. Bravo, H. Wang, L. Yin, C. S. Menoni, J. J. Rocca and B. A. Reagan, *1 J, 0.5 kHz repetition rate picosecond laser*, Optics Letters **41**, 3339–3342 (2016).

[Bec13] M. Beck, I. Rousseau, M. Klammer, P. Leiderer, M. Mittendorff, S. Winnerl, M. Helm, G. N. Gol'tsman and J. Demsar, *Transient Increase of the Energy Gap of Superconducting NbN Thin Films Excited by Resonant Narrow-Band Terahertz Pulses*, Physical Review Letter **110**, 267003 (2013).

[Boy61] G. D. Boyd and J. P. Gordon, *Confocal multimode resonator for millimeter through optical wavelength masers*, The Bell System Technical Journal **40**, 489-508 (1961).

[Boy64] G. Boyd, R. C. Miller, K. Nassau, W. Bond and A. Savage, *LiNbO3: an efficient phase matchable nonlinear optical material*, Applied physics letters **5**, 234–236 (1964).

[Boy71] G. Boyd, T. Bridges, M. Pollack and E. Turner, *Microwave nonlinear susceptibilities due to electronic and ionic anharmonicities in acentric crystals*, Physical Review Letters **26**, 387 (1971).

[Boy03] R. W. Boyd, *Nonlinear optics*, Handbook of Laser Technology and Applications (Three-Volume Set), Taylor & Francis, 2003, pp. 161–183.

[Bus02] A. C. Busacca, C. L. Sones, V. Apostolopoulos, R. W. Eason and S. Mailis, *Surface domain engineering in congruent lithium niobate single crystals: A route to submicron periodic poling*, Applied physics letters **81**, 4946–4948 (2002).

[Cao09] Z. Cao, X. Gao, W. Chen, H. Wang, W. Zhang and Z. Gong, *Study of quasi-phase matching wavelength acceptance bandwidth for periodically poled LiNbO3 crystal-based difference-frequency generation*, Optics and Lasers in Engineering **47**, 589-593 (2009).

[Car15] S. Carbajo, J. Schulte, X. Wu, K. Ravi, D. Schimpf and F. Kärtner, *Efficient narrowband terahertz generation in cryogenically cooled periodically poled lithium niobate*, Optics Letters **40**, 5762-5765 (2015).

[CG04] M. Cronin-Golomb, *Cascaded nonlinear difference-frequency generation of enhanced terahertz wave production*, Optics Letter **29**, 2046–2048 (2004).

[Che11] Z. Chen, X. Zhou, C. A. Werley and K. A. Nelson, *Generation of high power tunable multicycle teraherz pulses*, Applied Physics Letters **99**, 071102 (2011).

[Cir17] G. Cirmi, M. Hemmer, K. Ravi, F. Reichert, L. E. Zapata, A.-L. Calendron, H. Çankaya, F. Ahr, O. D. Mücke, N. H. Matlis and F. X. Kärtner, *Cascaded second-order processes for the efficient generation of narrowband terahertz radiation*, Journal of Physics B: Atomic, Molecular and Optical Physics **50**, 044002 (2017).

[Cun92] S. Cunsolo, P. Dore and C. Varsamis, *Refractive index of crystals from transmission and reflection measurements: MgO in the far-infrared region*, Applied optics **31**, 4554–4558 (1992).

[Dhi17] S. Dhillon, M. Vitiello, E. Linfield, A. Davies, M. C. Hoffmann, J. Booske, C. Paoloni, M. Gensch, P. Weightman, G. Williams et al., *The 2017 terahertz science and technology roadmap*, Journal of Physics D: Applied Physics **50**, 043001 (2017).

[Fak17] M. Fakhari, A. Fallahi and F. X. Kärtner, *THz cavities and injectors for compact electron acceleration using laser-driven THz sources*, Phys. Rev. Accel. Beams **20**, 041302 (2017).

[Fat89] C. Fattinger and D. Grischkowsky, *Terahertz beams*, Applied Physics Letters **54**, 490–492 (1989).

[Fej92] M. Fejer, G. Magel, D. Jundt and R. Byer, *Quasi-Phase-Matched Second Harmonic Generation: Tuning and Tolerances*, IEEE Journal of Quantum Electronics **28**, 2631-2654 (1992).

[Feu07] T. Feurer, N. S. Stoyanov, D. W. Ward, J. C. Vaughan, E. R. Statz and K. A. Nelson, *Terahertz polaritonics*, Annu. Rev. Mater. Res. **37**, 317–350 (2007).

[Fur91] Y. Furukawa, A. Yokotani, T. Sasaki, H. Yoshida, K. Yoshida, F. Nitanda and M. Sato, *Investigation of bulk laser damage threshold of lithium niobate single crystals by Q-switched pulse laser*, Journal of Applied Physics **69**, 3372-3374 (1991).

[Gay08] O. Gayer, Z. Sacks, E. Galun and A. Arie, *Temperature and wavelength dependent refractive index equations for MgO-doped congruent and stoichiometric LiNbO3*, Applied Physics B **91**, 343–348 (2008).

[Gla74] A. M. Glass, D. von der Linde and T. J. Negran, *High-voltage bulk photovoltaic effect and the photorefractive process in LiNbO3*, Applied Physics Letters **25**, 233-235 (1974).

[Gri83] P. Griffiths, *Fourier transform infrared spectrometry*, Science **222**, 297–302 (1983).

[Han00] G. Hansson, H. Karlsson, S. Wang and F. Laurell, *Transmission measurements in KTP and isomorphic compounds*, Applied optics **39**, 5058–5069 (2000).

[Heb08] J. Hebling, K. L. Yeh, M. C. Hoffmann and K. A. Nelson, *High-Power THz Generation, THz Nonlinear Optics, and THz Nonlinear Spectroscopy*, IEEE Journal of Selected Topics in Quantum Electronics **14**, 345-353 (2008).

[Hem11] M. Hemmer, *Few-cycle Pulses Amplification For Attosecond Science Applications Modeling And Experiments.*

[Ish12] H. Ishizuki and T. Taira, *Half-joule output optical-parametric oscillation using 10-mm-thick periodically poled Mg-doped congruent LiNbO*$_3$, Optics Express **20**, 20002-20010 (2012).

[Jaz02] M. Jazbinšek and M. Zgonik, *Material tensor parameters of LiNbO3 relevant for electro-and elasto-optics*, Applied Physics B: Lasers and Optics **74**, 407–414 (2002).

[Jen10] L. Jentjens, *Bestrahlungsinduzierte Modifikation der Materialparameter in magnesiumdotiertem Lithiumniobat*, Dissertation, Bonn, Univ., Diss., 2010, 2010.

[Jep96] P. U. Jepsen, R. H. Jacobsen and S. Keiding, *Generation and detection of terahertz pulses from biased semiconductor antennas*, JOSA B **13**, 2424–2436 (1996).

[Jep05] P. U. Jepsen and B. M. Fischer, *Dynamic range in terahertz time-domain transmission and reflection spectroscopy*, Optics letters **30**, 29–31 (2005).

[Jep11] P. U. Jepsen, D. G. Cooke and M. Koch, *Terahertz spectroscopy and imaging–Modern techniques and applications*, Laser & Photonics Reviews **5**, 124–166 (2011).

[Jol17] S. W. Jolly, F. Ahr, N. H. Matlis, F. X. Kärtner and A. R. Maier, in preparation (2017).

[Jun97] D. Jundt, *Temperature-dependent Sellmeier equation for the index of refraction, ne, in congruent lithium niobate*, Optics Letters **22**, 1553-1555 (1997).

[Kam13] T. Kampfrath, K. Tanaka and K. A. Nelson, *Resonant and nonresonant control over matter and light by intense terahertz transients*, Nature Photonics **7**, 680-690 (2013).

[Kär16] F. Kärtner, F. Ahr, A.-L. Calendron, H. Çankaya, S. Carbajo, G. Chang, G. Cirmi, K. Dörner, U. Dorda, A. Fallahi, A. Hartin, M. Hemmer, R. Hobbs, Y. Hua, W. Huang, R. Letrun, N. Matlis, V. Mazalova, O. Mücke, E. Nanni, W. Putnam, K. Ravi, F. Reichert, I. Sarrou, X. Wu, A. Yahaghi, H. Ye, L. Zapata, D. Zhang, C. Zhou, R. Miller, K. Berggren, H. Graafsma, A. Meents,

R. Assmann, H. Chapman and P. Fromme, *AXSIS: Exploring the frontiers in attosecond X-ray science, imaging and spectroscopy*, Nuclear Instruments and methods in Physics Research A **829**, 24-29 (2016).

[Kie13] J. Kiessling, K. Buse and I. Breunig, *Temperature-dependent Sellmeier equation for the extraordinary refractive index of 5 mol. % MgO-doped LiNbO3 in the terahertz range*, J. Opt. Soc. Am. B **30**, 950–952 (2013).

[Koj02] S. Kojima, N. Tsumura, H. Kitahara, M. W. Takeda and S. Nishizawa, *Terahertz time domain spectroscopy of phonon-polaritons in ferroelectric lithium niobate crystals*, Japanese journal of applied physics **41**, 7033 (2002).

[Lee00] Y.-S. Lee, T. Meade, V. Perlin, H. Winful, T. B. Norris and A. Galvanauskas, *Generation of narrow-band terahertz radiation via optical rectification of femtosecond pulses in periodically poled lithium niobate*, Applied Physics Letters **76**, 2505-2507 (2000).

[Lee01] Y.-S. Lee, T. Meade, T. B. Norris and A. Galvanauskas, *Tunable narrow-band terahertz generation from periodically poled lithium niobate*, Applied Physics Letters **78**, 3583-3585 (2001).

[Lee09] Y.-S. Lee, *Principles of terahertz science and technology*, vol. 170, Springer Science & Business Media, 2009.

[Len66] P. Lenzo, E. Spencer and K. Nassau, *Electro-optic coefficients in single-domain ferroelectric lithium niobate*, JOSA **56**, 633–635 (1966).

[L'h07a] J. L'huillier, G. Torosyan, M. Theuer, Y. Avetisyan and R. Beigang, *Generation of THz radiation using bulk, periodically and aperiodically poled lithium niobate – Part 1: Theory*, Applied Physics B **86**, 185–196 (2007).

[L'h07b] J. L'huillier, G. Torosyan, M. Theuer, C. Rau, Y. Avetisyan and R. Beigang, *Generation of THz radiation using bulk, periodically and aperiodically poled lithium niobate – Part 2: Experiments*, Applied Physics B **86**, 197–208 (2007).

[Lue03] M. Luennemann, U. Hartwig, G. Panotopoulos and K. Buse, *Electrooptic properties of lithium niobate crystals for extremely high external electric fields*, Applied Physics B: Lasers and Optics **76**, 403–406 (2003).

[Mai17] A. R. Maier, S. W. Jolly, V. Leroux and M. Schnepp, *Integration of the ANGUS 200 TW Laser-System into the Accelerator Infrastructure at DESY*, Conference on Lasers and Electro-Optics, Optical Society of America, 2017, p. JTu3L.4.

[Man56] J. M. Manley and H. E. Rowe, *Some General Properties of Nonlinear Elements-Part I. General Energy Relations*, Proceedings of the IRE **44**, 904-913 (1956).

[Mas71] W. Massey, W. Hook, D. Dobberpuhl and H. Jeffers, *Lithium niobate damage threshold measurements inside a Nd:YA Q-switched laser cavity*, IEEE Journal of Quantum Electronics **7**, 317-318 (1971).

[Mat49] B. Matthias and J. Remeika, *Ferroelectricity in the ilmenite structure*, Physical Review **76**, 1886 (1949).

[Mat91] S. Matsumoto, E. Lim, H. Hertz and M. Fejer, *Quasiphase-matched second harmonic generation of blue light in electrically periodically-poled lithium tantalate waveguides*, Electronics letters **27**, 2040–2042 (1991).

[Mat97] S. Matsuura, M. Tani and K. Sakai, *Generation of coherent terahertz radiation by photomixing in dipole photoconductive antennas*, Applied Physics Letters **70**, 559–561 (1997).

[Men16] Q. Meng, B. Zhang, S. Zhong and L. Zhu, *Damage threshold of lithium niobate crystal under single and multiple femtosecond laser pulses: theoretical and experimental study*, Applied Physics A **122**, 582 (2016).

[Mil97] G. Miller, R. Batchko, W. Tulloch, D. Weise, M. Fejer and R. Byer, *42%-efficient single-pass cw second-harmonic generation in periodically poled lithium niobate*, Optics letters **22**, 1834–1836 (1997).

[Mil98] G. D. Miller, *Periodically poled lithium niobate: modeling, fabrication, and nonlinear-optical performance*, Dissertation, Stanford University, 1998.

[Min05] L. Ming, C. B. Gawith, K. Gallo, M. V. O'Connor, G. D. Emmerson and P. G. Smith, *High conversion efficiency single-pass second harmonic generation in a zinc-diffused periodically poled lithium niobate waveguide*, Optics express **13**, 4862–4868 (2005).

[Mit96] D. M. Mittleman, R. H. Jacobsen and M. C. Nuss, *T-ray imaging*, IEEE Journal of selected topics in quantum electronics **2**, 679–692 (1996).

[MSG16] G. Menlo System GmbH, Munich, *User Manual of TeraK15/SYNC Terahertz Time Domain Spectrometer V1.0*, 2016.

[Mül04] M. Müller, *Wechselwirkung von Licht mit ferroelektrischen Domänen in Lithiumniobat-und Lithiumtantalat-Kristallen*, Dissertation, Dissertation, Universität Bonn, 2004.

[Naf13] M. Naftaly, *Metrology issues and solutions in THz time-domain spectroscopy: Noise, errors, calibration*, IEEE Sensors Journal **13**, 8–17 (2013).

[Nah96] A. Nahata, A. S. Weling and T. F. Heinz, *A wideband coherent terahertz spectroscopy system using optical rectification and electro-optic sampling*, Applied physics letters **69**, 2321–2323 (1996).

[Nan15] E. A. Nanni, W. R. Huang, K.-H. Hong, K. Ravi, A. Fallahi, G. Moriena, R. D. Miller and F. X. Kärtner, *Terahertz-driven linear electron acceleration*, Nature communications **6**, 8486 (2015).

[Nas66a] K. Nassau, H. Levinstein and G. Loiacono, *Ferroelectric lithium niobate. 1. Growth, domain structure, dislocations and etching*, Journal of Physics and Chemistry of Solids **27**, 983–988 (1966).

[Nas66b] K. Nassau, H. Levinstein and G. Loiacono, *Ferroelectric lithium niobate. 2. Preparation of single domain crystals*, Journal of Physics and Chemistry of Solids **27**, 989–996 (1966).

[O'B85] H. M. O'Bryan, P. K. Gallagher and C. Brandle, *Congruent Composition and Li-Rich Phase Boundary of LiNbO3*, Journal of the American Ceramic Society **68**, 493–496 (1985).

[Pál05] L. Pálfalvi, J. Hebling, J. Kuhl, Á. Péter and K. Polgár, *Temperature dependence of the absorption and refraction of Mg-doped congruent and stoichiometric LiNbO3 in the THz range*, Journal of Applied Physics **97**, 123505 (2005).

[Pas98] V. Pasiskevicius, S. Wang, J. A. Tellefsen, F. Laurell and H. Karlsson, *Efficient Nd: YAG laser frequency doubling with periodically poled KTP*, Applied optics **37**, 7116–7119 (1998).

[Ram00] J. Rams, A. A. de Velasco, M. Carrascosa, J. Cabrera and F. Agulló-López, *Optical damage inhibition and thresholding effects in lithium niobate above room temperature*, Optics Communications **178**, 211 - 216 (2000).

[Rav16a] K. Ravi, M. Hemmer, G. Cirmi, F. Reichert, D. N. Schimpf, O. D. Mücke and F. X. Kärtner, *Cascaded parametric amplification for highly efficient terahertz generation*, Optics Letters **41**, 3806–3809 (2016).

[Rav16b] K. Ravi, D. N. Schimpf and F. X. Kärtner, *Pulse sequences for efficient multi-cycle terahertz generation in periodically poled lithium niobate*, Optics Express **24**, 25582–25607 (2016).

[Rea12] B. A. Reagan, A. H. Curtis, K. A. Wernsing, F. J. Furch, B. M. Luther and J. J. Rocca, *Development of High Energy Diode-Pumped Thick-Disk Yb:YAG Chirped-Pulse-Amplification Lasers*, IEEE Journal of Quantum Electronics **48**, 827-835 (2012).

[Rön98] W. C. Röntgen, *Über eine neue Art von Strahlen*, Annalen der Physik **300**, 1–11 (1898).

[Sav66] A. Savage, *Pyroelectricity and spontaneous polarization in LiNbO3*, Journal of Applied Physics **37**, 3071–3072 (1966).

[Sch93] U. Schlarb and K. Betzler, *Refractive indices of lithium niobate as a function of temperature, wavelength, and composition: A generalized fit*, Physical Review B **48**, 15613 (1993).

[Sch09] P. G. Schunemann, K. T. Zawilski, T. M. Pollak, V. Petrov and D. E. Zelmon, *CdSiP 2: a new nonlinear optical crystal for 1-and 1.5-micron-pumped mid-IR* *generation*, Advanced Solid-State Photonics, Optical Society of America, 2009, p. TuC6.

[Sch11] J. R. Schwesyg, M. Falk, C. R. Phillips, D. H. Jundt, K. Buse and M. M. Fejer, *Pyroelectrically induced photorefractive damage in magnesium-doped lithium niobate crystals*, J. Opt. Soc. Am. B **28**, 1973–1987 (2011).

[SCH15] SCHOTT, *SCHOTT optical glass data sheets 2015-07-22*, 2015.

[Ser79] J. Servoin and F. Gervais, *Soft vibrational mode in LiNbO3 and LiTaO3*, Solid State Communications **31**, 387 - 391 (1979).

[Sho97] I. Shoji, T. Kondo, A. Kitamoto, M. Shirane and R. Ito, *Absolute scale of second-order nonlinear-optical coefficients*, JOSA B **14**, 2268–2294 (1997).

[Sie86] A. E. Siegman, *Lasers university science books*, Mill Valley, CA **37**, 630 (1986).

[Smi71] R. Smith and F. Welsh, *Temperature dependence of the elastic, piezoelectric, and dielectric constants of lithium tantalate and lithium niobate*, Journal of applied physics **42**, 2219–2230 (1971).

[Sow10] R. Sowade, I. Breunig, C. Tulea and K. Buse, *Nonlinear coefficient and temperature dependence of the refractive index of lithium niobate crystals in the terahertz regime*, Applied Physics B **99**, 63–66 (2010).

[Ste03] A. G. Stepanov, J. Hebling and J. Kuhl, *Efficient generation of subpicosecond terahertz radiation by phase-matched optical rectification using ultrashort laser pulses with tilted pulse fronts*, Applied Physics Letters **83**, 3000-3002 (2003).

[Sut03] R. L. Sutherland, *Handbook of nonlinear optics*, CRC press, 2003.

[Tho90] P. Thomas, A. Glazer and B. Watts, *Crystal structure and nonlinear optical properties of KSnOPO4 and their comparison with KTiOPO4*, Acta Crystallographica Section B: Structural Science **46**, 333–343 (1990).

[Unf15] M. Unferdorben, Z. Szaller, I. Hajdara, J. Hebling and L. Pálfalvi, *Measurement of refractive index and absorption coefficient of congruent and stoichiometric lithium niobate in the terahertz range*, Journal of Infrared, Millimeter, and Terahertz Waves **36**, 1203–1209 (2015).

[Vod06] K. L. Vodopyanov, M. M. Fejer, X. Yu, J. S. Harris, Y.-S. Lee, W. C. Hurlbut, V. G. Kozlov, D. Bliss and C. Lynch, *Terahertz-wave generation in quasi-phase-matched GaAs*, Applied Physics Letters **89** (2006).

[Vod08] K. L. Vodopyanov, *Optical THz-wave generation with periodically-inverted GaAs*, Laser & Photonics Reviews **2**, 11–25 (2008).

[WC08] Wikimedia-Commons, *Crystal structure of LiNbO3 showing octahedral oxygen coordination spheres of niobium*, 2008, File: LiNbO3.png, https://upload.wikimedia.org/wikipedia/commons/0/0c/LiNbO3.png; Attribution: By Solid State (Own work) [Public domain], via Wikimedia Commons.

[Wei85] R. Weis and T. Gaylord, *Lithium niobate: summary of physical properties and crystal structure*, Applied Physics A: Materials Science & Processing **37**, 191–203 (1985).

[Wei01] C. Weiss, G. Torosyan, Y. Avetisyan and R. Beigang, *Generation of tunable narrow-band surface-emitted terahertz radiation in periodically poled lithium niobate*, Optics Letter **26**, 563–565 (2001).

[Wei11] A. Weiner, *Ultrafast optics*, vol. 72, John Wiley & Sons, 2011.

[Wel94] A. S. Weling, B. B. Hu, N. M. Froberg and D. H. Auston, *Generation of tunable narrowband THz radiation from large aperture photoconducting antennas*, Applied Physics Letters **64**, 137-139 (1994).

[Wen05] M. Wengler, U. Heinemeyer, E. Soergel and K. Buse, *Ultraviolet light-assisted domain inversion in magnesium-doped lithium niobate crystals*, Journal of applied physics **98**, 064104 (2005).

[Wit08] W. Withayachumnankul, B. M. Fischer, H. Lin and D. Abbott, *Uncertainty in terahertz time-domain spectroscopy measurement*, JOSA B **25**, 1059–1072 (2008).

[Won13] L. J. Wong, A. Fallahi and F. X. Kärtner, *Compact electron acceleration and bunch compression in THz waveguides*, Opt. Express **21**, 9792–9806 (2013).

[Wu15] X. Wu, C. Zhou, W. Huang, F. Ahr and F. Kärtner, *Temperature dependent refractive index and absorption coefficient of congruent lithium niobate crystals in the terahertz range*, Optics Express **23**, 29729-29737 (2015).

[Wu16] M.-H. Wu, Y.-C. Chiu, T.-D. Wang, G. Zhao, A. Zukauskas, F. Laurell and Y.-C. Huang, *Terahertz parametric generation and amplification from potassium titanyl phosphate in comparison with lithium niobate and lithium tantalate*, Optics Express **24**, 25964–25973 (2016).

[Xu92] L. Xu, X.-C. Zhang and D. Auston, *Terahertz beam generation by femtosecond optical pulses in electro-optic materials*, Applied Physics Letters **61**, 1784–1786 (1992).

[Yaj70] T. Yajima and N. Takeuchi, *Far-infrared difference-frequency generation by picosecond laser pulses*, Japanese Journal of Applied Physics **9**, 1361 (1970).

[Yam93] M. Yamada, N. Nada, M. Saitoh and K. Watanabe, *First-order quasi-phase matched LiNbO3 waveguide periodically poled by applying an external field for efficient blue second-harmonic generation*, Applied Physics Letters **62**, 435-436 (1993).

[Yu11] N. E. Yu, K. S. Lee, D.-K. Ko, C. Kang, S. Takekawa and K. Kitamura, *Temperature dependent narrow-band terahertz pulse generation in periodically poled crystals via difference frequency generation*, Optics Communications **284**, 1395 (2011).

[Zac29] W. Zachariasen, *Untersuchungen über die Kristallstrukturen von Sesquioxiden und Verbindungen ABO3*, GFF **51**, 123–123 (1929).

[Zap15] L. E. Zapata, H. Lin, A.-L. Calendron, H. Cankaya, M. Hemmer, F. Reichert, W. R. Huang, E. Granados, K.-H. Hong and F. X. Kärtner, *Cryogenic Yb: YAG composite-thin-disk for high energy and average power amplifiers*, Optics letters **40**, 2610–2613 (2015).

[Zel97] D. E. Zelmon, D. L. Small and D. Jundt, *Infrared corrected Sellmeier coefficients for congruently grown lithium niobate and 5 mol.oxide-doped lithium niobate*, Journal of the Optical Society of America B **14**, 3319-3322 (1997).

Acronyms

AR	anti-reflection
BS	beam splitter
CPA	chirp pulse amplfication
DAQ	data aquisition
DFG	difference frequency generation
EOS	electro optic sampling
FIR	far-infrared
FEL	free-electron lasers
FFT	fast Fourier transform
FS	fused silica
FTIR	Fourier transform infrared spectrometer
FWHM	full-width half maximum
GD	group delay
GDD	group delay dispersion
HR	high reflector
IR	infrared
$\mathbf{LiNbO_3}$	lithium niobate

LN_2	liquid nitrogen
MgO:PPLN	magnesium oxide doped periodically poled lithium niobate
MIR	mid-infrared
NIR	near-infrared
OAP	off-axis parabola
OR	optical rectification
PEEK	Polyetheretherketon
PPLN	periodically poled lithium niobate
QPM	quasi phase-matching
RSD	relative standard deviation
THz-TDS	terahertz time domain spectrometer
THz	terahertz
TOD	third order dispersion
TPX	Polymethylpentene
UV	ultra violet
VIS	visible

List of Figures

List of Tables

Eidesstattliche Versicherung

Hiermit erkläre ich an Eides statt, dass ich die vorliegende Dissertationsschrift selbst verfasst und keine anderen als die angegebenen Quellen und Hilfsmittel benutzt habe.

Frederike Beate Ahr, M.Sc.

Acknowledgments

Finalizing my thesis at the Center for Free Electron Science at the "Deutsches Elektronen Synchrotron" in the Ultrafast Optics and X-ray division it is time to review and to thank all people supporting me during this period of my life.

First of all my sincere thank goes to my advisor, Professor Franz X. Kärtner, for the great opportunity to work in such an inspiring and encouraging environment. He gave me the chance to join the exciting project AXSIS and to enter this fascinating research area. I am grateful to his continuous guidance, the numerous motivating discussions and his valuable scientific advise.

I thank my second advisor, Andreas Maier, for many fruitful scientific discussions and the opportunity to perform research in his lab increasing my knowledge on plasma wake-field acceleration and teaching me on accelerator beam lines. I especially thank Spencer Jolly for the enjoyable teamwork. I highly appreciate his time when we explored hidden mysteries during valuable discussions.

I am grateful to Nicholas Matlis for his supervision over the last two year. His scientific advise and motivating discussions paved my way as scientist. Regarding the full AXSIS team: it was so great working with you in such an creative and fertile setting expanding my horizon. In particular many thanks to Jan Schulte and Sergio Carbajo for the initial experiments with the PPLNs, Arya Fallahi, Koustuban Ravi and Jan Schulte for the theoretical support and Xiaojun Wu, Tobias Kroh and Halil Olgun for their contributions on the THz-TDS experiments. Deeply thanks go to Daniele Nicoletti and Andrea Cavalleri for the possibility to use the FTIR and especially Daniele for the teaching the secrets of FTIR and how to handle cold gases.

An especial and deep thank goes to all engineers of the CFEL UX group, Matthias Schust, Thomas Tilp, Andrej Berg and Johann Derksen: they always were able to work miracles, when I came up with complicated wishes. Furthermore, I like to thank the LUX team and the CFEL UX group for the inspiring discussions and all the help.

I like to thank Anne-Laure Calendron, Joachim Meier, Spencer Jolly, Axel Rühl and Nicholas Matlis for continuous feedback and proof-reading my thesis.

My thanks go to the graduate schools International Max Planck Research School for Ultrafast Imaging & Structural Dynamics and PIER Helmholtz Graduate School for all the interesting courses and the possibility to have an insight in the further research fields on campus. The time as student representative of IMPRS helped me to detect my strength and weakness and empowered my leadership skills. I especially thank our secretary Christine Berber for running the administrative jungle and the helping hand whenever the paper work was far too much.

Financial support is essential for living and for successful research. I acknowledge the research funding provided by "Deutsches Elektronen-Synchrotron" and by the "European Research Council (ERC) under the European Union Seventh Framework Programme (FP7) (FP7/2007-2013)/ERC Grant (609920)".

I am extremely grateful to all my friends at CFEL and campus, to name a few: Nele Müller, Stephanie Maier, Theresa Brümmer and Julia Maracke. I thank all my friends inside and outside DESY for their support and friendship.

I express my deepest gratitude to my parents. I am so glad to have you with all your inspiration and your unconditional support.

List of Publications

Publications based on this thesis

1. *Generation of narrowband terahertz pulses via pulse-train pumping of periodically poled lithium niobate*
   F. Ahr, N. H. Matlis, S. W. Jolly, K. Ravi, D. N. Schimpf, A. Fallahi and F. X. Kärtner
   In preparation

2. *High energy, multi-cycle terahertz pulses generated via chirped-and-delayed laser pulses in periodically poled lithium niobate*
   S. W. Jolly, **F. Ahr**, N. H. Matlis, H. Ishizuki, T. Taira, A. R. Maier, and F. X. Kärtner
   In preparation

3. *Narrowband terahertz generation with chirped-and-delayed laser pulses in periodically poled lithium niobate*
   F. Ahr, S. W. Jolly, N. H. Matlis, S. Carbajo, T. Kroh, K. Ravi, D. N. Schimpf, J. Schulte, H. Ishizuki, T. Taira, A. R. Maier, and F. X. Kärtner
   Optics Letters **42**(11), 2118-2121 (2017)

4. *Temperature dependent refractive index and absorption coefficient of congruent lithium niobate crystals in the terahertz range*
   X. Wu, C. Zhou, W. R. Huang, **F. Ahr**, F. X. Kärtner
   Optics express **23**(23), 29729 (2015)

Publications beyond this thesis

1. *Cascaded regime of optical parametric amplification for efficient THz radiation generation*
   M. Hemmer, G. Cirmi, K. Ravi, F. Reichert, **F. Ahr**, L. E. Zapata, O. D. Mücke, A.-L. Calendron, H. Cankaya, D. Schimpf, N. H. Matlis and F. X. Kärtner
   In preparation

2. *Terahertz-induced molecular orientation of liquid water and other molecular liquids*
   P. Zalden, L. Song, X. Wu, H. Huang, **F. Ahr**, O. D. Mücke, J. Reichert, M. Thorwart, P. Kr. Mishra, R. Welsch, R. Santra, F. X. Kärtner and C. Bressler
   Submitted (2017)

3. *Cascaded second-order processes for the efficient generation of narrowband terahertz radiation*
   G. Cirmi, M. Hemmer, K. Ravi, F. Reichert, L. E. Zapata, A.-L. Calendron, H. Cankaya, **F. Ahr**, O. D. Mücke, N. H. Matlis and F. X. Kärtner
   Journal of Physics B: Atomic, Molecular and Optical Physics (2016)

4. *AXSIS: Exploring the frontiers in attosecond X-ray science, imaging and spectroscopy*
   F. X. Kärtner, **F. Ahr**, A.-L. Calendron, H. Çankaya, S. Carbajo, G. Chang, G. Cirmi, K. Dörner, U. Dorda, A. Fallahi, A. Hartin, M. Hemmer, R. Hobbs, Y. Hua, W.R. Huang, R. Letrun, N. Matlis, V. Mazalova, O.D. Mücke, E. Nanni, W. Putnam, K. Ravi, F. Reichert, I. Sarrou, X. Wu, A. Yahaghi, H. Ye, L. Zapata, D. Zhang, C. Zhou, R.J.D. Miller, K.K. Berggren, H. Graafsma, A. Meents, R.W. Assmann, H.N. Chapman, P. Fromme
   Nuclear Instruments and Methods in Physics Research Section A: Accelerators, Spectrometers, Detectors and Associated Equipment (2016)

5. *Terahertz generation in lithium niobate driven by Ti: sapphire laser pulses and its limitations*
   X. Wu, S. Carbajo, K. Ravi, **F. Ahr**, G. Cirmi, Y. Zhou, O. D. Mücke, F. X. Kärtner
   Optics letters **39**(18), 5403 (2014)

Conference proceedings

1. *Terahertz Accelerator Technology*
   F. X. Kärtner, K. Ravi, S. W. Jolly, **F. Ahr**, D. Zhang, X. Wu, M. Fakhari, H. Cankaya, A.-L. Calendron, C. Zhou, F. Lemery, W. Qiao, R. W. Huang, S. Carbajo, D. N. Schimpf, A. R. Maier, M. Hemmer, L. Zapata, O. D. Mücke, G. Cirmi, A. Fallahi, N. H. Matlis1, H. Shizuki, T. Taira
   Nonlinear Optics Conference, Hawaii (2017)

2. *THz Linear Acceleration For Compact Electron And X-ray Sources*
   M. Fakhari, D. Zhang, A. Fallahi, X. Wu, H. Cankaya, A.-L. Calendron, **F. Ahr**, K. Ravi, N. H. Matlis, F. X. Kärtner
   IRMMW-THz, 42nd International Conference on Infrared, Millimeter and Terahertz Waves (2017)

3. *THz Linear Acceleration for Compact Electron and X-ray Sources*
   F. X. Kärtner, D. Zhang, A. Fallahi, X. Wu, M. Fakhari, H. Cankaya, A.-L. Calendron, C. Zhou, F. Ahr, F. Lemery, W. Qiao, R. W. Huang, K. Ravi, N. H. Matlis
   OTST Conference, London (2017)

4. *Narrowband THz generation via chirp-and-delay in PPLN*
   F. Ahr, S. W. Jolly, N. H. Matlis, S. Carbajo, K. Ravi, T. Kroh, J. Schulte, D. N. Schimpf, A. R. Maier, and F. X. Kärtner
   CLEO/Europe-EQEC, Optical Society of America **CC-2.1** (2017)

5. *THz-driven electron streak camera based on a multilayer structure*
   D Zhang, A. Fallahi, X. Wu, M. Fakhari, H. Cankaya, A.-L. Calendron, C. Zhou, W. R. Huang, D. Haynes, F. Lemery, **F. Ahr**, W. Qiao, N. H. Matlis, F. X. Kärtner
   CLEO/Europe-EQEC, Optical Society of America **CC-1.4** (2017)

6. *Narrowband Terahertz Generation with Broadband Chirped Pulse Trains in Periodically Poled Lithium Niobate*
   S. W. Jolly, **F. Ahr**, N. H. Matlis, S. Carbajo, K. Ravi, T. Kroh, J. Schulte, D. N. Schimpf, A. R. Maier, and F. X. Kärtner
   CLEO: QELS_Fundamental Science, Optical Society of America **FW4D.4** (2017)

7. *Pulse-train pumping for efficient narrowband terahertz generation in periodically poled lithium niobate*
   F. Ahr, K. Ravi, S. Carbajo, S. W. Jolly, T. Kroh, D. N. Schimpf, N. H. Matlis, A. R. Maier, F. X. Kärtner
   CLEO: QELS_Fundamental Science, Optical Society of America **JTh2A–58** (2016)

8. *THz-wave generation via cascaded optical parametric amplification*
   M. Hemmer, G. Cirmi, F. Reichert, K. Ravi, **F. Ahr**, H. Cankaya, N. H. Matlis, O. D. Mücke, L. E. Zapata, F. X. Kärtner
   IRMMW-THz, 41th International Conference on Infrared, Millimeter, and Terahertz waves, IEEE (2016)

9. *Pulse sequences for high-energy terahertz generation*
   K. Ravi, **F. Ahr**, G. Cirmi, M. Hemmer, F. Reichert, D. N. Schimpf, H. Cankaya, O. D. Mücke, L. E. Zapata, N. H. Matlis, F. X. Kärtner
   IRMMW-THz, 41th International Conference on Infrared, Millimeter, and Terahertz waves, IEEE (2016)

10. *Cascaded optical parametric chirped-pulse amplification for multi-cycle THz-wave generation*
    M. Hemmer, F. Reichert, G. Cirmi, K. Ravi, **F. Ahr**, F. Lemery, A.-L. Calendron, H. Cankaya, D. N. Schimpf, L. E. Zapata, N. H. Matlis, F. X. Kärtner
    International Conference on Ultrafast Phenomena, Optical Society of America **UTu2A–6** (2016)

11. *Cascaded optical parametric amplification: A novel approach to efficient THz wave generation*
    G. Cirmi, M. Hemmer, F. Reichert, K. Ravi, **F. Ahr**, H. Cankaya, A.-L. Calendron, L. E. Zapata, N. H. Matlis, O. D. Mücke, F. X. Kärtner
    Photonics North (PN), IEEE (2016)

12. *Cascaded optical parametric amplifier in PPLN for efficient narrowband terahertz generation*
    G. Cirmi, F. Reichert, M. Hemmer, K. Ravi, **F. Ahr**, F. Lemery, A.-L. Calendron,

H. Cankaya, D. N. Schimpf, L. E. Zapata, N. H. Matlis, F. X. Kärtner
CLEO: Science and Innovations, Optical Society of America **SM2L–4** (2016)

13. *Efficient narrowband terahertz generation in periodically poled lithium niobate*
   F. Ahr, S. Carbajo, J. Schulte, X. Wu, K. Ravi, D. N. Schimpf, F. X. Kärtner
   Conference: DPG 2016, At Hannover, Germany **Q45.5** (2015)

14. *Optimized Generation of Strong-Field Terahertz Pulses at 0.8 and 1.03 μm Wavelengths*
   X. Wu, S. Carbajo, A.-L. Calendron, H. Cankaya, K. Ravi, **F. Ahr**, G. Cirmi, G. M. Rossi, O. D. Mücke, F. X. Kärtner
   German THz Conference 2015, Dresden **PUBDB-2016-00722** (2015)

15. *Efficient generation of terahertz radiation at 800 nm wavelength*
   X. Wu, S. Carbajo, K. Ravi, W. R. Huang , S. Fang, **F. Ahr**, G. Cirmi, G. M. Rossi, O. D. Mücke, F. X. Kärtner
   IRMMW-THz, 40th International Conference on Infrared, Millimeter, and Terahertz waves, IEEE (2015)

16. *On extracting the maximum terahertz conversion efficiency from optical rectification in lithium niobate*
   S. Carbajo, P. Alcorta, A.-L. Calendron, H. Cankaya, X. Wu, K. Ravi, **F. Ahr**, W. R. Huang, F. X. Kärtner
   CLEO: Science and Innovations, Optical Society of America **SM2H–3** (2015)

17. *Terahertz time domain spectrometer to characterize nonlinear materials for efficient terahertz generation*
   F. Ahr, S. Carbajo, G. Cirmi, O. D. Mücke, X. Wu, F. X. Kärtner
   Conference: DPG 2015, At Bochum, Germany **K4.6** (2015)

18. *Terahertz Generation and its Limitations in Lithium Niobate by Optical Rectification*
   X. Wu, S. Carbajo, K. Ravi, **F. Ahr**, F. X. Kärtner
   Advanced Solid State Lasers, Optical Society of America **ATh2A–33** (2014)

19. *Terahertz conversion efficiency scaling by optical rectification in the 800 nm pump-wavelength range*

S. Carbajo, X. Wu, K. Ravi, **F. Ahr**, F. X. Kärtner

CLEO: Science and Innovations, Optical Society of America **SW1F–6** (2014)